UNIVERSITY of CALIFORNIA, Santa Barbara

Crystal plasticity modeling to understand interactions between slip and deformation twinning in hexagonal close packed alloys

A dissertation submitted in partial satisfaction of the requirements for the degree

Doctor of Philosophy in Mechanical Engineering

Jiaxiang Wang

Committee in charge:

Professor Irene J. Beyerlein, Chair

Professor Samantha Daly

Professor G. Robert Odette

Dr. Raymond F. Decker

June 2022

The dissertation of Jiaxiang Wang is approved.

Professor Samantha Daly

Professor G. Robert Odette

Dr. Raymond F. Decker

Professor Irene J. Beyerlein, Committee Chair

June 2022

This thesis is dedicated to my parents and my Ph.D. advisor

Acknowledgments

First, I would like to express my sincere gratitude to my advisor, Prof. Irene J. Beyerlein, for the continuous support of my Ph.D. study and research. Her guidance helped me during the entire time of the research for this thesis. Over the past four years, her advice always gives me inspiration for overcoming the research challenges I have encountered.

I would also like to thank Prof. Marko Knezevic from the University of New Hampshire and Dr. Arul Kumar from Los Alamos National Lab for providing the basic version of the crystal plasticity codes and their advice in computer modeling.

I want to also thank Professor Samantha Daly, Professor G. Robert Odette, and Dr. Raymond F. Decker for being a member of the committee and giving me essential advice in my thesis work.

Finally, I would like to thank my friends and family for putting up with me and giving me emotional support when I was frustrated about my research progress. Without their motivation, I would not have been able to complete my degree.

Jiaxiang Wang

805-837-9443 | wangjiaxiang1511@outlook.com | linkedin.com/in/JiaxiangW

SUMMARY OF QUALIFICATIONS

- Energetic Ph.D. candidate in Mechanical Engineering. Expertise in Solid Mechanics and Metallic Structures
- Quick learner with strong technical skills who is proficient in Abaqus, MATLAB, Fortran, and python scripting.
- Experience solving technical problems in the following areas: 3D modeling, Finite element analysis, Numerical analysis, materials, machine learning, and continuum mechanics.
- Experienced researcher in simulation work and published four papers, three as lead-author, in science with high impact factor.

KEY SKILLS

Programing Fortran, Python, MATLAB

Software ABAQUS, AutoCAD, SolidWorks, Dream3D, Patran, Paraview, Microsoft office, ANSYS

Language Chinese (Native), English (Professional), Japanese (Limited)

EDUCATION

Ph.D., Mechanical Engineering | *Area of research:* Materials June 2022

M.S., Mechanical Engineering | *Area of research:* Materials June 2018

University of California, Santa Barbara (UCSB), Santa Barbara, CA

B. Eng., Mechanical Engineering | *GPA:* 3.8/4.0 June 2015

Eastern Washington University (EWU), Cheney, WA

RESEARCH EXPERIENCE

Research Assistant, UCSB, Santa Barbara, CA
Feb. 2018-Present

Project 1: Research layer size effect on nano-layered Mg/Nb composite by crystal plasticity finite element method.

- Developed crystal plasticity model independently in finite element framework
- Created 3D microstructure model and conducted the nonlinear simulation in Abaqus with Fortran based user subroutine
- Analyzed the result by MATLAB and identified the primary strengthening mechanism in nano-layered material.
- Published key findings that are impactful in nano-layered material field in *Journal of the Mechanics and Physics of Solids*.

Project 2: Investigate the deformation mechanism in Titanium (Ti) during cyclic loading

- Advanced the Elasto-Plastic Self-Consistent model by incorporating a slip-system level backstress
- Significantly increased the model prediction ability in cyclic loading and accurately captured the macroscopic responses in four loading paths.
- Had significant finding of dislocation-twin interaction which can help improve the performance of HCP metals
- Published results in the *International Journal of Plasticity* as the lead author.

Project 3: Study twin-twin interaction in HCP metal.

- Worked collaboratively with experimental scientists to study twin-twin interaction in HCP metal
- Designed and conducted the simulation by using the crystal-plasticity fast Fourier transform method.
- Wrote the python script for stress analysis and data visualization.
- Hosted weekly meetings (via zoom) to update project progress and overcome research challenges.
- Presented key findings in *Material and Science Technology 2021*.

ADDITIONAL LEADERSHIP EXPERIENCE

Teaching Assistant, UCSB**,** Santa Barbara, CA
Jan. 2017-Present

- Instructed students in vibration, heat transfer, static, dynamic, and material areas to 30 students per section.
- Answered technical questions related to course knowledge, exam, and homework problems to help students have a better understanding of class material.

PUBLICATION

- **Wang, J**., Knezevic, M., Jain, M., Pathak, S., Beyerlein, I.J*; Role of interface-affected dislocation motion on the strength of Mg/Nb nanolayered composites inferred by dual-mode confined layer slip crystal plasticity, J. Mech. Phys. Solids, 2021. (SCI, IF=5.471)
- **Wang, J**., Wang, X., Yu, K., Rupert, T., Mahajan, S., Lavernia, E., Schoenung, Beyerlein, I.J*; Manipulating deformation mechanisms with Y alloying of Mg. Mater. Sci. Eng. A, 2021. (SCI, If=5.234)
- **Wang, J**., Zecevic, M., Knezevic, M., Beyerlein, I.J*; Polycrystal plasticity modeling for load reversals in commercially pure titanium. Int J Plasticity, 2020, (SCI, IF=7.081)
- Leu, B., Savage, D.J., **Wang, J**., Alam, M.E., Mara, N.A., Kumar, M.A., Carpenter, J.S., Vogel, S.C., Knezevic, M., Decker, R., Beyerlein, I.J.*; Processing of Dilute Mg–Zn–Mn–Ca Alloy/Nb Multilayers by Accumulative Roll Bonding. Adv. Eng. Mater., 2020(SCI,IF=3.862)
- Zhang, J., **Wang, J.,**Zou,X., Beyerlein, I.J.,Han W.*; Texture evolution and temperature-dependent deformation modes in ambient- and cryogenic-rolled nanolayered Zr-2.5Nb. Acta Mater., 2022(SCI, IF=8.203)

Abstract:

Crystal plasticity modeling to understand interactions between slip and deformation twinning in hexagonal close packed alloys

by

Jiaxiang Wang

Twinning can be an essential deformation mechanism in hexagonal close packed (HCP) materials and when it occurs, can significantly change plastic behavior, causing, for instance, noticeable tension and compression asymmetry. In this thesis research, crystal plasticity models, such as elasto-plastic self-consistent (EPSC) model, viscoplastic self-consistent (VPSC) model, and elasto-viscoplastic fast Fourier transformation model, are applied to investigate twin-related hardening mechanisms in HCP alloys. A shared feature of these models is that all models are coupled with dislocation density-based hardening laws, which can predict the underlying dislocation slip activity. How twinning is represented is different among these models. In EPSC and VPSC, a composite grain model is employed to account for twinning, while in EVP-FFT, the intragranular twin domain is model explicitly within the single crystal. Based on their respective advantages, the VPSC and EPSC models are selected to first research dislocation-twin interactions in polycrystalline in commercially pure titanium (CP-Ti) and Mg-Y alloys, and later, the EVP-FFT model is applied for twin-twin interactions within Mg alloy crystals.

As mentioned, in the first part of this research, the EPSC model was employed to study the interaction between slip and twinning in CP-Ti under cyclic loading. There are a variety of active mechanisms in CP-Ti at room temperature, including prismatic $\langle a \rangle$, basal $\langle a \rangle$, pyramidal slip $\langle c + a \rangle$, $\{10\bar{1}2\}$ tensile twin, and $\{11\bar{2}2\}$ compressive twin. A model for the development of a "slip-system-level" backstress due to dislocation density accumulation is included in the EPSC model to advance the model to treat cyclic loading and in particular predict the Bauschinger effect. Material parameters associated with the slip strengths for the three HCP slip modes are determined and newly reported. The model identifies the few systems within the pyramidal slip mode responsible for developing the most backstress among the three slip modes. The analysis also indicates that the backstress that developed in the forward loading path promotes pyramidal slip in the reversal loading path. In addition, reverse loading negligibly changes the relative slip mode contributions from monotonic loading, but it strongly affects the twinning-detwinning behavior. The novel conclusions are that pyramidal slip mode activity and detwinning and their interactions are largely responsible for the strong Bauschinger effect in CP-Ti.

Second, dislocation-twin interactions in Mg-Y alloys are investigated using the VPSC model. The research is motivated by experimental tests on alloys performed elsewhere. The model is applied to understand tests in which the alloys were deformed in tension and compression in the rolling direction and in compression in the normal direction to invoke distinct proportions of slip and twin mechanisms with each test. Within the single-crystal hardening model used in VPSC polycrystal modeling, a slip-twin interaction law is

introduced to account for dislocation density reductions due to dislocation absorption during twin boundary migration. To obtain a more comprehensive understanding, Mg alloys with four different Y concentrations, including Mg 0.2 wt%, Mg 0.6 wt%, Mg 1.0 wt%, and Mg 3.0 wt %, are researched. For each alloy, the model identifies a single set of material parameters that successfully reproduces all measured stress-strain curves and achieves agreement with measured deformation textures and twin area fractions. During deformation, the plastic anisotropy in yield stress, tension-compression asymmetry, and amount of $\{10\bar{1}2\}\langle\bar{1}011\rangle$ twinning is found to decrease with increasing Y. The model interpretation of the flow responses suggests that increased concentrations of Y increase the critical resolved shear stress for basal slip but have negligible effects on the other slip modes. The observed reductions in plastic anisotropy with increases in Y is explained by a concomitant decrease in the prismatic-to-pyramidal slip critical resolved shear stress ratio. The calculations suggest migrating twin boundaries in Mg–Y with different concentrations have the same dislocation absorption rate. Therefore, the chief finding identifies differences in slip strengths among the HCP slip modes as a critical link to macroscale plastic anisotropy.

Finally, the EVP-FFT model was applied to research $\{\bar{1}012\}$ twin-twin interactions in Mg alloys. In the simulation, two non-parallel intersecting twins with the same zone axis are modeled explicitly within a grain (within a polycrystal). These two twins form a co-zone twin-twin junction structure (TTJ). The study reveals important effects the TTJ has on the growth of the impinging twin (IT) and the recipient (RT) twin, as well as the ability of the IT to apparently cross the RT. In addition, the effect of the relative twin thickness between

the IT and RT on these twinning activities is investigated. These TTJ simulations are also performed on three different Mg alloys to reveal the effect of alloy additions on the local stress field produced by the TTJ. The results show that increasing the RT thickness does not affect IT growth, while increasing the IT thickness promotes the reformation of the IT on the other side of the RT, giving the appearance of twin-crossing. The latter apparent crossing is not automatic and requires additional loading to occur. Alloy additions are shown to not significantly alter twin growth mechanisms around the TTJ. However, the formation of non-co-zone twins is more likely to happen in an alloy with low plastic anisotropy.

Table of Contents

List of Figures

List of Tables

1 Introduction and Motivation

1.1 Introduction to HCP Metals

Metals are a group of crystalline materials that have been widely used in the society for structural applications. Most commonly used structural metals, such as aluminum, copper, iron, titanium, magnesium, are found to have a relatively simple crystal structure: face-centered cubic (FCC), body-centered cubic (BCC), or hexagonal close-packed (HCP). Compared with the cubic structures, the latter class of HCP metals are not as widely used, although they bear many excellent properties, many of which can improve energy efficiency and reducing the carbon footprint in the industry. For instance, Ti and Mg are structural materials that are well known for their high specific strength, and Zn is widely used in galvanizing iron and steel products for its superior corrosion resistance. However, the work hardening behavior of HCP metals is less well understood compared to FCC and BCC metals. The complexity in HCP material behavior can be partially attributed to the lower symmetry crystal structure and its associated effect on deformation. Therefore, before going further, a short description of the HCP structure is provided.

In an HCP metal, each atom is situated at the point of the direct lattice. Because the surrounding of each lattice point is the same, the location of lattice points can be described by a primitive unit cell. Figure 1-1 shows the HCP primitive unit cell. All a axes have equal lengths, while c axis length is different and longer. The angle between two neighbors a axes is $\gamma = 120°$ and c axis is perpendicular to the plane construct by the two a axes. The atom positions in the HCP structure are designated in Figure 1-1 by blue

dots. In the ideal case, the atoms are assumed to be hard spheres and close packed. In other words, HCP consists of a stack of close-packed atoms one upon another with a coordination number of 12 and provides a c/a ratio = 1.6333. The actual c/a ratio varies depending on the material. For example, Mg has a c/a ratio =1.623, while Ti has a c/a ratio = 1.587.

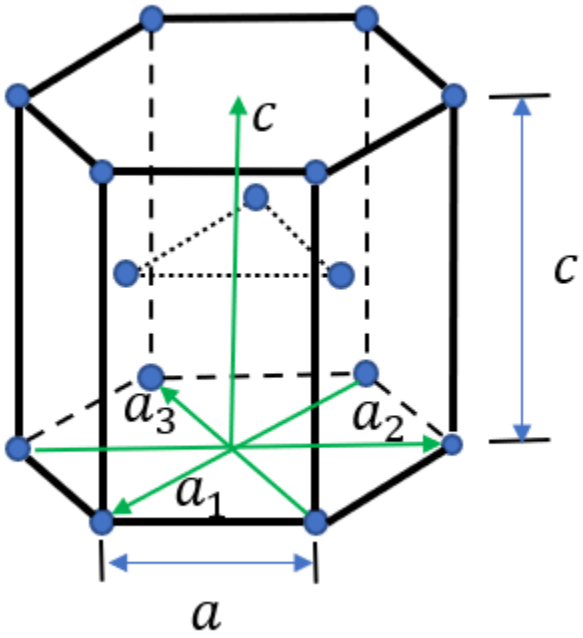

Figure 1-1 Unit cell of the hexagonal close packed structure

1.2 Motivation

The mechanical behavior of metals is determined mainly by the motion of two types of defects, namely dislocations motion and twins. Much pioneering research in this area has brought understanding of the structure and energy of the dislocation cores, stack fault formation and twin growth mechanisms in FCC metals. In the last few decades, metals research has advanced the understanding on the dislocation-dislocation and dislocation-

grain boundary interactions in FCC and BCC metals. Although much work has been dedicated since the 1960's, still comparatively less effort has been dedicated to dislocation-twin, and twin-twin dislocations in HCP materials. Understanding the interaction between different deformation modes can help in understanding the hardening behavior of HCP materials and consequently lead to advances in their performance. The present thesis research twin-slip and twin-twin interactions by extending and applying a suite of crystal plasticity based models. Two kinds of lightweight materials--CP-Ti and Mg alloys-- were selected for this research. Before describing the overarching objectives, in the next chapter, the author will present some background, include the relevant deformation modes, materials, and simulation models.

2 Literature Background

2.1 Deformation mode in HCP Material

In HCP materials, plastic deformation is usually accommodated by slip and twinning. Slip deformation occurs through the motion of dislocations on specific planes and along specific directions, see Figure 2-1. The commonly reported slip systems in HCP materials are basal slip $\langle \boldsymbol{a} \rangle$, prismatic slip $\langle \boldsymbol{a} \rangle$, pyramidal I $\langle \boldsymbol{a} + \boldsymbol{c} \rangle$, and pyramidal II $\langle \boldsymbol{a} + \boldsymbol{c} \rangle$, as show in Figure 2-2(a) (Yoo et al., 2002).

Due to its low symmetry structure, some of these slip systems, namely the $\langle \boldsymbol{a} \rangle$ slip systems, are much easier to activate than the $\langle \boldsymbol{a} + \boldsymbol{c} \rangle$ slip systems. While there appear to be many possible slip systems, the easiest slip systems alone in HCP material are insufficient to satisfy the von Mises Criteria. Specifically, the primary basal slip or

prismatic $\langle \boldsymbol{a} \rangle$ slip systems are incapable of accommodating deformation along $\langle \boldsymbol{c} \rangle$ -axis direction, unlike the pyramidal I $\langle \boldsymbol{a} + \boldsymbol{c} \rangle$ slip systems. However, the mobility of pyramidal slip dislocations is hampered compared to $\langle \boldsymbol{a} \rangle$ slip dislocations, since it may be influenced the non-planar structure of its dislocation core. Thus, additional deformation modes, such as twinning, are required to accommodate $\langle \boldsymbol{c} \rangle$ deformation.

Twinning refers to an atomic displacement in which the atoms on one side of a plane move to a new position that is a mirror-image of the atomic arrangement on the other side. This plane is the twin boundary. Figure 2-3 is a schematic diagram showing the twin within a parent crystalline matrix. As shown, a twin has a distinctly different orientation than the matrix. Twinning involves nucleation, propagation, and thickening process. Twin nucleation refers to the formation of a twin embryo, while the propagation and thickening refer the expansion of the nucleus, including lateral movement of the twin front and transverse migration of the twin boundary.

Twinning has profound effects on several aspects of plastic deformation behavior, such as plastic anisotropy, yield strength and flow stress. The commonly observed twinning modes in HCP material are the $\{10\bar{1}2\}$, $\{11\bar{2}1\}$ extension twin and $\{10\bar{1}1\}$,$\{11\bar{2}2\}$ contraction twin, as show in Figure 2-2(b). The other types of twins can appear as well and which ones dominate depend on the material. They will be discussed next.

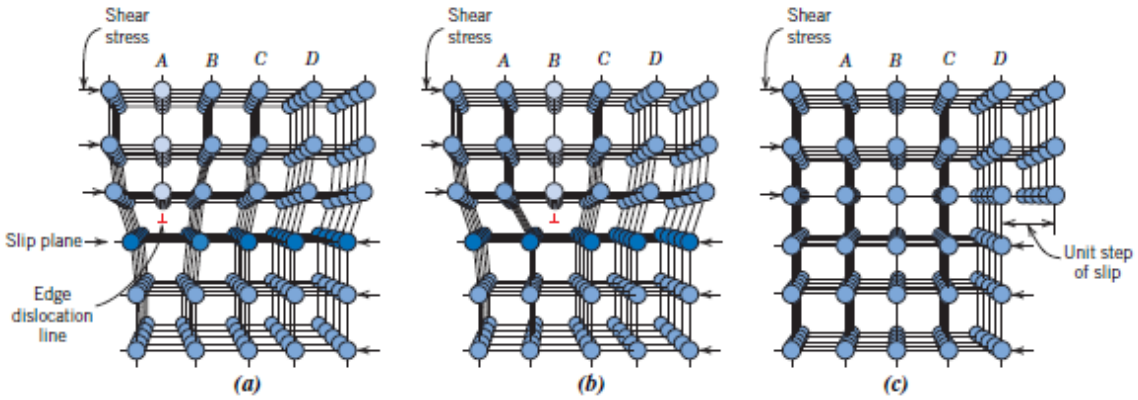

Figure 2-1 Atomic rearrangements that accompany the motion of an edge dislocation as it moves in response to an applied shear stress. This image is taken with permission from Callister and Rethwisch (2013)

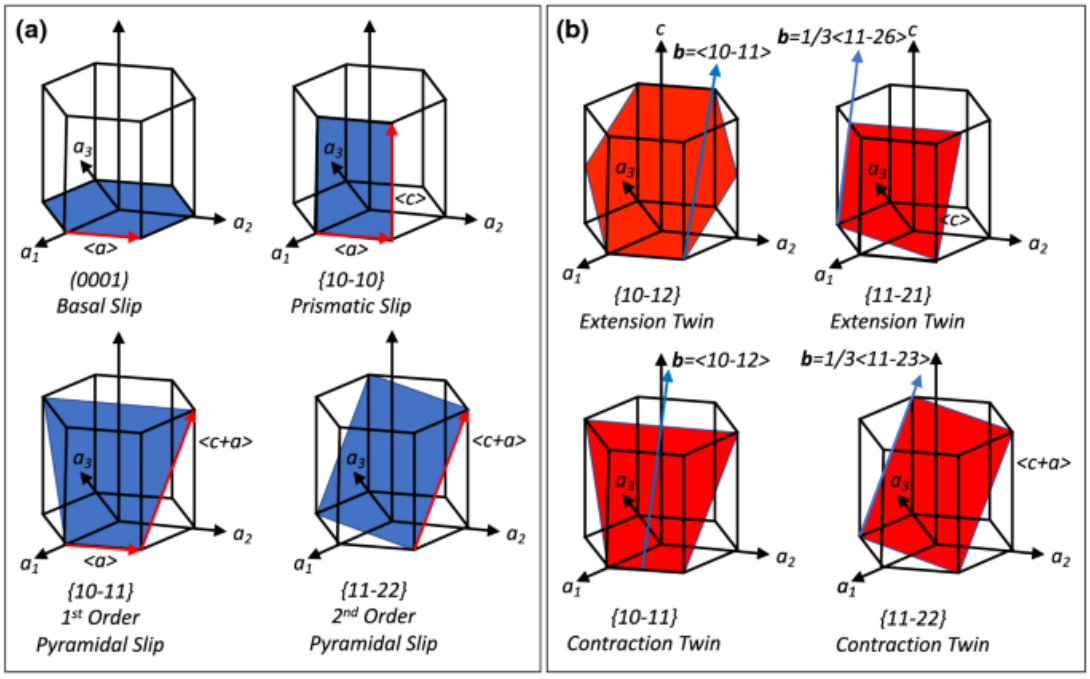

Figure 2-2 Schematic diagram of slip (a) and twinning system(b) in HCP unit cell. This image is taken with permission from Williams et al. (2020)

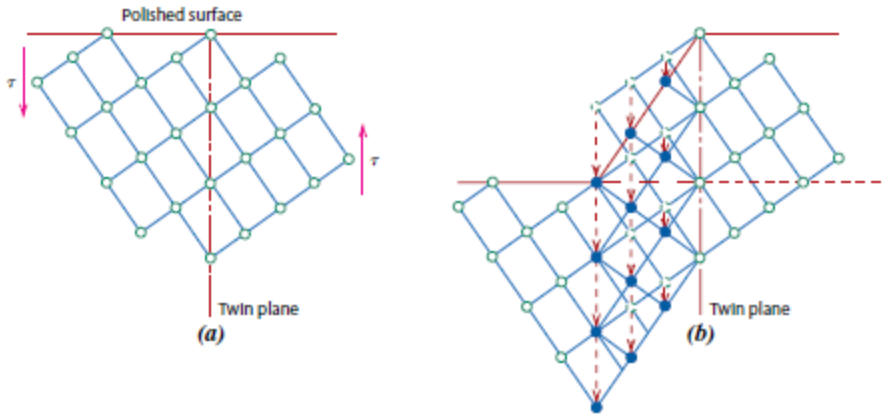

Figure 2-3 Schematic diagram showing how twinning results from an applied shear stress τ. In (b), open circles represent atoms that did not change position; dashed and solid circles represent original and final atom positions, respectively. This image is taken with permission from Callister and Rethwisch (2013)

2.2 Titanium

Titanium is a type of HCP material and is known for its low density, high strength, and excellent biocompatibility. Thanks to these features, Ti and its alloy have been used in many industries, such as aerospace, medical. The response of Ti is governed by the formation and propagation of the two aforementioned defect-driven mechanisms, namely slip and twinning (Becker and Pantleon, 2013; Chichili et al., 1998; Hama et al., 2013; Hosford, 1993; Warwick et al., 2012; Won et al., 2017; Won et al., 2015). Further, slip and twinning have been observed to operate by many modes. For commercially pure titanium (CP-Ti) in ambient conditions, for instance, slip can occur via prismatic $\langle \boldsymbol{a} \rangle$ slip, pyramidal $\langle \boldsymbol{c} + \boldsymbol{a} \rangle$ slip, and basal$\langle \boldsymbol{a} \rangle$ slip (Becker and Pantleon, 2013; Benmhenni et al., 2013; Warwick et al., 2012). At the same time, Ti can also exhibit a large amount of

twinning. For Ti, it has been reported that the number and kind of slip and twinning modes that operate during deformation depend on the load/material orientation relationship and the loading temperature and strain rate (Hama et al., 2015; Paton and Backofen, 1970). This multiplicity in deformation mechanisms renders the macroscopic deformation response of Ti highly anisotropic, and much more temperature and rate sensitive than metals with simpler crystal structures, like body-centered cubic (BCC) and face-centered cubic (FCC).

One goal of this work is to study slip and twinning activity and slip-twin interactions during a load reversal cycle. To this end, CP-Ti is an excellent choice. As mentioned in the introduction, plastic deformation of CP-Ti is accommodated by a multiplicity of slip and twinning modes. At room temperature, $\{10\bar{1}0\}\langle 11\bar{2}0\rangle$ prismatic is believed to be the easiest slip mode to activate. Other possible slip modes are $\{0001\}\langle 11\bar{2}0\rangle$ basal slip, and $\{10\bar{1}1\}\langle 11\bar{2}3\rangle$ pyramidal slip modes (Chichili et al., 1998; Hosford, 1993; Warwick et al., 2012; Won et al., 2017; Won et al., 2015)

Several types of twins have been observed in CP-Ti: $\{10\bar{1}2\}$, $\{11\bar{2}1\}$ extension twins and $\{11\bar{2}2\}$, $\{10\bar{1}1\}$, $\{11\bar{2}4\}$ contraction twins. In the study by Hama et al. (2015) of CP-Ti, twin types and volume fractions were obtained via EBSD. They observed $\{10\bar{1}2\}$ twinning, $\{11\bar{2}2\}$ twinning and $\{11\bar{2}1\}$ twinning during tension in the RD. In high-strain rate conditions, Xu et al. (2012) reported the formation of $\{11\bar{2}2\}$ and $\{11\bar{2}4\}$ twins. A wire-drawn CP-Ti sample test performed by Stanford et al. (2008) observed that $\{10\bar{1}2\}$ extension twinning is the most active extension twin mode and $\{11\bar{2}2\}$ twinning an active

contraction twin mode. Becker and Pantleon (2013) conducted a tensile test based on rolled CP-Ti, which aimed to identify three different work-hardening stages. They found that both $\{11\bar{2}2\}$ twins and $\{10\bar{1}2\}$ twins were activated in the second and third stages. At room temperature, other twin modes, such as $\{11\bar{2}1\}$ extension twinning and $\{10\bar{1}1\}$ contraction twinning, are relatively 8difficult to activate. $\{10\bar{1}1\}$ contraction twinning, for instance, has been reported at temperatures above 300°C. Evidently, from the studies carried out to date, contraction $\{11\bar{2}2\}$ twinning (CTW) and extension $\{10\bar{1}2\}$ twinning (TTW) are common twinning modes for CP-Ti in room temperature deformation. Accordingly, these two twinning modes were made available to the CP-Ti simulation.

2.3 Magnesium

Mg and its alloys are also considered as potential candidates, particularly where a lightweight structural material is needed. Compared to many structural metals, Mg has a low density (1.7g/cm^3) and high specific strength. The known slip systems in Mg are basal $\langle \boldsymbol{a} \rangle$, prismatic$\langle \boldsymbol{a} \rangle$, pyramidal$\langle \boldsymbol{c}+\boldsymbol{a} \rangle$ slip (Yoo, 1981). Among these slip systems, only $\langle \boldsymbol{c}+\boldsymbol{a} \rangle$ dislocations can accommodate strain along the c axis. The $\langle \boldsymbol{c}+\boldsymbol{a} \rangle$ dislocation can either glide on the $\{10\bar{1}1\}$ pyramidal I slip plane (Py1) or $\{11\bar{2}2\}$ pyramidal II plane (Py2)(Xie et al., 2016; Zecevic et al., 2018; Zhang et al., 2018). Alongside dislocation slip, $\{1\bar{0}12\}$ tensile twinning is also frequently observed in Mg. This mode of twinning imposes a shear strain of ~0.13 and adopts the elongation by rotating crystal structure 86° about the $\langle 1\bar{1}20 \rangle$ directions on the $\{10\bar{1}2\}$ planes (Partridge, 1967) .

One strategy to reduce the plastic anisotropy and possibly enhance the performance of Mg is to alter the activation barrier for each slip and twinning mode via alloying. Alloying elements in Mg that increase the CRSS values for basal slip or decrease those for non-basal slip tend to lower the non-basal-to-basal CRSS ratio. Enhanced formability and an increased CRSS for basal slip have been reported in Mg with additions of Al(Ando et al., 2012; Wang et al., 2019), Zn (Ando et al., 2012; Jang and Lee, 2019; Wang et al., 2019) and Sn (Vanderplanken and Deruyttere, 1969). The improved formability with the addition of Li has been attributed to a decreased CRSS for $\langle \boldsymbol{c}+\boldsymbol{a} \rangle$ pyramidal slip (Agnew et al., 2001; Agnew et al., 2002) and an increased CRSS for $\{10\bar{1}2\}\langle\bar{1}011\rangle$ twinning (Lentz et al., 2015b). Moreover, even dilute additions of rare earth elements, such as Y or Ce, can significantly decrease the basal texture and enhance room temperature ductility (Chino et al., 2008a, b; Chino et al., 2009; Hantzsche et al., 2010; Huang et al., 2018; Wu et al., 2018; Zhang et al., 2019b; Zhang et al., 2016). The activity of non-basal deformation modes has been substantially enhanced by rare earth alloying. Some experimental studies have been carried out to study the effect of Y on the behavior of Mg-Y binary alloys. In related studies using transmission electron microscopy (TEM) and density functional theory (DFT) simulations, Sandlöbes et al. (2013; 2012; 2011) reported an increased concentration of $\langle \boldsymbol{c}+\boldsymbol{a} \rangle$ dislocations in binary solid solution Mg-Y, where I1 stacking faults act as a heterogeneous nucleation source for $\langle \boldsymbol{c}+\boldsymbol{a} \rangle$ dislocations. Zhang et al. (2019b; 2016) used in-situ compression in (TEM) to study the CRSS values for slip and twinning modes activated in the Mg-2.5 at. % Y crystal and showed that prismatic slip was favored over

$\{10\bar{1}2\}\langle\bar{1}011\rangle$ twinning in alloys with Y additions. Rikihisa et al. (2017) and Takemoto et al. (2020) observed that the activities of prismatic slip and first-order pyramidal slip increase with increasing Y. In examining different concentrations of Mg-Y (0.2 at. %, 0.3 at. %, 0.8 at. %, 1.2 at. %, and 2.0 at. %), from ambient temperature to 350 °C, Gao et al. (2009) found that the yield strength of Mg-Y increases linearly with c1/2 or c2/3 , where c is the atomic concentration. However, for low concentrations of Y, according to Shi et al., the strengthening effect caused by solute is less than the softening effect by a weaker texture (Shi et al., 2013). In addition, Huang et al. (2018) and Zhao et al. (2019) reported that the macroscopic behavior of Mg-Y is very sensitive to the initial texture and grain size.

2.4 Backstress

The concept of a backstress or long-range internal stress (LRIS) within a deformed material has been discussed in connection with the Bauschinger effect (BE) in many previous works (Kassner et al., 2013a; Mughrabi, 1983; Zecevic and Knezevic, 2015b). The BE (Bauschinger, 1886) is illustrated in Figure 2-4. It refers to a change in the yield strength followed by a rapid hardening in reverse loading. An expression for the backstress σ_b has been proposed following $\sigma_b = (\sigma_f + \sigma_r)/2$ (Kassner et al., 1985), where σ_f is the yield stress in forward loading and σ_r is the yield stress for reverse loading. Several models have been put forward to explain the origin of the backstress. An early explanation by Seeger et al. associated the backstress with dislocation pile ups (Seeger et al., 1957). When dislocations pile up at a cell wall, a high stress of value τ_p acting against the barrier develops. As a result, the wall will impose a negative stress $-\tau_p$ on dislocation. During the reversal loading process, this internal stress $-\tau_p$ now assists plasticity in reverse (Mott,

1952; Seeger et al., 1957). In the early 1980s, another mechanism was proposed by Mughrabi(1983) and Pedersen et al. (1981) that associated the LRIS with the heterogeneous dislocation substructures that develop inside each grain after some amount of deformation. This mechanism is envisioned through the so called “composite model”, which is illustrated in Figure 2-5. As shown, the cells are separated into a hard region with high dislocation density wall and a soft interior region with a low dislocation density. While these two regions are both considered elastic-perfectly plastic and compatible, the hard wall and soft interior will yield differently. When the cell is unloaded in tension, the hard cell wall will compress the soft interior, resulting in the generation of a negative stress in the interior. This negative stress will, in turn, favor plastic deformation and dislocation glide when the macroscopic load subsequently reversed in compression, resulting in a lower flow stress.

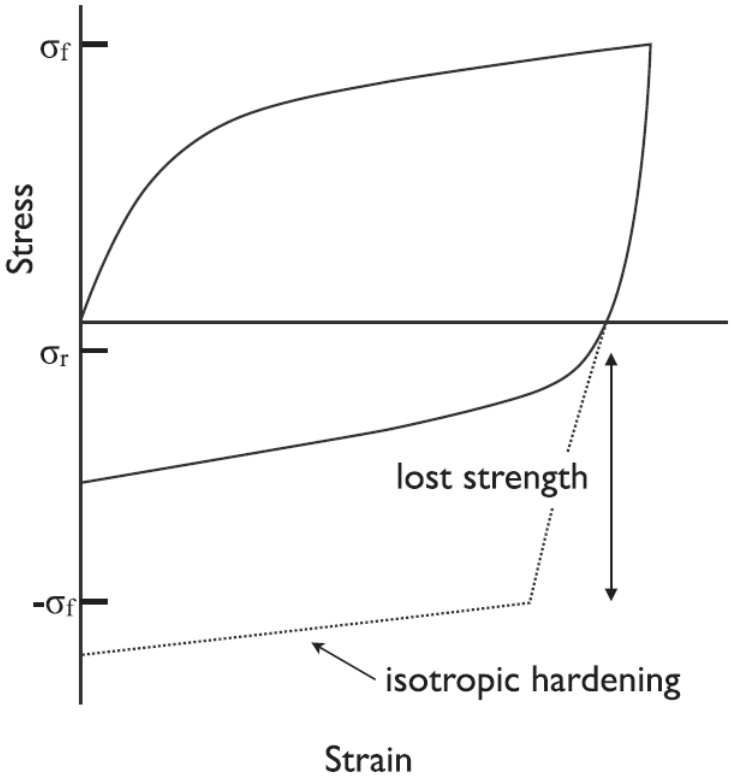

Figure 2-4 A generalized description of the Bauschinger effect. This image is taken with permission from Kassner et al. (2013b).

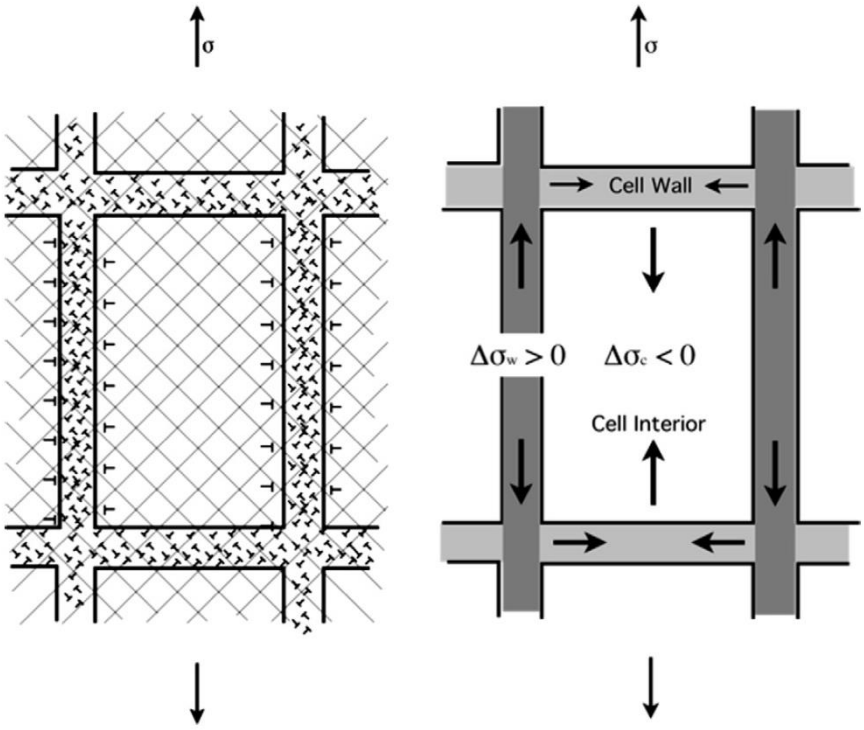

Figure 2-5 The composite model indicating "hard'' regions (high dislocation density) and ''soft'' regions (low dislocation density). Note that interfacial dislocations at the interface allow elastic compatibility and form dipole pairs across the walls. This image is taken with permission from Kassner et al. (2013b).

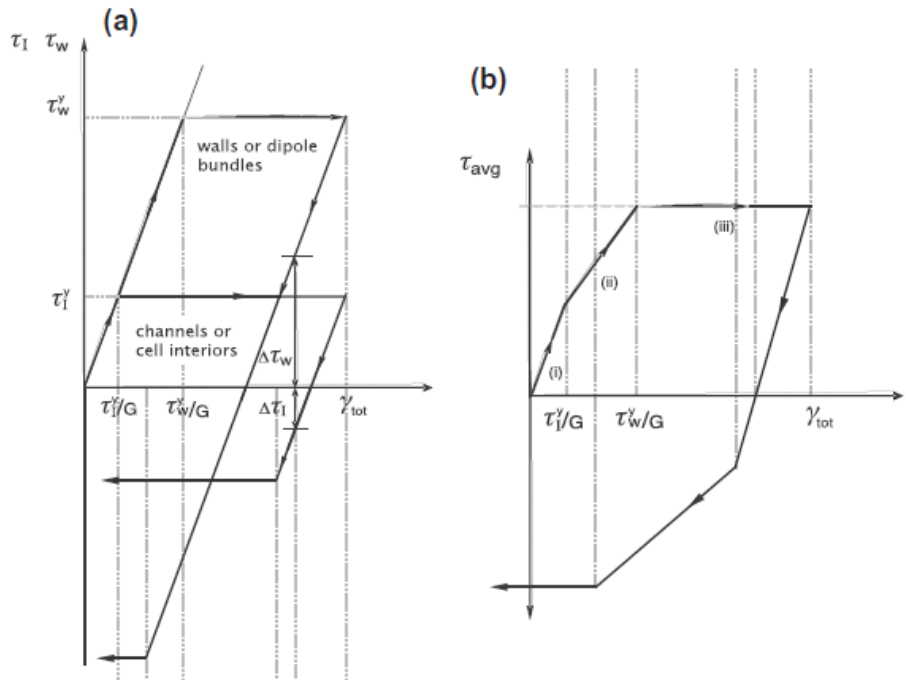

Figure 2-6 The composite model illustrating the Bauschinger effect. The different stress versus strain behaviors of the cell walls and the cell interiors are illustrated in (a), while the stress versus strain behavior of the composite is illustrated in (b). When the composite is completely unloaded, the low dislocation density cell interior region is under compressive (back) stress. This leads to a yielding of this "softer" component in compression at a "macroscopic" stress less than τ_w^y. This image is taken with permission from Kassner et al. (2013b)

2.5 Dislocation-Twin interactions

A considerable amount of work has been devoted to understanding dislocation and twin interactions. Serra et al. (2002) investigated the interaction of the basal slip system with {11-12} and {11-22} twin boundaries. They showed that the edge dislocation will be blocked by the boundary, while a mixed dislocation, with a Burgers vector inclined at 30°

to the dislocation line, will transmit across the twin boundary. Fan et al. (2015) studied the {10-12} tension twin in Mg via a 3-dimensional (3D) discrete dislocation dynamic simulation and found that the TB provides significant resistance to dislocation motion. The barrier effect is usually explained by a Hall-Petch type hardening mechanism and has been used in many crystal plasticity models (Knezevic et al., 2010; Salem et al., 2003). Basinski et al. (1997) found that the hardness of the matrix was lower than that of the twin and the hardness in twin was ascribed to a glissile-to-sessile transformation of the dislocations. This intriguing finding has also been further researched in several subsequent studies. Recent TEM studies observed the basal dislocation in the matrix transforms to a $\langle \boldsymbol{c} + \boldsymbol{a} \rangle$ dislocation inside twin (Wang et al., 2018; Wang and Agnew, 2016). El Kadiri et al.(2013) and Oppedal et al.(2012) use a crystal plasticity model to show that dislocation transmutation induces higher hardening rates in the twin. Besides the transmutation mechanism, dislocation absorption has also been observed in many computer simulation methods. Serra and Bacon (1995) report that screw dislocations will be transformed into a pair of twinning dislocations at the {10-11} twin boundary. Chen et al. (2019) report that when the Burgers vector of a matrix basal (prismatic) dislocation lies parallel to the zone axis of the twin, it will cross slip onto prismatic (basal) plane in the twin. A similar finding has been reported via an in-situ scanning electron microscope (SEM) shear test (Molodov et al., 2017). If the Burgers vector is not parallel to the zone axis, the matrix dislocation will be absorbed (Chen et al., 2019). Using atomistic simulation (Gong et al., 2018a) studied the basal dislocation and 3D {10-12} twin in Mg. Based on this study, it is seen that the dislocation can take different pathways, such as

cross slipping onto the prismatic plane or transmuting into a $\langle \boldsymbol{c} + \boldsymbol{a} \rangle$ dislocation on the prismatic plane, when it reacts with the twin boundary. The type of outcome depends on the dislocation type (edge, screw, or mixed) and the reaction position in twin boundary (coherent twin boundary or lateral twin boundary). Meanwhile, a dislocation can also affect the twinning behavior. Simulation methods investigating the single dislocation-TB reaction have shown that the basal dislocation can decompose at the {10-12} twin boundary and act as a source of twinning dislocations (Hooshmand et al., 2017; Serra and Bacon, 1996; Wang et al., 2014). In contrast, the experiment observations suggest that the TB-dislocation may retard TB migration (Wang et al., 2018; Wang et al., 2014; Xin et al., 2016). The reason could be either the dislocation-TB interaction damages the coherency of the TB, or the transmutation mechanism increases the dislocation density near the twin boundary inside twin.

In summary, the above analysis of the literature to date show that, on the one hand, twinning can affect dislocation behavior in multiple ways. (1) Twinning can reorient the twinned crystal. Thus, an unfavored dislocation in the matrix may be favored and activated in the twin region. (2) The twin boundary can act as a barrier for dislocation slip (Fan et al., 2015; Hong et al., 2010; Knezevic et al., 2010; Salem et al., 2003; Sangid et al., 2012; Serra and Bacon, 1995, 1996; Serra et al., 2002),. (3) Dislocation transmutation can occur (El Kadiri et al., 2013; Molodov et al., 2017; Oppedal et al., 2012; Wang et al., 2018; Wang and Agnew, 2016). (4) The dislocation may be absorbed by the twin boundary (Chen et al., 2019; Serra and Bacon, 1995, 1996; Serra et al., 1999). On the other hand, the twin boundary migration will also be significantly influenced by the dislocations surround twin

(Hooshmand et al., 2017; Serra and Bacon, 1996; Wang et al., 2018; Wang et al., 2014; Xin et al., 2016).

2.6 Twin-twin Interactions

A twinned crystal is commonly divided into an untwinned matrix and multiple parallel twins of the same twin variant (Arul Kumar et al., 2019; Beyerlein et al., 2010; Beyerlein and Tomé, 2008; Kumar et al., 2016). However, non-parallel twins with various twin variants can be activated and can interact with each other. Twin-twin interactions (TTI) between non-parallel twins can lead to the formation of twin-twin junctions (TTJ) and a 3D twin network structure (El Kadiri et al., 2013; Juan et al., 2015; Kumar et al., 2019; Sun et al., 2015a; Yu et al., 2014a). Roberts and Partridge (1966) experimentally characterized the twin-twin boundaries (TTBs) between $\{10\bar{1}2\}$ twin in Mg and identify it as a common interface bisection two twinning plane. Yu et al. (2014a) classified $\{10\bar{1}2\}$ TTJs either as a co-zone TTJ (twin variants sharing the same zone axis) or a non-co-zone TTJ (two twin variants with different zone axes) and investigated the character of the associated TTBs. Three different types of twin-twin structures are observed by TEM, i.e., a quilted-looking twin structure, an “apparent crossing” twin structure, and a double twin structure. The TTBs of co-zone TTJs were identified as either (10-10) or (0001) planes corresponding to the prismatic-prismatic (PP) and basal-basal (BB) boundary. Subsequent molecular dynamics (MD) simulation demonstrated the formation of the two TTBs (Yu et al., 2014b).

Recent research has shown that twin junctions can play a distinctive role compared to isolated twins in what concerns interactions with glide dislocations, further twinning, and

local strain hardening. El Kadiri et al (2013) compared the twin nucleation and growth behavior between two grains that contain different numbers of twin variants. They found the grain in two twin variant condition has a higher twin nucleation rate and lower twin thickening rate than the other grain only has one twin variant. Morrow et al. (Morrow et al., 2014a; Morrow et al., 2014b) found that the TTBs retard the detwinning process under cyclic loading. Local stress field analysis, such as MD at atomic level and crystal plasticity model at meso-scale, has also been applied to research the effect of TTJs on primary twin twinning, secondary twinning and slip bands (Gong et al., 2018b; Kumar et al., 2019; Yu et al., 2014b). Applying the MD simulation, Yu et al. (2014b) revealed that co-zone TTJ will facilitate the propagation of a basal slip band; Gong et al. (2018b) explain the abnormal twin boundary migration on two side of TTJ. Kumar et al. (2019) calculate the stress field around the $\{10\bar{1}2\}$ co-zone TTJ using the elasto-viscoplastic fast Fourier transformation (EVP-FFT). This work provides a possible explanation of twin "reach out", an observation wherein the recipient twin boundary appears to migrate towards the incoming twin. It also suggested that a new twin is likely to nucleate on the other side of the recipient twin boundary. In addition, microcrack often observed along the secondary twin boundary indicate that TTJ may also be related to the fracture initiation (Yu et al., 2015).

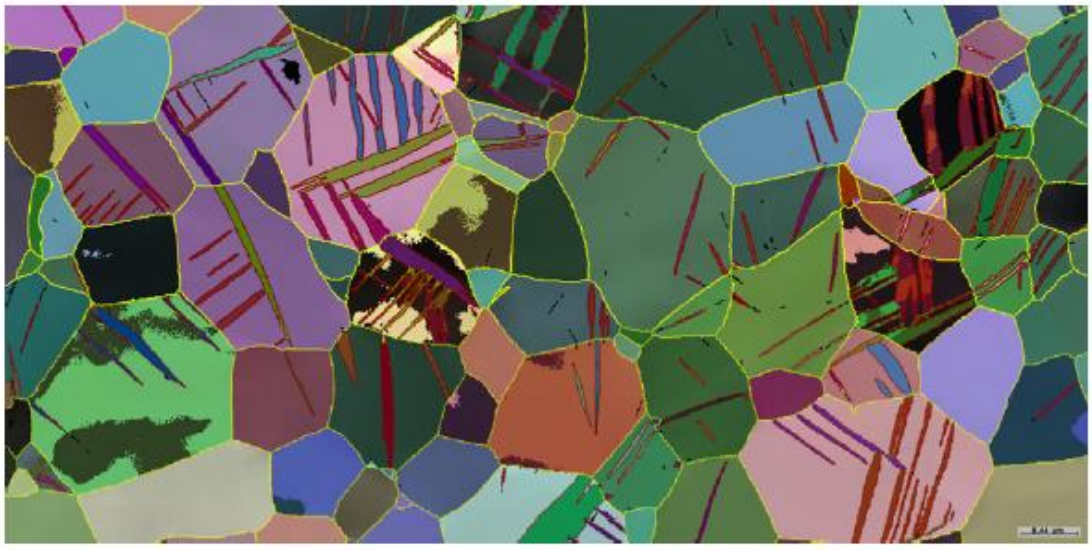

Figure 2-7 A typical EBSD scan of HCP polycrystalline specimens loaded in compression. This image is taken with permission from (Juan et al., 2015)

2.7 Crystal plasticity

Crystal plasticity models are physics-based models that are often used for simulating and understanding the deformation behavior of a strained single crystal or polycrystalline material. Polycrystal plasticity models usually employ a combination of crystal plasticity (CP) theory and a type of homogenization scheme. Full-field crystal plasticity mechanics tools, on the other hand, combine CP theory to dictate the constitutive law at each integration or Fourier point. In both cases, CP theory links the deformation of a single crystal with the glide of a dislocation on slip systems. Thus, some microscopic physical quantities, such as slip resistance for these slip systems and orientation of the crystal, may be needed as input for the CP model. The two kinds of CP models are described in detail below.

Mean-field techniques, including the full constraint Taylor model and self-consistent schemes, homogenize the neighborhood of an individual grain, therefore improving computation efficiency compared with the spatially resolved model. The mean-field model can be used to predict the evolution of crystallographic orientation of the grain, the macroscopic stress-strain response, and relative activities of the deformation modes. The two often used models are the viscoplastic self-consistent (VPSC) (Beyerlein and Tomé, 2008) and elastoplastic self-consistent model (EPSC) (Zecevic and Knezevic, 2015b). In these two models, the polycrystal are regarded by a collection of orientations (grains) with associated volume fractions. The single grain can be represented by an ellipsoidal inclusion embedded in the homogeneous effective medium (HEM), which has the average properties of the polycrystal. The difference between VPSC and EPSC is that VPSC does not account the elastic deformation, while the EPSC account both elasticity and plasticity. More details on these two techniques will be given in chapters 4 and 5.

The full-field approach spatially resolves the grain interiors and their neighborhoods and thus, it can calculate the inter- and intragranular mechanical fields within the deformed microstructure. This important ability allows it to provide addition information compared with the mean-field approach. For instance, it has been used to research grain-to-grain interactions, the stress state inside grains and stress across grain boundaries. This approach usually makes use of either one of many finite element solvers or the fast Fourier transform solver. The former is the well-known crystal plasticity finite element (CP-FE) model and the latter one is the new elasto-viscoplastic fast Fourier transform (EVP-FFT) model.

In any of these CP models, a hardening law is required. Earlier hardening laws were phenomenological based functions, while most of the recently developed law, were based on an evolving dislocation density. For instance, a thermally activated dislocation density based hardening law (DD model) for HCP metals was developed by Beyerlein and Tomé (Beyerlein and Tomé, 2008). In this model, work hardening is linked to the evolution of dislocations, their mutual interactions, and their interactions with barriers in the microstructure. The threshold shear stress for slip τ_c^s, including contributions from forest dislocations, debris, and twin boundaries, is expressed as:

$$\tau_{\mathrm{c}}^{\mathrm{s}} = \tau_0^{\alpha} + \tau_{\mathrm{for}}^{\mathrm{s}} + \tau_{\mathrm{deb}}^{\mathrm{s}} + \tau_{HP}^{s} \qquad 2\text{-}1$$

where the initial slip resistance τ_0^{α} depends on slip mode α, solute density, and temperature T and strain rate $\dot{\varepsilon}$. The resistances, τ_{for}^{s} and τ_{deb}^{s}, are the forest dislocation interaction stress and dislocation substructure interaction stress. The last term τ_{HP}^{s} is the barrier effect provided by twin boundaries. Since the experiment is performed at fixed strain rate and temperature, the initial resistance is assumed to be a constant which can be adjusted. The evolution of τ_{for}^{s} follows the traditional Taylor law, meaning it scales as the square root of dislocation density (Kocks and Mecking, 1981; Lavrentev, 1980):

$$\tau_{for}^{s} = b^{\alpha}\chi\mu\sqrt{\rho_{for}^{s}} \qquad 2\text{-}2$$

where $\chi, \mu, and\ b^{\alpha}$ are the dislocation interaction parameter, effective shear modulus, and the value of the Burgers vector of mode α. The parameter χ is usually ranges in $0.1 < \chi < 1.0$, and conventionally set to 0.9. The density ρ_{for}^{s} is the forest dislocation density, which is governed by the following equation:

$$\frac{\partial \rho^{\alpha}}{\partial \gamma^{\alpha}} = \frac{\partial \rho_{gen,for}^{s}}{\partial \gamma^{s}} - \frac{\partial \rho_{rem,for}^{s}}{\partial \gamma^{s}} = k_1^{\alpha}\sqrt{\rho^{\alpha}} - k_2^{\alpha}\rho^{\alpha} \qquad 2\text{-}3$$

where k_1^{α} is a rate-insensitive coefficient for dislocation storage by statistical trapping of mobile dislocation and k_2^{α} is the coefficient for dynamic recovery by thermally activated mechanisms(Essmann and Mughrabi, 1979; Kocks and Mecking, 2003). Their ratio can be expressed as:

$$\frac{k_2^{\alpha}}{k_1^{\alpha}} = \frac{\chi b^{\alpha}}{g^{\alpha}}\left(1 - \frac{kT}{D^{\alpha}b^{3}}\ln\left(\frac{\dot{\varepsilon}}{\dot{\varepsilon}_0}\right)\right) \qquad 2\text{-}4$$

where $k, \dot{\varepsilon_0}, g^{\alpha} \text{and}\ D^{\alpha}$ are the Boltzmann constant, a strain rate related to the number of attempts and Debye frequency, an effective activation enthalpy, and drag stress. The stress τ_{deb}^{α} represents the hardening contribution of dislocation stored in substructure as found in dislocation dynamics studies by Basinski (1974).

$$\tau_{\mathrm{deb}}^{\alpha} = k_{\mathrm{deb}}\mu b^{\alpha}\sqrt{\rho}\log\left(\frac{1}{b^{\alpha}\sqrt{\rho_{\mathrm{deb}}}}\right) \qquad 2\text{-}5$$

Here, $k_{deb} = 0.086$ is a material-independent constant determined to be 0.086. The evolution of the debris density ρ_{deb} governed by the rate of recovery of all active dislocations via:

$$\partial \rho_{deb,tot} = \sum_{\alpha} Q^{\alpha} b^{\alpha} \sqrt{\rho_{deb}} \frac{\partial \rho^{\alpha}_{rem,for}}{\partial \gamma^{\alpha}} d\gamma^{\alpha} \qquad 2\text{-}6$$

where Q^{α} is a dislocation recovery rate that quantifies the fraction of dislocation stored as substructure. The τ^{α}_{HP} models the barrier effect on slip imposed by the twin boundaries through a Hall-Petch like relationship, which is

$$\tau^{s}_{HP} = \mu H P^{\alpha\beta} \sqrt{\frac{b^{\alpha}}{d^{s,PTS}_{mfp}}} \quad s \in \alpha \text{ with } \beta - \text{type PTS} \qquad 2\text{-}7$$

Here, $HP^{\alpha\beta}$ is a Hall-Petch like coefficient.

To model the reorientation caused by twinning, twin evolution, and the twin barrier effect caused by the twin boundary, the uncoupled version of the Composite grain (CG) twin model has been used (Beyerlein and Tomé, 2008; Proust et al., 2007; Tomé and Kaschner, 2005). In this model, when the volume fraction $f^{t} = \frac{\Delta\gamma^{t}}{s}$ in a system reaches a threshold (5%), this system is then selected as the predominant twin system (PTS) in the grain, where $\Delta\gamma$ is the shear contributed by the twin system and S is the characteristic twin shear. The grain is then divided into a matrix and a twin region when the volume fraction in the PTS reaches a critical value. Twin and matrix regions are treated as ellipsoids that interact only with the effective medium and not directly with each other during the deformation

process. In all grains, the twinned regions are assumed to be equally spaced and have equal thickness. The parameter d_c defines the center-to-center spacing between neighboring twins. The d_t is the evolving twin width, and d_g is the grain size. As reported by previous work (Proust et al., 2007), d_c is 0.2 d_g for tensile twinning and 0.05 d_g for compressive twinning. A key element in the CG model is the mean free path (d_{mfp}), which is defined by the combined crystallography of the PTS and that of the other slip or twin systems. The $dmfp$ enters in the hardening law and evolves with twin activity from a maximum d_{mfp} = d_g (when no twin is present) to a minimum of d_t. Twin resistance calculated in the model is assumed to be driven by a shear stress calculated by resolving the stress in the twin direction and twin plane. The critical value to grow the twin corresponds to a critical propagation stress τ^t , which is, in principle, can be considered the same for each twin system *t* but different between twin modes β.

3 Thesis Objectives

The objective of this thesis work is three-fold. The first aim is to reveal the effect of dislocation activity on twinning and detwinning: An EPSC model was presented to determine the amounts of slip and twinning in each step and whether the mechanisms operating in forward loading alter in reverse loading. The effect of dislocation activity on deformation twinning and detwinning behavior was studied. The second objective is to elucidate the effect of twin boundaries on dislocation behavior. To this end, a VPSC model was presented to study the hardening or softening effect on dislocation slip caused by twinning. Different Mg alloys were investigated to research the alloying effect on this TB-

dislocation interaction. The final goal is to understand the interaction between twin and twin. An EVP-FFT model is presented to study the stress field and dislocation field around TTJ. Different Mg alloys were inspected to research the alloying effect on the TTJ formation and subsequent growth.

The rest of the thesis is structured as follows. In Chapter 4, the EPSC model is applied to research the slip, twinning, and detwinning behavior in CP-Ti during the cyclic loading process. A slip-system level backstress law is incorporated in the model to enhance the performance of the model in cyclic loading. In Chapter 5, the VPSC model is utilized to research the interactions between twin boundary and dislocation. As mentioned, the VPSC model does not include elastic deformation. However, in this study, Mg alloys were compressed to a relatively large strain level, so the elastic regime is less important. In Chapter 6, the EVP-FFT model is employed to investigate TTJ structure and development in different alloys. Every Chapter 4 to 6 will provide research motivation, description of the model formulation and new model developments, the simulation set up, and any descriptions of the experimental results used for validation, before presenting the modeling results and analysis. In Chapter 7, an overall summary of the thesis research and the recommendations for further research are presented.

4 Commercially pure titanium (CP-Ti) under strain reversals

4.1 Motivation

For modeling constitutive response under strain path changes, self-consistent formulations involving advanced constitutive laws have recently been developed. Of

special note, some works, combined VPSC with a dislocation based hardening law to model the Bauschinger effect (BE) and subsequent working hardening rate upon strain reversal (Kitayama et al., 2013; Knezevic et al., 2013; Wen et al., 2015). To capture the reverse hardening rate, this model introduced a reversible dislocation population that accumulates in prestraining and annihilates upon strain reversal. However, these models did not account for elastic deformation, and they did not link dislocation motion to the development of backstresses. To account for elasticity, prior attempts for modeling load reversals have also involved the elasto-plastic self-consistent (EPSC) or elasto-plastic self-consistent (EVPSC) model (Lorentzen et al., 2002; Ma et al., 2019). It was shown in Lorentzen et al. (2002) that even with inter-granular backstresses (type II stresses) taken into account, EPSC was still insufficient in predicting the behavior of stainless steel under cyclic deformation. By incorporating a slip-system-level backstress evolution law for intra-granular stresses (type III stresses), the EPSC model was able to capture subsequent hardening behavior under the reverse strain path change (Zecevic and Knezevic, 2015a, 2018). To date, this EPSC scheme with inter- and intra-granular stresses has been applied to model the large strain cyclic deformation of a dual phase steel DP590 (Zecevic et al., 2016) and the Inconel 718 Ni-based superalloy (Ghorbanpour et al., 2017). These studies, however, treated materials with either an FCC or BCC crystal structure. For modeling load reversal sequences in HCP materials, like Ti and Mg, the interactions of twinning and detwinning with elasticity, multiple slip modes, and type III backstress development need to also be taken into account.

In this chapter, an EPSC model that accounts for dislocation density-based hardening on slip systems, inter- and intra-granular stresses backstress evolution due to slip, and subgrain reorientation due to twinning and detwinning is presented. The aim of this model advancement is to apply it to commercially pure titanium (CP-Ti) to understand and evaluate the mechanisms underlying its deformation response in load reversals. The model is developed to incorporate the multiple slip modes and multiple twinning modes commonly associated with the deformation of CP-Ti. Forward-reverse stress-strain data are taken from an earlier work (Hama et al., 2015), which includes texture evolution and different loading sequences and amounts of strains. Notably, in the present thesis research, only one set of material parameters is characterized for all data sets.

4.2 EPSC background

Details of EPSC are briefly reviewed in this section, following the formulation given in. In EPSC, the polycrystal is represented by a set of grains. Each grain is treated as an elasto-plastic inclusion embedded in a homogeneous equivalent matrix (HEM). The mechanics of the inclusion are solved using a Green's function approach and the individual grains interact only with the HEM. Each grain, embedded in a polycrystal, has a distinct crystallographic lattice orientation and volume fraction. In EPSC, a linearized relationship is employed at the scale of the individual grain, in which the Jaumann stress rate, $\hat{\boldsymbol{\sigma}}$, and the strain rate in grain c, $\dot{\boldsymbol{\varepsilon}}$ are related by:

$$\hat{\boldsymbol{\sigma}} = \mathbf{L}^{c}\, \dot{\boldsymbol{\varepsilon}}^{c} \qquad 4\text{-}1$$

where the tensor $\mathbf{L}^c$ is the instantaneous stiffness of the grain *c*. The macroscopic, polycrystalline Jaumann stress rate and strain rate are equal to the volume average of the Jaumann grain stress and strain rate, i.e.,$\widehat{\boldsymbol{\sigma}} =< \widehat{\boldsymbol{\sigma}}^{\mathbf{c}} >$and $\dot{\boldsymbol{\varepsilon}} =< \dot{\boldsymbol{\varepsilon}}^{\mathbf{c}} >$ and therefore, their relationship is also linear and given by:

$$\widehat{\boldsymbol{\sigma}} = \mathbf{L}\dot{\boldsymbol{\varepsilon}} \qquad 4\text{-}2$$

where $\mathbf{L}$ is the unknown instantaneous elasto-plastic stiffness tensor of the HEM. As will be described shortly, $\mathbf{L}$ is calculated iteratively using the self-consistent procedure. The macroscale Cauchy stress rate $\dot{\boldsymbol{\sigma}}$ is related to the macroscale Jaumann stress rate $\hat{\dot{\boldsymbol{\sigma}}}$ via

$$\dot{\boldsymbol{\sigma}} = \widehat{\boldsymbol{\sigma}} + < \mathbf{W}^{\mathbf{c}}\boldsymbol{\sigma}^{\mathbf{c}} > - < \boldsymbol{\sigma}^{c}\mathbf{W}^{\mathbf{c}} > = \mathbf{L}\dot{\boldsymbol{\varepsilon}} + < \mathbf{w}^{\mathbf{c}}\boldsymbol{\sigma}^{\mathbf{c}} > - < \boldsymbol{\sigma}^{\mathbf{c}}\mathbf{W}^{\mathbf{c}} > \qquad 4\text{-}3$$

where $\mathbf{W}^{\mathbf{c}}$ is elastic spin of crystal, c. The Cauchy stress $\boldsymbol{\sigma}$ is determined by explicit integration of the Cauchy stress rate $\dot{\boldsymbol{\sigma}}$ at the end of each time increment.

The response of each grain c follows from solving the stress equilibrium and compatibility relations for an inclusion embedded in a homogeneous anisotropic matrix under applied loads. The stress and strain rate in a grain is related to those in the macroscopic medium through the following interaction equation

$$\widehat{\boldsymbol{\sigma}}^{c} - \boldsymbol{\sigma} = -\boldsymbol{L}^{c^*}(\dot{\boldsymbol{\varepsilon}}^{c} - \dot{\boldsymbol{\varepsilon}}) \qquad 4\text{-}4$$

where $\mathbf{L}^{c^*} = \mathbf{L}(\mathbf{S}^{c^{-1}} - \mathbf{I})$ is the effective stiffness. $\mathbf{S}^{c}$ is the symmetric portion of Eshelby tensor and $\mathbf{I}$ is the fourth-ranked identity matrix. The equation for the grain scale strain then follows:

$$\dot{\boldsymbol{\varepsilon}}^{\mathbf{c}} = \mathbf{A}^{\mathbf{c}}\dot{\boldsymbol{\varepsilon}} \qquad 4\text{-}5$$

where $\mathrm{A}^{\mathrm{c}} = \left(\mathbf{L}^{\mathrm{c}} + \mathbf{L}^{\mathrm{c}^*}\right)^{-1}(\mathbf{L}^{\mathrm{c}^*} + \mathbf{L}^{\mathrm{c}^*})$, and $\mathbf{L} =< \mathbf{L}^{\mathrm{c}}\mathbf{A}^{\mathrm{c}} >< \mathbf{A}^{\mathrm{c}} >^{-1}$. From prior work by Wollmershauser et al. (2012) the driving force (resolved shear stress) for the activation of slip system is influenced by the applied loading, inter-granular stresses originating from the EPSC description of grain interaction, $\mathbf{m}^{\mathrm{c,s}}$, and the slip system intra-granular backstress $\tau_{bs}^{c,s}$. In the work, $\mathbf{m}^{\mathrm{c,s}}$ is the Schmid tensor, which is given by $\mathbf{m}^{\mathrm{c,s}} = 0.5(\mathbf{b}^{\mathrm{c,s}} \otimes \mathbf{n}^{\mathrm{c,s}} + \mathbf{n}^{\mathrm{c,s}} \otimes \mathbf{b}^{\mathrm{c,s}})$, where $\mathbf{b}^{\mathrm{c,s}}$ and $\mathbf{n}^{\mathrm{c,s}}$ are the slip direction and slip plane normal. Two conditions must be satisfied: (1) $\mathbf{m}^{\mathrm{c,s}} \cdot \boldsymbol{\sigma}^{\mathrm{c}} - \tau_{bs}^{\mathrm{c,s}} = \tau_{c}^{\mathrm{c,s}}$ meaning that the resolved shear stress reduced by the value of backstress reaches the value of slip resistance and (2) $\mathbf{m}^{\mathrm{c,s}} \cdot \hat{\boldsymbol{\sigma}}^{c} - \dot{\tau}_{bs}^{\mathrm{c,s}} = \dot{\tau}_{c}^{\mathrm{c,s}}$, meaning that the stress has to remain on the single crystal yield surface, which evolves due to hardening. The hardening matrix, $h^{ss'}$ and backstress interaction matrix, $h_{bs}^{ss'}$ are introduced to account for any coupling between the rate of slip resistance $\dot{\tau}_{c}^{\mathrm{c,s}}$, and $\dot{\tau}_{bs}^{\mathrm{c,s}}$ rate of backstress, respectively, to the slip rate on other active slip systems through:

$$\dot{\tau}_{c}^{\mathrm{c,s}} = \sum_{s} h^{ss'}\dot{\gamma}^{c,s'} \qquad 4\text{-}6$$

$$\dot{\tau}_{bs}^{\mathrm{c,s}} = \sum_{s'} h_{bs}^{ss'}\dot{\gamma}^{c,s'} \qquad 4\text{-}7$$

For the individual grain *c*, the stress increment and strain increment also follow a constitutive relation given by

$$\hat{\boldsymbol{\sigma}}^{\mathrm{c}} = \mathbf{C}^{\mathrm{c}}\left(\dot{\boldsymbol{\varepsilon}}^{\mathrm{c}} - \sum_{\mathrm{s}} \mathbf{m}^{\mathrm{c,s}}\dot{\gamma}^{\mathrm{c,s}}\right) - \boldsymbol{\sigma}^{\mathrm{c}}\mathrm{tr}(\dot{\boldsymbol{\varepsilon}}^{\mathrm{c}}) \qquad 4\text{-}8$$

where $\boldsymbol{C}^{c}$ is the single crystal elastic stiffness tensor and $\sum_{s} \boldsymbol{m}^{c,s}\dot{\gamma}^{c,s}$, is the plastic strain rate comprised of the slip system shear rates. From Eqs. 4-5, 4-6,and 4-8, the grain stiffness becomes:

$$\mathbf{L^{c}} = \mathbf{C^{c}} - \mathbf{C^{c}} \sum_{\mathbf{s}} \mathbf{m^{c,s}} \otimes \left(\sum_{\mathbf{s'}} \left(\mathbf{X^{ss'}}\right)^{-1} \mathbf{m^{c,s'}} \left(\mathbf{C^{c}} - \boldsymbol{\sigma}^{\mathbf{c}} \otimes \mathbf{i}\right) - \boldsymbol{\sigma}^{\mathbf{c}} \otimes \mathbf{i}\right) \qquad 4\text{-}9$$

where $\mathbf{i}$ is a second rank identity tensor. The definition of $\mathrm{X}^{\mathrm{ss'}}$ can be expressed as follows

$$\mathrm{X}^{\mathrm{ss'}} = \mathrm{h}^{\mathrm{ss'}} + \mathrm{h}_{\mathrm{bs}}^{\mathrm{ss'}} + \mathbf{C}^{\mathrm{c}} \cdot \mathbf{m}^{\mathrm{c,s}} \otimes \mathbf{m}^{\mathrm{c,s'}} \qquad 4\text{-}10$$

The crystallographic texture evolution calculation is given below in Eq. 4-11 and Eq. 4-12

$$\mathbf{W}^{\mathrm{p,c}} = \sum_{\mathbf{s}} \dot{\gamma}^{\mathrm{c,s}} \mathbf{q}^{\mathrm{c,s}} \qquad 4\text{-}11$$

The tensor $\mathbf{q}^{c,s}$ is the unit slip system tensor ($\mathbf{q}^{\mathrm{c,s}} = 0.5(\mathbf{b}^{\mathrm{c,s}} \otimes \mathbf{n}^{\mathrm{c,s}} - \mathbf{n}^{\mathrm{c,s}} \otimes \mathbf{b}^{\mathrm{c,s}})$), and $\boldsymbol{W}^{p}$ is the plastic rotation rate for each crystal.

$$\mathbf{W}^{\mathrm{c}} = \mathbf{W}^{\mathrm{app}} + \boldsymbol{\Pi}^{\mathrm{c}} - \mathbf{W}^{\mathrm{p,c}} \qquad 4\text{-}12$$

where $\mathbf{W}^{\mathrm{app}}$ is the macroscopically applied rotation rate and $\boldsymbol{\Pi}$ is the reorientation contribution from the anti-symmetric part of the Eshelby tensor. The tensor $\mathbf{W}^{\mathrm{c}}$ is the lattice rotation rate, which is used to update the crystal orientation and hence evolve the texture.

4.2.1 Backstress evolution law

For the calculations, the adaption of the slip-level backstress evolution law introduced in (Zecevic and Knezevic, 2015a) for an FCC aluminum alloy to HCP CP-Ti is described first.

The law presumes that backstresses develop as dislocations accumulate with strain. Backstresses are directional and depend on the sense of shear responsible for storing or releasing dislocations in the crystal. Dislocations gliding in one direction can generate backstresses that resist slip in the same sense of direction but aid slip in the opposite sense. A positive backstress on slip system *s* acts against it and a negative backstress on *s* acts in favor of it. The backstress model is briefly reviewed here for the purposes of introducing the associated parameters.

When slip is activated on the s^+ system, i.e., $d\gamma^{s^+} > 0$, then the backstress $\tau_{bs}^{s^+}$ evolves according to:

$$\tau_{bs}^{s^+} = \tau_{bs}^{sat}(1 - \exp(-v\gamma^{s^+})) \qquad 4\text{-}13$$

The strain γ^{s^+} also generates a negative backstress $\tau_{bs}^{s^-}$ on the slip system s^-.

$$\tau_{bs}^{s^-} = -A\tau_{bs}^{s^+} \qquad 4\text{-}14$$

The value of A is an asymmetry parameter and v controls the rate at which the backstress reaches the saturation value τ_{bs}^{sat}. When $A = 1$, then backstresses caused by $d\gamma^{s^+} > 0$ generate an equal but negative backstress on s^-. If the stress available to re-emit or re-mobilize piled up dislocations is larger than that which resists them, then A will be larger than unity but is generally of order $1 - 10$.

In reversal, the slip system s^- becomes active,$d\gamma^{s^-} > 0$, and the backstress $\tau_{bs}^{s^+}$ decays from the value τ_{bs0}^{+} accumulated at the point of reversal. Physically, this reduction is

interpreted as dislocations once piled up are now reemitted or remobilized in reverse. The empirical function governing this decay is given by:

$$\tau_{bs}^{s^+} = -A\tau_{bs}^{s^-} \tag{4-15}$$

and

$$\tau_{bs}^{s^-} = -(A+1)\tau_{bs0}^{s^+} \exp\left(-\frac{\gamma^{s^-}}{\gamma_b}\right) + \tau_{bs0}^{s^+} \tag{4-16}$$

where the rate of decay is governed by γ_b. The parameters A, ν, and γ_b are related to dislocation accumulation and the stress fields produced by clusters of them. As such, it is assumed they depend on the type of dislocation, and hence differ among slip modes but are the same for individual systems belonging to the same mode.

4.2.2 The twinning model

As a novel feature of this thesis work, a backstress-twinning interaction component is introduced. To begin, it is first recognized that the model assumes a twin resistance to twin propagation calculated in the model as a critical value of the shear stress resolved in the twin direction and twin plane. This critical threshold for twin system *t* in twin mode β consists of the sum of two different terms:

$$\tau_c^s = \tau_0^\beta + \tau_{slip}^\beta \quad t \in \beta \tag{4-17}$$

In Eq. 4-17, and the following equation, β represents the twin mode. The first term τ_0^β is the propagation resistance without interactions with other dislocations and the resistive

effects of grain or twin boundaries. The twin variant that lies in the grain as reoriented lamellae is referred to as the predominant twin system (PTS).

The second term in Eq. 4-17 represents the contribution to hardening for all twin systems due to interactions with slip dislocations. It can increase proportionally with the dislocation population according to

$$\tau_{slip}^{\beta} = \mu \sum_{\alpha} C^{\alpha\beta} b^{\beta} b^{\alpha} \rho^{\alpha} \qquad 4\text{-}18$$

where μ, b^{α}, and $C^{\alpha\beta}$ are the elastic shear modulus on the system, the magnitude of the Burgers vector for the twinning dislocation, and the twin-slip interaction matrix. Slip dislocations can either promote or hinder twin propagation. Positive values of $C^{\alpha\beta}$ indicate when the accumulation of slip dislocation retards and eventually surpasses twin growth, and negative when slip dislocations aid twin dislocation generation

4.2.3 The detwinning model

In the event that the deformation in the grain is reversed, detwinning of the PTS could occur. The detwinning model monitors the possible activation of the PTS inside the twin inclusion (i.e., twinned region), as well as the other twin variants that are not yet represented as reoriented twin inclusions. If another variant other than the PTS is activated, then a secondary twin is created inside the twin inclusion. The detwinning process initiates when the PTS becomes activated inside the twin inclusion. The volume occupied by the PTS is then transferred from the original twin to the matrix. This process is permitted to continue until the entire twin volume has been transferred back to the parent grain, at which point the grain is twin-free and the twin inclusion removed. To

prevent the other twin variants inside the twinned region from being activated once the detwinning process has started, their twin resistance is assigned an exceptionally high value. Last, it is mentioned that the initial detwinning resistance, τ_{prop}^{β}, is made equal to the τ_0^{β} in twinning process. The contribution of the surrounding dislocations on evolution of the detwinning resistance follows the same law as for twinning. The final expression for the detwinning resistance is

$$\tau_c^{\beta} = \tau_{prop}^{\beta} + \mu \sum_{\alpha} C^{\alpha\beta} b^{\beta} b^{\alpha} \rho^{\alpha} \qquad 4\text{-}19$$

4.3 Review of experimental used for validation

Hama et al. performed experiments to investigate the work hardening and twinning behavior in a CP-Ti under large strain cyclic loading (2015). In their experiment, a cold-rolled CP-Ti sheet (Kobe Steel, JIS grade 2) with 1 mm thickness was used. The present study uses data from their experiment in order to understand the contributions of slip and twinning in the deformation of CP-Ti during cyclic loading.

In their work, samples were cut parallel to the RD direction (RD sample) and TD direction (TD sample). All samples were annealed for approximately one hour before testing. The average grain size is 20 μm. Figure 4-4 (a) presents the pole figures of the initial texture of the sample. Monotonic tension, compression, tension followed by compression(T-C) and compression followed by tension (C-T) were performed on the RD and TD samples. A 9 MPa through-thickness stress was applied by comb-shaped dies to prevent buckling

during compression. Mineral hydraulic oil was used to reduce the friction between the die and specimen. The tests were conducted with an initial strain rate of $6.67 \times 10^{-4} s^{-1}$ 1 (see Figure 4-3).

In view of the initial texture in Figure 4-4 (a) of their rolled sheet, it is possible surmise which of the two types of twin modes could be activated during RD and TD cyclic tests. In-plane compression in the RD would generate a local normal tensile stress component along the c-axes in many grains while in-plane tension would generate a local normal compression component. It can, therefore, be expected that in-plane compression would be suitable for activating TTWing and in-plane tension CTWing.

These expectations are consistent with the modeling that has been performed to date. For this same initial texture, Hama et al. (2016) applied a crystal-plasticity finite-element model to study the material response under monotonic loading, either in tension or compression along the RD direction. The initial crystallographic orientations assigned to the elements were randomly selected from a result of EBSD measurement and five families of slip were made available: basal $\{0001\}\langle 11\bar{2}0\rangle$ slip, prismatic $\{10\bar{1}0\}\langle 11\bar{2}0\rangle$ slip, pyramidal $\{10\bar{1}1\}\langle 11\bar{2}0\rangle$ slip, pyramidal $\{11\bar{2}2\}\langle 11\bar{2}3\rangle$ slip, and pyramidal $\{10\bar{1}1\}\langle 11\bar{2}3\rangle$ slip, as well as two families of twinning systems: $\{10\bar{1}2\}$ twinning and $\{11\bar{2}2\}$ twinning. Their modeling results indicated that $\{11\bar{2}2\}$ twinning was activated under RD tension, while $\{10\bar{1}2\}$ twinning was activated under RD compression (Hama et al., 2016).

The properties, particularly in directionality, of these two twin types would suggest that when considering cyclic loading, the order taken in the forward-reverse cyclic loading would lead to different responses. In a forward-reverse load cycle, such as compression-tension, TTWing resulting from the pre-strain compression step would influence the behavior of slip and twinning in the subsequent tension reloading step. Similarly, for the tension-compression cycle, CTWing generated in the pre-loading tension step would affect the slip and twinning activity in the subsequent compression reloading step. However, the underlying slip or twinning mechanisms operating in the cyclic loading would not be so easily apparent in measurements of stress-strain response or EBSD alone. The objective of the modeling effort is to determine the amounts of slip and twinning in each step and whether the mechanisms operating in forward loading alter those in reverse loading.

4.4 Simulation procedure

In the present research study, the polycrystal is represented by a set of grains, wherein each grain is assigned an ellipsoidal shape with distinct crystal orientation and volume fraction. The slip systems and twinning families made available in the simulation are listed in Table 4-1. These five slip and twinning families have been reported in experimental studies of CP-Ti (Chichili et al., 1998; Warwick et al., 2012; Won et al., 2017; Won et al., 2015). They have also been used as input into prior simulation studies on CP-Ti, such as in CPFE (Hama et al., 2016), and VPSC (Wronski et al., 2018) and proven capable of modeling the main deformation characteristics in monotonic deformation (Wronski et al., 2018; Wu et al., 2008). In the calculation, the initial dislocation density is set to

$5.55 \times 10^{10}/m^2$. The latent hardening matrix $L^{ss'}$ components in Eq. 2-2 are 0.5 for interactions between dissimilar slip modes and 1.0 for interactions between slip systems belonging to the same slip mode. The strain rates are set to be the same as the experiment ($6.67 \times 10^{-4}s^{-1}$). The single-crystal elastic constants used for α -Ti were: $\mathrm{C11} = 162.4\ \mathrm{GPa}, \mathrm{C12} = 92\ \mathrm{GPa}, \mathrm{C13} = 69\ \mathrm{GPa}, \mathrm{C33} = 180.7\ \mathrm{GPa}, \text{and } \mathrm{C44} = 46.7\ \mathrm{GPa}$ (Simmons and Wang, 1971).

Table 4-1 Slip and twinning modes used in this work for CP-Ti

Mode	Symbol	Crystallography	No. of systems	B(Å)
Prismatic $\langle \boldsymbol{a} \rangle$	$\alpha = 1$	$\{10\bar{1}0\}\langle 1\bar{2}10\rangle$	3	2.95
Basal $\langle \boldsymbol{a} \rangle$	$\alpha = 2$	$\{0001\}\langle 11\bar{2}0\rangle$	3	2.95
Pyramidal $\langle \boldsymbol{c}+\boldsymbol{a} \rangle$	$\alpha = 3$	$\{10\bar{1}1\}\ \langle 11\bar{2}3\rangle$	12	5.54
Extension twinning	$\beta = 1$	$\{10\bar{1}2\}\langle \bar{1}011\rangle$	6	0.3017
Contraction twinning	$\beta = 2$	$\{11\bar{2}2\}\langle 11\bar{2}\bar{3}\rangle$	6	0.2725

The initial texture measured experimentally in figure 4-4 was used to build the model initial texture used in all simulations to follow presented in this chapter. As a check, figure 4-1 shows the pole figures of the model initial texture, which agrees with the measurement, particularly in the main texture components.

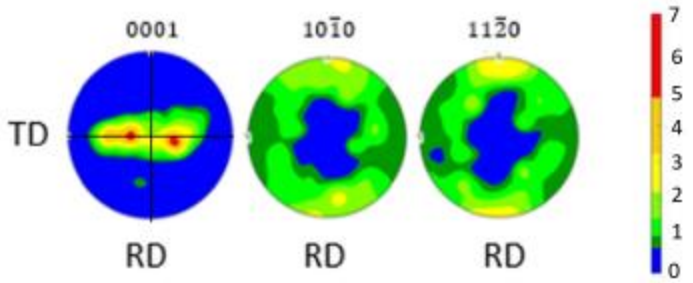

Figure 4-1 Pole figures showing the initial texture of the CP-Ti material used in simulation

Load reversal tension-compression and compression-tension tests were simulated by imposing strain increments along RD or TD, while enforcing zero average stress in the ND and the other lateral sample direction. Using an average stress of 9 MPa in the ND, as in the experiment instead of zero MPa had negligible effect on the results. In simulation, the dislocation density and grain shape and texture were continuously updated.

To characterize the material parameters associated with the hardening law for slip and the model for twinning and detwinning, the simulated forward-reverse stress-strain responses with the experimental responses associated with the 5% cyclic strain tests in the RD and TD directions are compared. The parameter sets for the slip and twin hardening parameters are given in Table 4-2 and Table 4-3, respectively. Requiring that a single set of parameters in the model can reproduce the stress-strain responses in all load reversal tests highly constrains the range of parameters that can be used and, therefore, is a strong indication that these parameter sets are reliable. For validation, the same material parameters were then used to predict the 2%, and 10%-strain load-reversal tests. Finally, the advanced model is used to calculate the deformation textures, twin volume

fraction evolution, and underlying contributions of each slip and twinning mode with strain in all available 2%, 5% and 10% load reversal strain tests.

Table 4-2 Hardening parameters for CP-Ti

	Prismatic ($\alpha = 1$)	Basal ($\alpha = 2$)	Pyramidal ($\alpha = 3$)
$\tau_0^\alpha(MPa)$	69	128	180
$k_1^\alpha(m^{-1})$	1.02×10^8	1.07×10^8	0.95×10^8
g^α	0.01	0.015	0.09
$D^\alpha(MPa)$	500	800	800
$HP^{\beta 1}$	0.1	0.1	0.1

	$\tau_0^\beta(MPa)$	$C^{1\beta}$	$C^{2\beta}$	$C^{3\beta}$
Extension Twin ($\beta = 1$)	230	20000	8600	11200
Contraction Twin ($\beta = 2$)	260	8200	8200	8000

Table 4-3 Kinematic hardening parameters for CP-Ti

	$\tau_{bs}^{sat}(MPa)$	ν	γ_b	A
Prismatic (α = 1)	11	40	0.001	1
Basal ($\alpha = 2$)	15	60	0.006	1
Pyramidal ($\alpha = 3$)	15	50	0.09	5

4.5 Results

4.5.1 Stress-strain response

The model is first used to understand the slip, twinning, and slip-twin interactions that underlie the measured cyclic loading responses. Figure 4-2 and Figure 4-3 compare the calculated curves with the measured ones for all the 5% forward-reverse loading tests. As shown, the model replicates well the forward and reload deformation responses, including the lower yield stress on reverse straining than in pretraining and hardening rate.

A few aspects of the deformation response are worth noting. The material exhibits a small amount of tension-compression asymmetry in yield and strain hardening. In the RD, for instance, the yield stress and flow stress at 5% in monotonic compression are 202 MPa and 406.5 MPa, whereas they are 198 MPa and 422.3 MPa in monotonic tension. The response also exhibits a Bauschinger effect, wherein the yield stress in the tension reload is 161 MPa, compared to the 202 MPa in the compression pre-straining step. The responses are generally higher in the TD-load tests compared to the RD-load tests. For instance, after 5% compression loading in the TD, the yield and flow stress are 221 MPa and 429 MPa. Notably, these features are also represented in the calculated stress-strain responses.

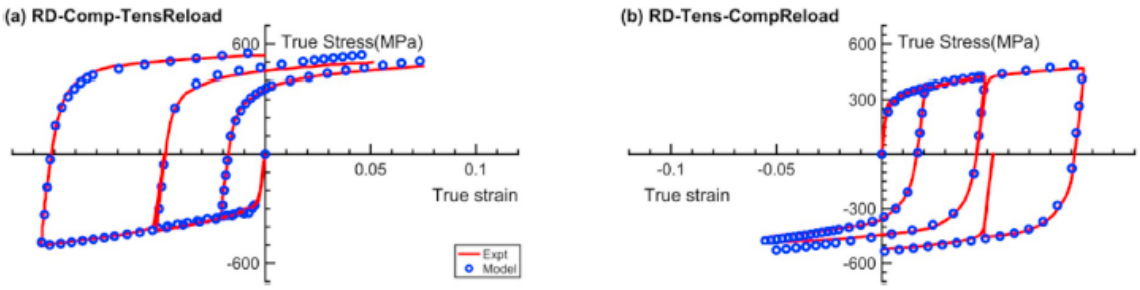

Figure 4-2 Comparison of the measured and calculated true stress-true strain response of CP-Ti when deformed in the RD direction (a) Compression followed by a tension reload (CT), (b) and tension followed by a compression reload (TC). Experimental data are taken from (Hama et al., 2015)

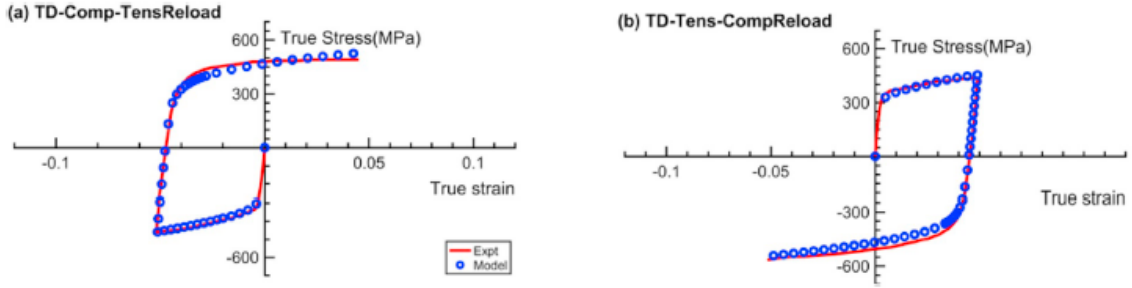

Figure 4-3 Comparison of the measured and calculated true stress-true strain response of CP-Ti when deformed in the TD direction (a) CT, (b) TC. Experimental data are taken from (Hama et al., 2015)

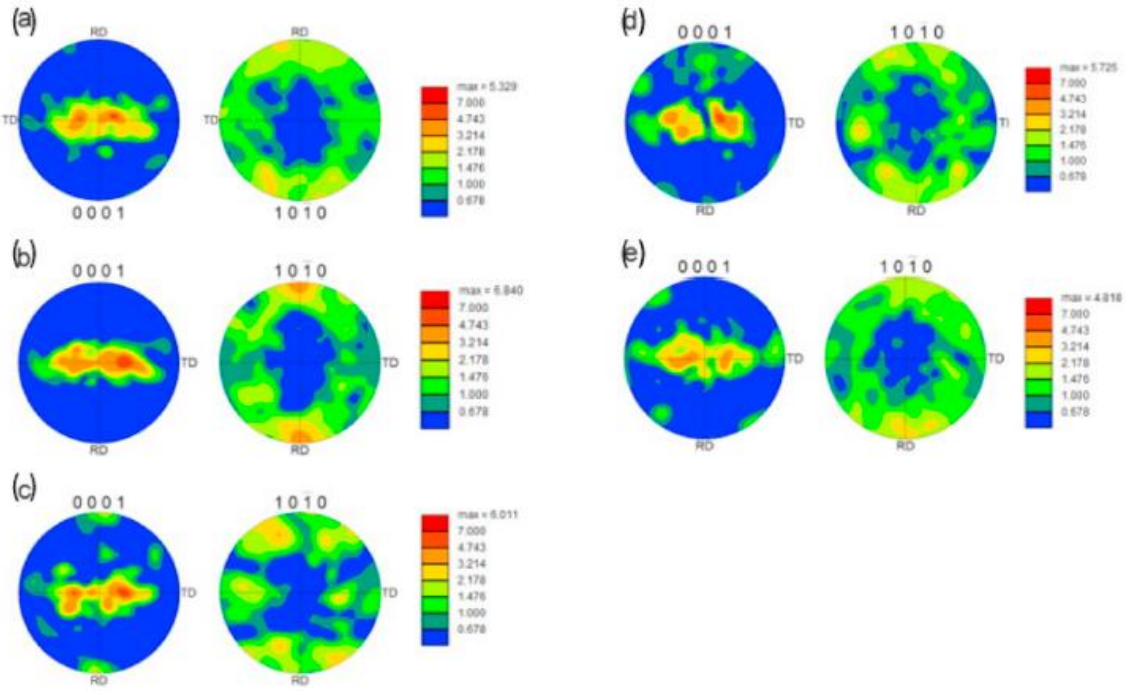

Figure 4-4 Experimental results taken from Hama et al. (2015) showing the {0001} pole figures for the (a) initial texture and (b–e) samples deformed in the RD direction: (b) texture at 0.1 strain during the tension in TC loading (c) texture at - 0.1 strain during compression in CT loading, (d) and (e) textures at -0.05 and 0 strain, respectively, during reverse loading in CT loading. This image is adapted with permission from Hama et al. (2015)

4.5.2 Slip model strengths and dislocation density rate parameters

The material parameter set associated with these calculations can provide some insight into individual slip strengths and their tendencies for strain hardening. Table 4-2 and Table 4-3 present the material parameters corresponding to the rate laws for dislocation density evolution and twinning, and kinematic hardening. Although they were able to simultaneously match all load-reload tests in figure 4-2 well, it is recognized that they may

not be unique. For this reason, these parameters with similar material parameters reported in the literature are compared and validation calculations are performed.

The initial slip resistance τ_0, given in table 4-2, governs the initial yield stress and is a common parameter in most hardening models. In the present case, prismatic $\langle \boldsymbol{a} \rangle$ slip has the lowest initial slip resistance, basal $\langle \boldsymbol{a} \rangle$ slip has the next higher one, and pyramidal $\langle \boldsymbol{c} + \boldsymbol{a} \rangle$ slip the highest. The values are in good agreement with CRSS measurements made by in-situ high energy X-ray diffraction microscopy (HEDM) experiment, which reported $96 \pm 18\ MPa$ for prismatic $\langle \boldsymbol{a} \rangle$ slip and 127 ± 33 MPa for basal $\langle \boldsymbol{a} \rangle$ slip (Wang et al., 2017). Also, in agreement, pyramidal $\langle \boldsymbol{c} + \boldsymbol{a} \rangle$ slip was reported to have the highest CRSS; however, it was indirectly assessed to be larger than 240 MPa, which is larger than that found here. The ranking of these modes is also consistent with slip strengths from many other studies, which involved experimental data and modeling approaches different from this (see recent review in as well as those from recent modeling work on CP-Ti by (Wronski et al., 2018) which used the same dislocation density-based law used here, but within the visco-plastic self-consistent (VPSC) model and for modeling monotonic stress-strain response data.) Also, it is noted that among the three slip modes, the prismatic slip mode has the lowest trapping coefficient, drag stress, and activation enthalpy for dislocation processes aiding dynamic recovery. It would be expected that prismatic slip would continue to dominate plasticity in CP-Ti.

Table 4-3 reports the material parameters associated with the resistance to twin expansion (as opposed to nucleation). The resulting values for τ_0 for twinning suggest that both contraction and extension twinning are more difficult to propagate compared

to slip, with contraction twinning being the slightly harder one of the two modes. The relative ease of $\{10\bar{1}2\}$ extension twinning compared to $\{10\bar{1}1\}$ contraction twinning is consistent with experimental assessments by (Tirry et al., 2012). It is also observed from table 4-3 that the interaction matrix $C^{\alpha\beta}$ components are relatively large, indicating a strong repulsive interaction between these two twin types and all types of dislocations.

For validation, the model is applied to additional load reversal tests involving either lower (2%) strains or higher (10%) strains (Hama et al., 2015) without further adjustments to the parameters in table 4-2 and table 4-3 The comparison between the simulated and measured responses given in figure 4-2 show that the model achieves reasonable agreement.

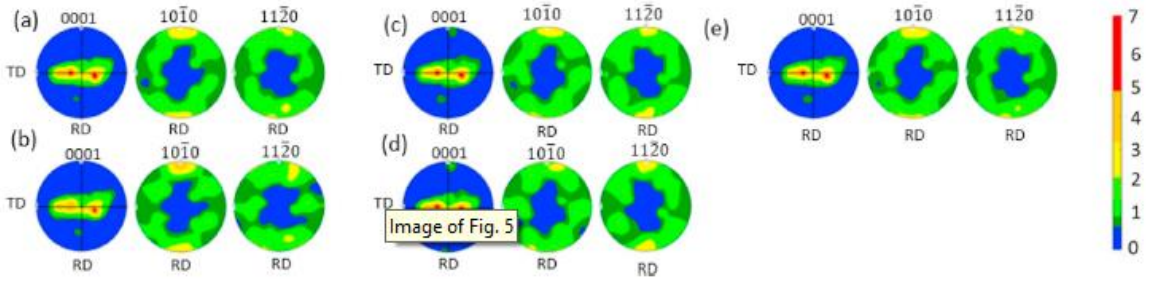

Figure 4-5 Calculated textures presented as {0001} pole figures for the (a) initial texture and (b–e) deformed RD samples: (b) texture at 0.1 strain during the tension in TC loading (c) texture at - 0.1 strain during compression in CT loading, (d) and (e) textures at - 0.05 and 0 strain, respectively during reverse loading in CT loading.

4.5.3 Slip activity and deformation twinning

Another important output of the modeling effort is the active slip and twin modes underlying each cyclic test and their individual contributions to the overall polycrystalline

deformation. Experimental assessment of which slip, and twinning systems are active during deformation can be challenging. Common approaches involving metallography are post-mortem methods and they indicate the types of dislocations that are stored (Han et al., 2012; Kumar et al., 2017a; Lentz et al., 2014; Zheng et al., 2014). In-situ approaches utilizing diffraction involve a model to de-convolute or decouple the relative amounts contributed by the active slip and twinning systems (Lentz et al., 2015a; Risse et al., 2017; Zhang et al., 2019a). In this section, the model is used to provide some insight into the strain evolution of slip activity and twin volume fraction during these load reversal tests.

The calculated strain evolution of the relative slip activities (RA^{α}) of basal slip, prismatic slip, and pyramidal $\langle \boldsymbol{c}+\boldsymbol{a} \rangle$ slip for the bulk polycrystal during the 5% strain cycle are presented in Figure 4-6. Relative slip activity is defined as:

$$RA^{\alpha} = \frac{\sum_n W_n \sum_s d\gamma^s_{\alpha,n}}{\sum_n W_n \sum_\alpha \sum_s d\,\gamma^\alpha_{\alpha,n}}$$

where W_n is weight percentage of grain *n* and the calculation for slip activity spans all grains *n* in the polycrystal. Further, the sum $\sum_s$ is taken over all slip systems belonging to the α family and the sum $\sum_\alpha$ corresponds to the strain contributed by all modes of slip and twinning in a grain *n*. The slip activity plots begin where plasticity initiates in a given strain path. Between strain paths when the material is first reloaded, a short transient period is seen, wherein in slip activity rapidly changes due to a combination of backstresses evolution, evolution of the elastic contribution, and initial easy glide on the easiest slip system, prismatic slip.

From the results in Figure 4-6, it is first noticed that in RD and TD deformation, whether initially in compression or tension, that prismatic slip is the most active throughout deformation. Secondly, although prismatic slip is the dominant mechanism, the other two slip modes contribute, albeit in varying amounts. The initial texture is not uniformly random, yet it is not exceptionally strong. The basal poles of the grains are distributed within a range of $60°$ about the normal direction in the TD direction. It can, therefore, be anticipated that under an in-plane uniaxial stress state, many grains would be suitably oriented for both $\langle \boldsymbol{a} \rangle$ slip and $\langle \boldsymbol{c} + \boldsymbol{a} \rangle$ slip. Thirdly, there is little tension-compression asymmetry in slip activity, provided that the loading direction is preserved. Figure 4-6 shows that in either RD or TD loading, the relative activities of the three slip modes in tension and compression are the same. Last, the results indicate that slip activity during deformation is unaffected by pre-straining. Whether the load is directed in the RD or TD, the slip activity in the compression reload after tension pre-strain is similar to the slip activity in compression without the pre-straining.

Compared to the sense of loading or the order of the cyclic loading (CT vs. TC), the loading direction, whether in RD or TD, has the greatest effect on the type and amounts of slip activated. This particular plastic anisotropy is to be expected due to the fact that the material, as mentioned, not only has a preferred initial texture but it also does not exhibit symmetry in the plane of the sheet (e.g., it is not axisymmetric about the ND). Loading along the RD direction has more grains more suitably oriented for pyramidal $\langle \boldsymbol{c} + \boldsymbol{a} \rangle$ slip than basal $\langle \boldsymbol{a} \rangle$ slip compared to loading along the TD, which activates more basal $\langle \boldsymbol{a} \rangle$ slip than pyramidal $\langle \boldsymbol{c} + \boldsymbol{a} \rangle$ slip.

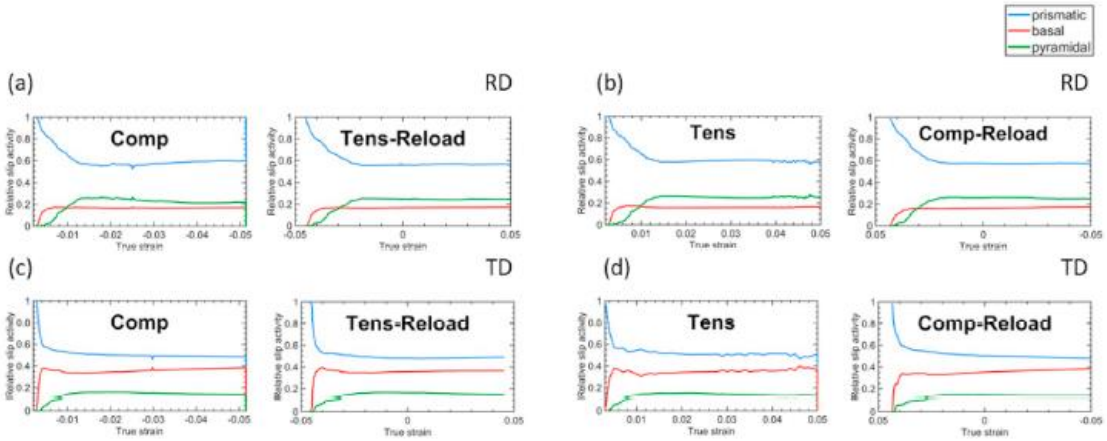

Figure 4-6 Calculated slip activities during 5% cyclic loading: (a)RD-CT; (b)RD-TC; (c)TD-CT; (d)TD-TC

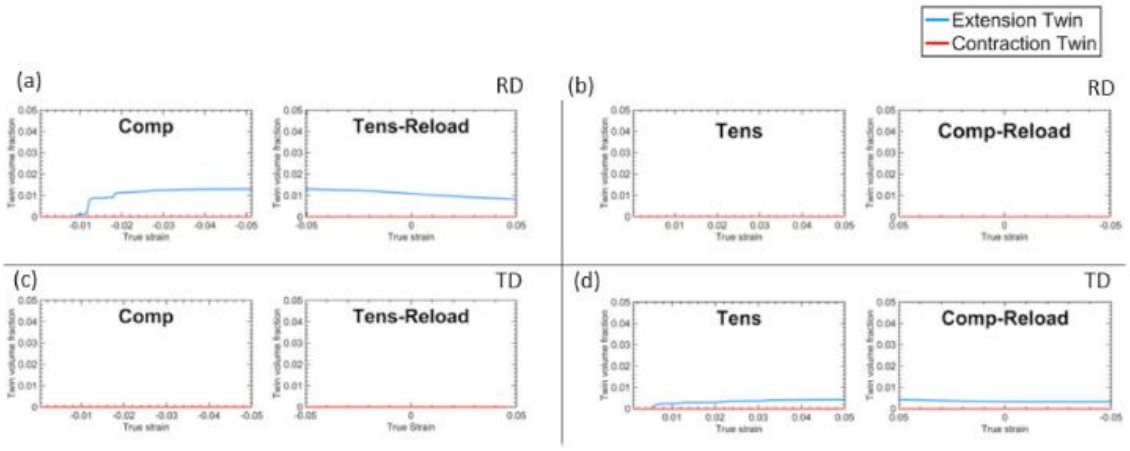

Figure 4-7 Calculated twin volume fraction evolution during 5% cyclic loading in (a–b) RD and (c–d) TD directions: (a)RD-CT; (b)RD-TC; (c)TD-CT; (d) TD-TC.

Deformation twinning, unlike slip, is a unidirectional deformation mechanism, and compared to slip, can be much more sensitive to crystallographic orientation and sense of loading (whether in compression or tension). Figure 4-7 (a and b) examines the strain evolution of the bulk polycrystal twin volume fraction calculated by the model during the

5% strain cyclic tests in the RD direction. The first test analyzed of the results applies compression in the RD and reloads in tension in the RD, and the second one examined takes the opposite path, with tension applied in the RD followed by compression in the RD. Initially, the c-axes of most grains in the sample are closely aligned along the ND, so compression in RD favors TTWing, whereas tension in RD favors CTWing. These two tests, therefore, enable study of the effects of the reloading path on either TTWing or CTWing generated in the preloading step.

The RD-CT cyclic test, RD compression followed by a tension reload is first considered. From the model calculations, in RD compression, TTWing is activated and increases to 3.5% twin volume fraction for the entire polycrystal by 5% compression strain. Upon unloading and reloading in tension, detwinning of the TTWs occurs. After 5% tension reloading, the TTW volume fraction is still 2.5%. No new TTWs occur in tension reloading, so the 2.5% TTW fraction at the end of the test are retained from pre-straining. In agreement, Hama et al. (2015) and Ma et al. (2019) reported $\{10\bar{1}2\}$ twinning during RD compression and $\{10\bar{1}2\}$detwinning in the tension reload following compression. During this test, CTW also occurs but in relatively small amounts. CTWing is activated while unloading and reloading, reaching a total of 0.5% twin volume fraction after 5% tension reloading.

The model calculations for the RD-TC load reversal test, RD tension followed by a compression reload, find that twinning is not prevalent. At the end of 5% RD tension step, the calculated CTW volume fraction is 0.6% (Figure 4-7). Upon unloading and reloading in RD compression, the CTW volume fraction decreases. CTW-detwinning is slow and incomplete, leaving some CTWs at the end of the test. After 10% RD tension, the

calculated CTW volume fraction is higher at 1.5% (see Figure 4-8 (c)). TTWing did not occur in either RD tension pre-loading or RD compression reloading. In agreement, corresponding experiments (Hama et al., 2015; Ma et al., 2019) also reported that $\{10\bar{1}2\}$ twinning was more active during RD compression than during RD tension.

Figure 4-4 presents the texture measurements reported previously in Hama et al. (2015), wherein they used only $\langle 0001 \rangle$ and $\langle 10\bar{1}0 \rangle$ pole figures. The texture in figure 4-4 (b) for RD tension after 10% strain presents little change in the basal pole figure from the initial texture. The prismatic poles have aligned along the RD, the tensile loading direction. This evolution would be expected of slip dominated deformation. Consistent with this assessment, the model predictions for this case indicate that monotonic RD tension is accommodated predominantly by prismatic slip and little CTWing (1.5% twin volume fraction, see Figure 4-7). The calculated texture for this case agrees with the experimental measurement (see Figure 4-5).

Texture measurements were also made in RD-compression testing. The measured textures in Figure 4-4 (d) after 5% compression straining and in Figure 4-4 (c) after 10% present evidence some TTWing. The basal pole figure displays a weak basal pole texture component aligned with the RD that is not found in the initial texture. This change is a common signature of TTWing, which can reorient the basal pole $85 - 86°$ toward the loading axis. The fact that it is weak is consistent with the prediction that the TTW volume fraction after 5% is 3.5% and after 10% is 4.1%. The measured texture in figure 4-4 (e) at zero net strain, achieved during the tension reload step, shows that this "twinning signature" has disappeared, implying detwinning. In agreement the calculated texture in

Figure 4-5 also predicts disappearance of this component. Further, for this same zero net strain the calculated TTW volume fraction has reduced to 3% as a result of detwinning.

Figure 4-7 (c and d) shows the strain evolution of extension and compression twin volume fraction in the two cyclic tests applied along the TD direction of the sheet. Unlike in RD loading, in TD loading, deformation twinning is negligible, highlighting the strong anisotropy caused by the initial texture. In TD-CT loading, twinning is not activated, and in TD-TC loading, small amounts of extension twins (<1% volume fraction) are produced during the forward tension path. After 0.04% strain, contraction twinning initiates and grows to negligible amounts (<< 1% volume fraction). During the compression reload, these twins are largely preserved, with no further propagation and negligible occurrences of detwinning. To conclude, in TD, deformation is largely slip dominated, indicating that any hysteresis seen in the cyclic stress-strain response is due to the development of backstresses. This finding is in good agreement with the conclusion in Hama et al. (2015) and Ma et al. (2019) that the activity of twinning is much smaller in TD than in RD (2015).

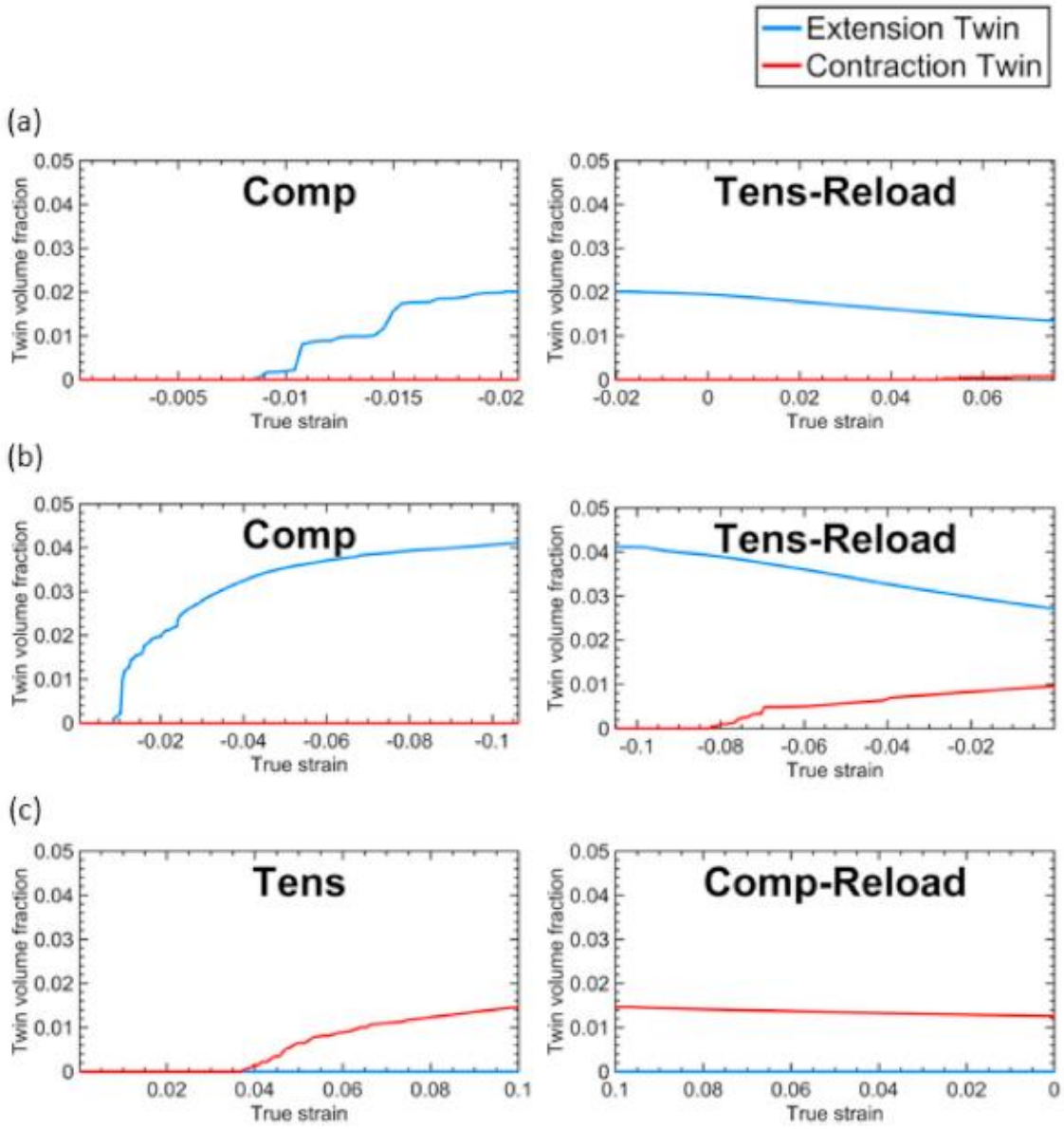

Figure 4-8 Calculated twin volume fraction evolution during cyclic loading:(a)2% RD-CT, (b)10% RD-CT and (c)10% RD-TC.

4.6 Discussion

4.6.1 Effect of backstress development

To analyze backstress development, the backstress of each slip system in each grain during deformation is calculated. Figure 4-9 presents the backstress (type III stress) averaged over the entire polycrystal. While backstresses may develop in all slip systems, only the top two slip systems generating the most backstress in each test are shown. Overall, their value is small relative to the flow stress, which is expected for intra-granular stresses (type III stress). In figure 4-9, it is observed that the backstress evolves abruptly with small changes in strain. Its value increases with strain, remains constant with unloading, and drops in reloading. The model indicates that in the four tests studied here, the backstress develops predominantly on a few pyramidal slip systems, experiencing the largest slip activity. For instance, in the CT test in the RD direction, the top two systems are the $(1\bar{1}01)[\bar{2}113]$ and $(\bar{1}011)[2\bar{1}\bar{1}3]$ pyramidal slip systems, while for the TD-TC test they are $(0\bar{1}11)[\bar{1}2\bar{1}3]$ and $(\bar{1}011)[11\bar{2}3]$ pyramidal slip systems. The amount of backstress on these systems loosely correlates with the amount of pyramidal slip activity in the test. The RD-TC test generates the most backstress among the four tests, wherein pyramidal slip was the second most active slip system, compared to prismatic slip, and among the four tests, pyramidal slip was the most active.

The active slip and twinning systems in each grain are determined by a combination of the backstress and local stress resulting from the applied strain. Further, it is noted that the backstresses are relatively small (<4 MPa) compared to the macroscopic stress. In an attempt to elucidate the individual role played by the backstress, the calculations without

the backstress model are repeated and the resulting slip and twinning activity studied. The first step is to re-characterize a few material parameters in the dislocation density law to ensure that the model without backstress develop can still replicate the forward stress-strain response. Toward this end, only k_1^α and g^α for the prismatic slip mode needed to be changed to 1.22×10^8 and 0.025, respectively. Figure 4-10 and figure 4-11 show the slip activity and twin volume fraction evolution in the load reversal test without backstress development included. Compared to the case without backstress, it is found that TTW development has reduced during the initial compression deformation and CTW has been suppressed entirely. Pyramidal slip, TTW and CTW are all modes that accommodate $\langle \boldsymbol{c} \rangle$ axis deformation in the grains. This analysis indicates that backstress, which develops preferentially on the pyramidal slip systems, hinders pyramidal slip, therefore encouraging the formation of twins.

4.6.2 Effect of preloading

The model analysis indicates that, at the polycrystal scale, the amounts of each slip mode that contribute to the deformation are not significantly affected by the sense of direction—tension or compression—or by the 5% pre-straining. Comparatively, however, the strain path change is seen to noticeably affect deformation twinning. In the 5% deformation cycle, TTWing was activated in RD compression at 5% deformation with no prestraining but it was not activated during RD compression after 5% deformation following RD-tension prestraining step to 5% deformation. Similarly, CTWing was activated in RD tension after 5% straining with no pre-straining step but not when RD tension was applied after a RD compression pre-straining step. This suggests that marked

differences in twinning activity between monotonic loading and cyclic loading can be expected even in HCP materials that twin easily.

Much of the analysis, thus far, has focused on load reversal tests to 2% and 5%. Next the model is applied to predict the effect of the pre-straining primary path on the reversal compression or tension response in the RD direction, by comparing the response up to 10% strain without and with 5% prestraining and analyzing the changes in slip and twinning activity. Ffigure 4-12 (a) compares the RD tensile response starting from the initial texture and twin-free microstructure with the RD tensile response after 5% compression pre-straining. The results show that the tensile response has been altered by the pre-straining. Compared to the response without the compression preload, the yield stress has been reduced and the work-hardening rate increased. The model indicates that this change is not a result of a change in slip activity. As shown in figure 4-6 the slip activity in the compression reload deformation is predominated by prismatic slip and accompanied by a lower, although a substantial, contribution of pyramidal slip and basal slip. At the polycrystal level, the amounts of strain contributed by these three slip modes is similar in RD tension without and with the pre-straining (see Figure 4-13). However, the twinning activity has changed. In the cyclic test case, the compression pre-strain introduces TTWs, calculated to be 3.5% volume fraction (see Figure 4-7 (a)). When tension is subsequently applied, the material already contains TTWs, which proceed to detwin during the course of tensile loading, and forms CTWs, which achieve about 1% CTW volume fraction after 10% tensile strain. In comparison, tensile loading from a twin-free structure develops 1.6% volume fraction after 10% tensile strain (see Figure 4-14).

Thus, the effect of pre-straining is to reduce the amount of twinning. Pre-straining creates a backstress on pyramidal slip, which can favor its activation when the strain is subsequently reversed.

Likewise, the effect of twin-slip interactions can be assessed when comparing the RD compression responses. In the RD direction, Figure 4-12 (b) compares the compression "monotonic" response, initially with a twin-free microstructure, and the compression reload response after 5% tension pre-straining. As in the other test, the compression response has been altered by the pre-straining, with a lower yield stress and higher work-hardening rate, than the compression response without the prestraining. Similarly, the change cannot be attributed to profound changes in slip activity. Both RD compression responses are accommodated by prismatic slip and secondly pyramidal and basal slip (see Figure 4-6). The twinning behavior, however, has experienced a noticeable change, as shown by comparing figure 4-7 and figure 4-14. After the tensile 5% pre-strain, the material develops 0.6% volume fraction of CTWs. During the subsequent compression reload path, the CTWs do not detwin but are maintained and more significantly, no TTWing occurs. This response is in stark contrast, during the compression response without pre-straining, which develops 4.4% volume fraction of TTW after 10% straining. Again, the pyramidal slip backstress that develops in pre-straining favors pyramidal slip in the following reverse straining, making TTW less competitive.

In figure 4-13, the dislocation activities and twin volume fraction for monotonic loading are plotted. It can be observed that the dislocation activity for prismatic and basal are very similar in different loading path. But during monotonic loading, pyramidal slip is

activated. During CT loading process, detwinning are activated. It is speculated the twinning and detwinning mechanism may compete with the pyramidal slip. The pyramidal slip has a much higher critical shear stress than basal slip and prismatic slip. Thus, it is reasonable to think the activation of pyramidal will not the major factor of lower macroscopic stress in monotonic loading simulation. Then it is inferred that the high twin volume fraction is an explanation of the difference between MT loading and CT loading. This adheres to the former conjecture that the formation of twin result in an increase in macroscopic stress.

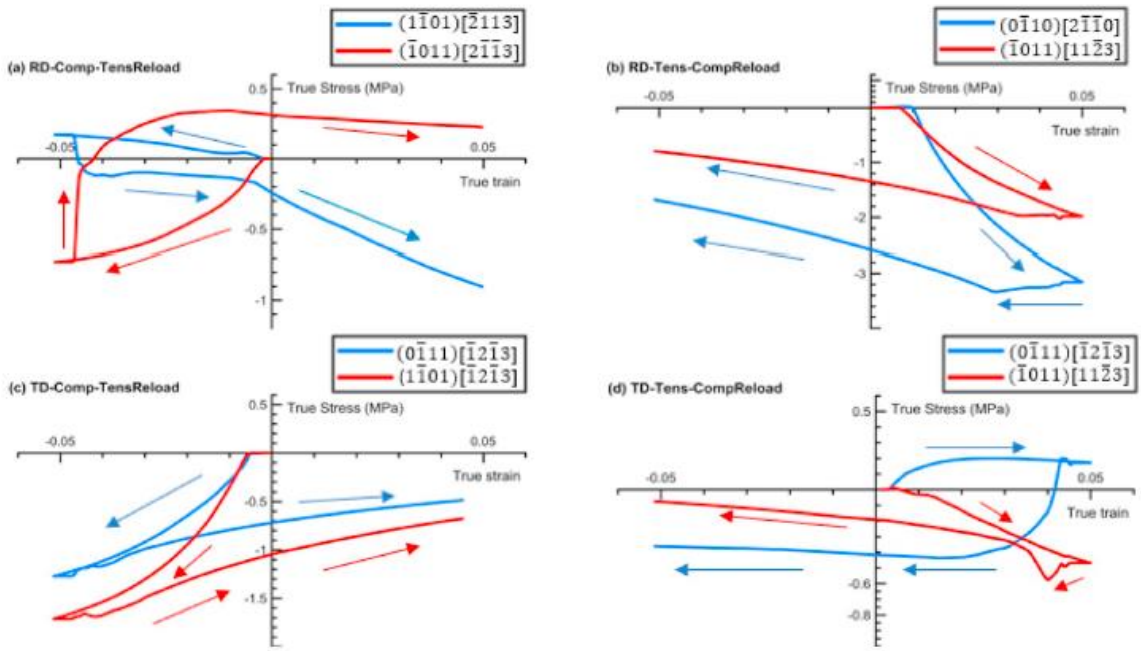

Figure 4-9 Calculated backstress evolution in the two slip systems developing the highest backstress values in each cyclic test

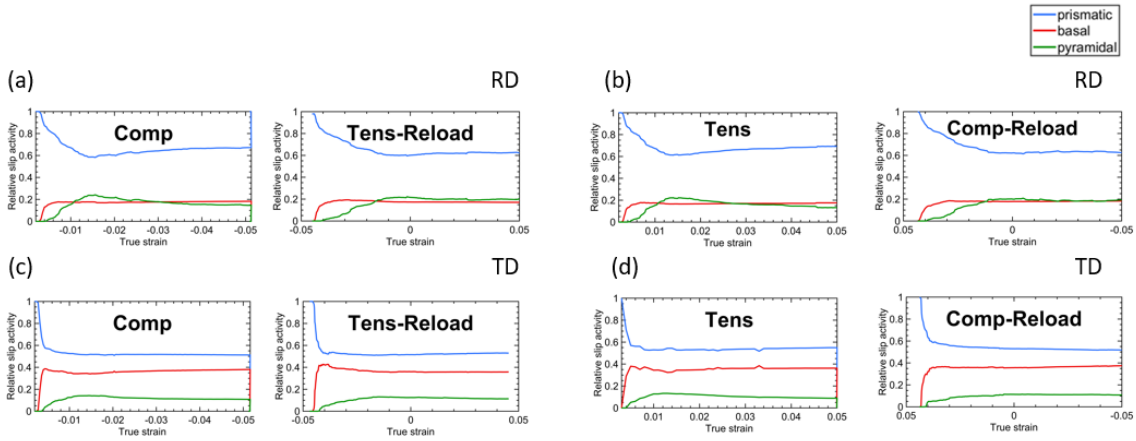

Figure 4-10 Calculated slip activities of the mode without taking into account backstress development during 5% cyclic loading in RD and TD directions: (a)RD-CT; (b)RD-TC; (c)TD-CT; (d)TD-TC.

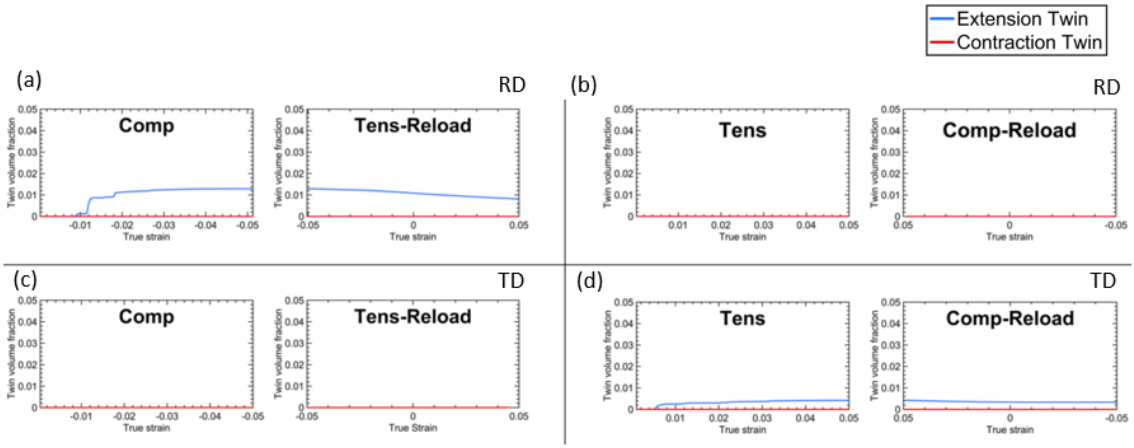

Figure 4-11 Calculated twin volume fraction of the mode without taking into account backstress development during the 5% cyclic loading test in RD and TD directions: (a)RD-CT; (b)RD-TC; (c)TD-CT; (d)TD-TC.

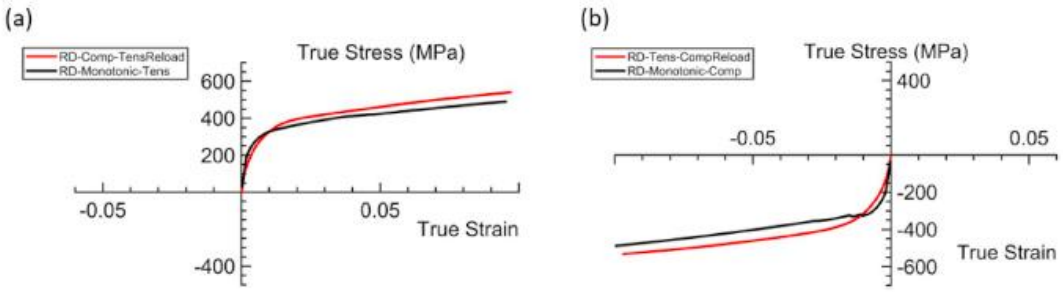

Figure 4-12 (a) Comparison between monotonic tension in the RD direction and with the tension response following 5% compression in the RD direction and (b) Comparison between monotonic compression in the RD direction and with the compression response following 5% tension in the RD direction.

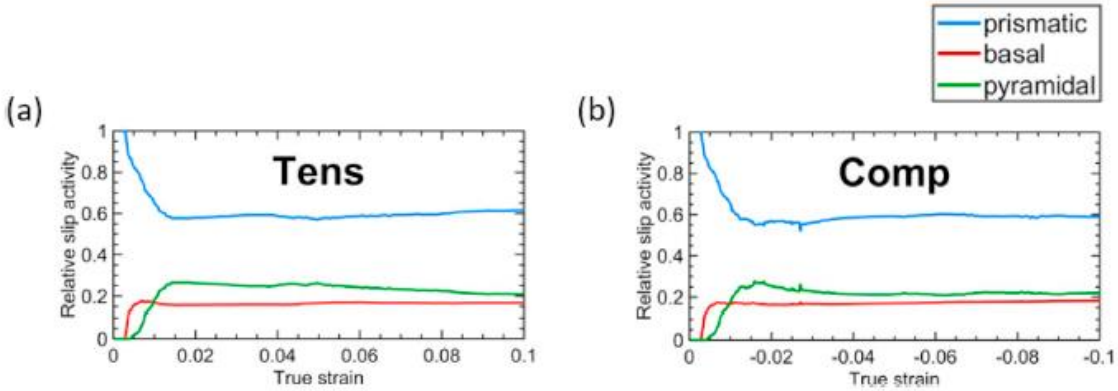

Figure 4-13 Calculated slip activities during (a) monotonic tension and (b) monotonic compression in the RD direction.

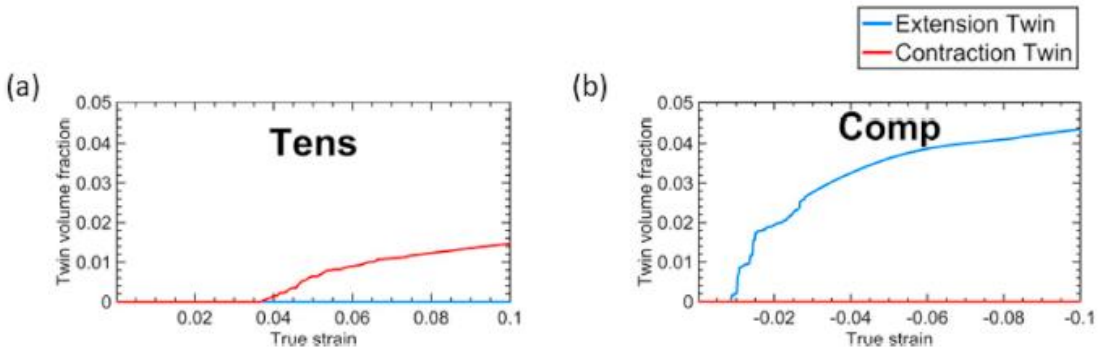

Figure 4-14 Calculated twin volume fraction evolution with straining in (a) monotonic tension and (b) monotonic compression in the RD direction.

4.7 Conclusions

In this study, an elasto-plastic self-consistent (EPSC) polycrystal plasticity model is used to study the deformation behavior in commercially pure titanium under load reversals. The model takes into account several subgrain mechanisms, anisotropic elasticity, crystal plasticity by $\{10\bar{1}0\}$ prismatic slip, $\{0001\}$ basal slip and $\{10\bar{1}1\}$ pyramidal slip, dislocation density-based hardening of slip strengths, deformation twinning by both contraction and extension twinning, reorientation by twinning and detwinning, and slip-system-level backstress development. With a single set of material parameters, the model achieves good agreement with a broad range of tests: true stress-strain responses in both compression-tension and tension-compression type cycles, to different strain levels, 2%, 5%, and 10%, and repeated in two different directions, the rolling and transverse directions. The texture evolution predicted by the model agrees well with available measurements. With the model, the slip activities, twin activities and backstress evolution during the deformation are further investigated. While prismatic slip was dominant in all

strain paths, the deformation was accommodated by multiple slip systems, wherein the relative amounts of basal slip and pyramidal slip were non-negligible. It is found that the relative amounts of slip contributing to polycrystal level deformation did not substantially change with cyclic loading or sense of loading, provided the loading direction was the same. The analysis indicates that type III, intra-granular backstresses develop more strongly in $\langle \boldsymbol{a}+\boldsymbol{c} \rangle$ pyramidal slip than the other two $\langle \boldsymbol{a} \rangle$ type slip modes. As a result, pyramidal slip backstresses that develop in forward loading make deformation twinning by both extension and contraction modes more favorable. In reverse loading, pyramidal slip is favored over twinning due to the reversion of the sign of the backstresses. Consequently, the material develops more twins when strained from an undeformed state than when strained after pre-straining in the opposing direction.

5 Role of Yttrium concentration in the deformation of Mg-Y alloys

5.1 Motivation

Mg alloys have been the focus of intense research in recent years due to their potential for light weighting structural components. The challenge, however, is that Mg and its alloys display limited room temperature ductility, hindering their widespread application. Mg-Y alloys show improved ductility compared with the pure Mg which make deformation in elasticity become less important. In alignment with the second objective for this thesis research, which is to determine how twinning affects dislocation

behavior, the effect of Y in Mg-Y alloys on twinning is studied. Recall that multiple twinning modes can be activated in HCP metals under deformation depending on the loading direction and texture. In Mg, the most common twin is $\{10\bar{1}2\}$ tensile twin, and other types of twin are relative less active. Likewise in the Mg-Y alloys considered in this study, experimental observations have shown that the $\{10\bar{1}2\}$ twin type is also the dominate one. Therefore, the focus of this computational investigation on Mg-Y alloys lies in the interaction between dislocations and the $\{10\bar{1}2\}$ tensile twin mode. To obtain a more comprehensive understanding, Mg-Y alloys with different concentrations were investigated. Since large strain behavior is of interest, the VPSC model is used instead of the EPSC model, which more efficiently treats microstructural evolution in this regime. Before presenting the research, first a general review of VPSC model and additional hardening model is provided.

5.2 VPSC Background

In this chapter, the VPSC model was employed to relate the macroscopic deformation response with texture evolution and the underlying slip and twinning mechanisms. A detailed description of the VPSC model originally developed by Lebensohn and Tomé can be found in (Lebensohn and Tomé, 1993; Tomé and Kaschner, 2005). The hardening law used in VPSC is extended to account for the interaction between dislocation storage and twin growth. In this section, the VPSC polycrystal model with the model for slip/twin

interactions is described. The flow rule of VPSC, which relates the local stress, $\boldsymbol{\sigma}$, to strain rate, $\dot{\varepsilon_{ij}}$, is expressed in the form of a power-law function via:

$$\dot{\varepsilon_{ij}} = \sum_s m_{ij}^s \dot{\gamma}^s = \dot{\gamma}_0 \sum_s \left| \frac{m^s : \boldsymbol{\sigma}}{\tau_c^s(\dot{\varepsilon}, T)} \right|^n \text{sign}(m^s : \sigma) \qquad 5\text{-}1$$

The flow rule introduces a critical strength or slip resistance τ_c^s that depends on the local microstructure and structural obstacles encountered by the dislocations. In Eq. 5-1, $\dot{\gamma}^s$ and m^s are, respectively, the shear rate and the symmetric Schmid tensor for system *s*, $\dot{\gamma}_0$ is the reference shear strain rate, and σ is the stress tensor. The exponent *n* has been referred to as the inverse slip rate sensitivity, yet here it is elected to use a sufficiently high value for *n* (i.e., *n* = 20), so that rate sensitivity in the activation of slip ($\dot{\gamma} > 0$) is controlled by the rate sensitivity in τ_c^s.

5.2.1 Twin affected dislocation storage rates

In some test orientations, the stress strain response of Mg alloys can exhibit inflections in the hardening rate, which are known as twinning signatures, signifying that twinning is occurring in addition to slip. Interactions between dislocations and growing twins have been considered to contribute to such distinctive changes in hardening. Several possible dislocation/twin interaction scenarios have been discussed in chapter 2. In recent work, Chen et al. (2019), using molecular dynamics simulation, studied the interaction between an impinging dislocation and an extension twin boundary in pure Mg. They found when the Burgers vector of a dislocation (basal, prismatic and $\{10\bar{1}1\}$ $\langle \boldsymbol{c} + \boldsymbol{a} \rangle$ pyramidal dislocations) is not parallel to the zone axis of the twin, the twin boundary can act as a dislocation sink, in which the matrix dislocation is absorbed by the twin boundary(Chen

et al., 2019). This scenario suggests that dislocations can be consumed by the migrating twin boundary, leading to a reduction in the dislocation trapping rate. This reduction is different than the reduction in dislocation density due to dynamic recovery, which is a thermally activated mechanism enabled by dislocation-dislocation reactions. Here, the DD model is extended to account for the reduction in the trapping rate caused by twin growth. To reflect this interaction, the trapping rate coefficient k_1^α in Eq. 2-3 for a given dislocation slip α in a given grain is made to depend on the growth rate of the twin, $\frac{\partial f}{\partial t} = \frac{\dot{\gamma}}{s}$ in the same grain. When there is no twinning, the coefficient k_1^α in Eq. 2-3 is constant and controls the rate of dislocation trapping with respect to shear. Yet, when twins have already formed and are growing, the coefficient decreases concomitantly, resulting in a decrease in the trapping rate. To capture this effect, the following exponential decay law is adopted

$$k_1^\alpha = k_0^\alpha \exp\left(-C \sum_t \frac{\partial f^t}{\partial t}\right) \qquad 5\text{-}2$$

where $\frac{\partial f}{\partial t} = \frac{\dot{\gamma}}{s}$ is the twin growth rate in the CG model, $C = \frac{\dot{\gamma}_0}{s}$, where $\dot{\gamma}_0$ is a reference shear rate defined in Eq. 5-1, and k_0^α is the initial trapping rate coefficient in the twin-free grain.

5.3 Experimental Procedures

The simulation studies in this thesis work were motivated by experimental testing and characterization performed elsewhere. To be complete, in this section, the experimental procedures are reviewed.

5.3.1 Material Preparation

The four Mg-Y alloys used in this study (Mg-0.2Y, Mg-0.6Y, Mg-1Y and Mg-3Y) were prepared at Helmholtz-Zentrum Geestchacht in Geesthacht, Germany. The chemical composition of the alloys was controlled by spark emission spectrometry and are the same as those used in prior studies (Hantzsche et al., 2010; Sandlöbes et al., 2011). The cast ingots were homogenization heat-treated and hot-rolled at 500 °C to a final thickness of 6 mm. To achieve a similar grain size of approximately 20-25 µm in all four Mg-Y alloys, selected recrystallization heat treatment procedures were carried out. These recrystallization parameters for the four samples are listed in Table 5-1.

Table 5-1 Nominal compositions, recrystallization heat treatment conditions and average grain size of Mg-Y alloys.

Sample	Mg-0.2Y	Mg-0.6Y	Mg-1Y	Mg-3Y
Solute concentration	0.2 wt%	0.6 wt%	1 wt%	3 wt%
Recrystallization temperature and time	400°C, 5 min	400°C, 10 min	400°C, 10 min	450°C, 10 min
Average grain size	35 µm	21 µm	22 µm	26 µm

5.3.2 Mechanical testing

The four Mg-Y alloys were quasi-statically tested at room temperature under compression along the rolling direction (RD-C), compression along the normal direction

(ND-C) and tension along the rolling direction (RD-T), all at room temperature. Tension and compression samples for mechanical testing were machined from the rolled sheets using electrical discharge machining (EDM). Compression samples were ~ 3.3 × 3.3 × 5 mm cuboids, with the compression axes along RD or ND. Dog-bone shaped tension samples had a gauge length of 20 mm along the RD and a rectangular cross section of 4 × 2 mm, following ASTM E8 standard (*Standard Test Methods for Tension Testing of Metallic Materials*). Uniaxial tension and compression mechanical tests were performed at a constant crosshead speed with a nominal strain rate of ~10^{-3} s^{-1} using an 8801 servo-hydraulic universal testing system (Instron Inc., USA) equipped with a dual-camera video extensometer for non-contact, high-resolution strain measurement. For the analyses of microstructure and texture evolution, mechanical tests were interrupted at various strain conditions.

5.3.3 Microstructural characterization

To conduct crystallographic texture analysis, pole figures of the four Mg-Y alloys were measured by a SmartLab X-ray diffractometer (XRD, Rigaku, Japan) using Cu Kα (λ=0.1542 nm) radiation under in-plane diffraction mode. Three pole figures of {0002}, {10-10}, and {10-11} were collected for each sample and plotted using the open source MTEX software package (Bachmann et al., 2010). For an investigation of the texture evolution, pole figures were measured for Mg-0.2Y samples deformed in RD-C to 5%, 7% and 13% strain and in ND-C to 10% strain, respectively. The strain values mentioned in this paper were recalculated into true strain.

To investigate the structure of pyramidal dislocations, TEM characterization of ND-C 2% pre-strained Mg-1Y samples was carried out using a JEOL JEM 2800 (JEOL, Japan) operating at 200 kV. For comparison, a 2% strain ND-compressed, commercially pure Mg sample (99.9%, Goodfellow Inc., USA) was also investigated by TEM. To prepare TEM specimens, pre-strained samples were cut into 1.0-to-1.5 mm thin foils from the center of the compression sample parallel to the ND $\times$ RD plane. The thin foils were then mechanically ground and sequentially polished down to 1 μm diamond suspension, followed by chemical polishing in a nitric acid:ethanol = 1:9 solution for 10 s. Finally, the samples were punched into Φ 3 mm disks and ion polished to electron transparency using PIPS (Gatan Inc., USA) at approximately 100°C, with ion-beam energies from 5 keV down to 1.5 keV and milling angles from 6° to 2°.

Electron backscatter diffraction (EBSD) maps were collected from RD-C deformed Mg-Y alloys to analyze their tendency to twin. EBSD was performed with a field emission scanning electron microscope (SEM, GAIA3, Tescan Inc., Czech Republic) operating at 20 kV, equipped with an Oxford AztecHKL NordlysMax2 integrated EBSD system. The partially deformed RD-C samples, deformed to ~5% true strain, were sectioned parallel to the RD $\times$ ND plane using EDM. For EBSD characterization, the samples were mechanically polished down to 0.05 μm colloidal silica in ethylene glycol followed by chemical etching using an etchant of nitric acid:hydrochloric acid:ethanol = 1:2:7. To get a statistically representative dataset on the deformed microstructure, EBSD maps were acquired from six 500 $\times$ 500 μm randomly selected regions for each alloy, with a scanning step size of 1 μm. Twin statistics were analyzed from the EBSD scans using QTcrystals developed by

Pradalier et al. (2018) to identify the twin/parent orientation relationship and calculate the twin area fractions.

5.4 Simulation procedures

Some of the experimental measurements described in the previous section served as inputs into the model, such as the initial crystallographic texture, initial morphological texture (i.e., grain shape distribution), and the applied boundary conditions. One input required is the slip and twinning modes to make available to the code. Here, the slip and twinning modes permitted to be used in the calculation are those commonly observed in a wide range of experiments on Mg-Y alloys: $\{0001\}\langle 11\bar{2}0\rangle$ basal slip, $\{10\bar{1}0\}\langle 1\bar{2}10\rangle$ prismatic slip, $\{10\bar{1}1\}\langle 11\bar{2}3\rangle$ pyramidal slip, and $\{10\bar{1}2\}\langle\bar{1}011\rangle$ extension twin (Agnew et al., 2001; Agnew and Duygulu, 2005; Rikihisa et al., 2017; Sandlobes et al., 2013; Takernoto et al., 2020; Yoshinaga and Horiuchi, 1963). TEM and EBSD analyses on the Mg-Y alloys in the experiments in Section 5.2 and an *in-situ* TEM study of a Mg-2.5 at.% Y alloy from another work (Zhang et al., 2019b) also observed dislocations from these same modes and $\{10\bar{1}2\}\langle\bar{1}011\rangle$ type extension twins. Other twin types, such as the $\{10\bar{1}1\}$ contraction twins and $\{10\bar{1}2\}$-$\{10\bar{1}1\}$ double twins, while seen in other Mg alloys were not observed in the present experiments. This result is consistent with recent work by Ansari et al., who studied the influence of Y addition (5 wt.% and 10 wt.%) on the recrystallization, texture and mechanical properties of Mg–Y alloys (Ansari et al., 2020). In their work, double twins and contraction twins are found to be dominant in Mg-10 wt.% Y, while only the $\{10\bar{1}2\}$ extension twin is dominant in the Mg-5 wt.% Y alloy (Ansari et al., 2020). This difference was explained by a significant decrease in the basal pole texture

intensity. In the present work, the Y concentration is not only lower than 5 wt.%, but the texture is also stronger; therefore, it is reasonable to only consider $\{10\bar{1}2\}$ twin system in the calculations.

Each slip mode is assigned a very small initial dislocation density of $1\times10^{10}/m^2$, a value that has been found to not affect the evolving dislocation density in prior studies (Ardeljan et al., 2016). For the initial texture the model material used the measured texture for each alloy, represented using 1000 weighted orientations. The initial shape for all grains is spherical, representing the nearly equiaxed structure. The mechanical tests were simulated by imposing 0.002 strain increments along the RD or ND, in the appropriate sense of loading (compression or tension), while enforcing zero average stress along the lateral two sample directions. The macroscopic strain rate is 0.001, equal to that used in the experimental tests. In simulation, the dislocation density, grain shape and texture were continuously updated. The calculated textures are plotted also using the MTEX software to compare directly with the measurement (Bachmann et al., 2010).

5.5 Experimental Results

In this subsection, the results of the experimental work are reviewed so that the study will be self-contained. While they are not performed by the Ph.D. candidate, they are integrated with the modeling component, which is carried out by the Ph.D. candidate. To be self-contained.

5.5.1 Initial microstructures and textures

After hot rolling to the same thickness reduction and recrystallization annealing, the microstructures of the four Mg-Y alloys were characterized using optical microscopy (Figure 5-1). The micrographs revealed a nearly equiaxed and twin-free microstructure with no detectable precipitates. The equilibrium solubility limit of Y in Mg at ambient temperatures is ~0.6 wt.% Y. Using XRD, it is found that evidence of a second phase only in the Mg-3Y alloy. The average grain sizes measured from optical microscopy are listed in Table 5-1. To achieve a similar average grain size in the alloys, higher annealing temperature and/or longer annealing time is needed for alloys with a higher Y concentration. It is noted that due to the rapid grain growth of Mg-0.2Y at elevated temperatures, its grain size is slightly larger compared to the other three Mg-Y alloys, despite the lowest temperature and shortest annealing time being used.

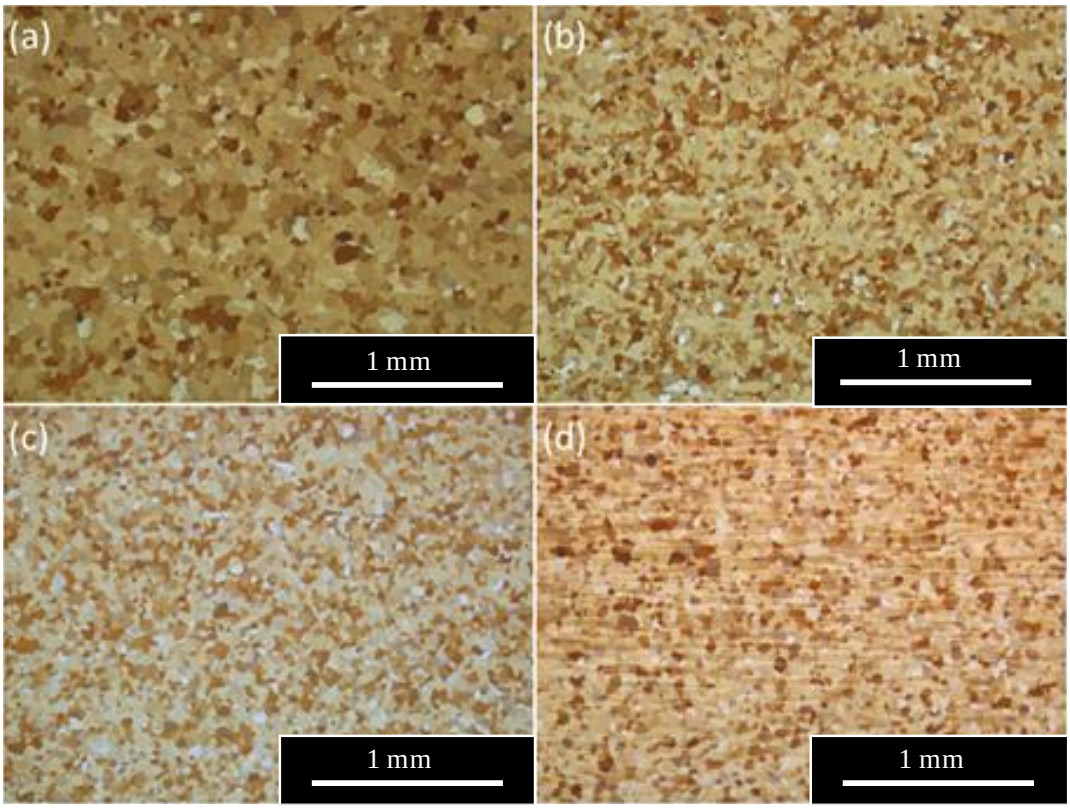

Figure 5-1 *Optical micrographs showing the microstructure of recrystallized Mg-Y plates: (a) Mg-0.2Y; (b) Mg-0.6Y; (c) Mg-1Y; (d) Mg-3Y. Note that the grain sizes are similar in Mg-0.6Y, Mg-1Y, and Mg-3Y, whereas Mg-0.2Y exhibits a slightly larger grain size due to the rapid grain growth in Mg with low Y content, This image is taken with permission from (Wang et al., 2021)*

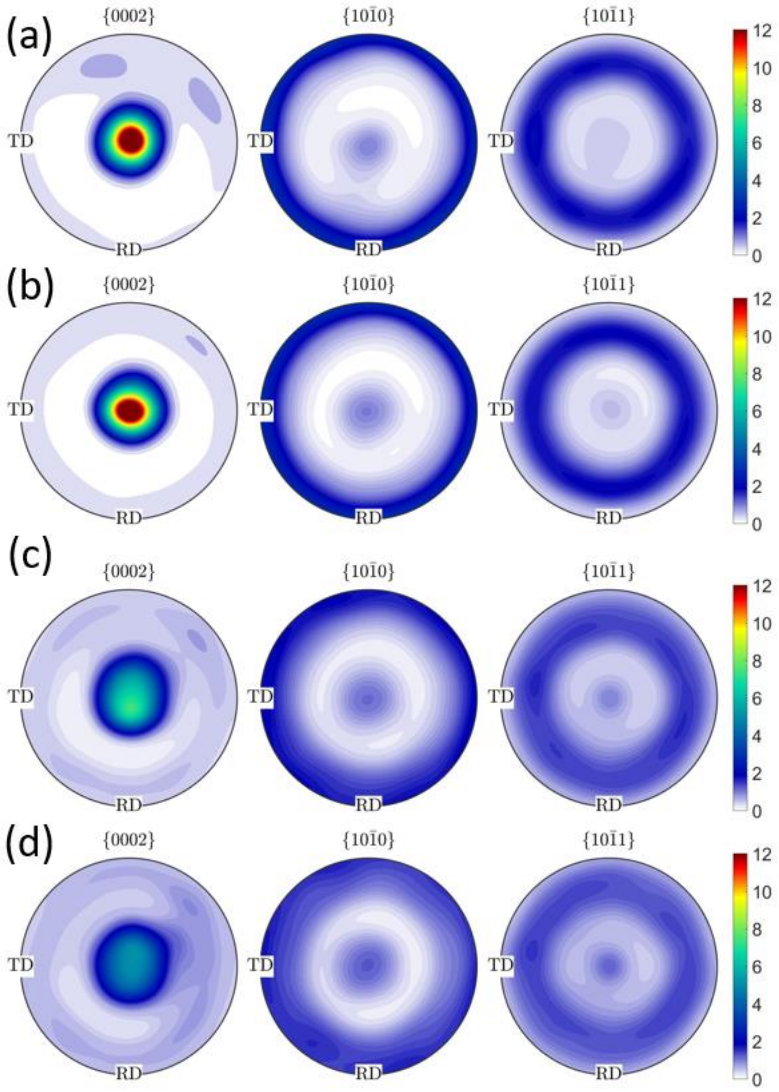

Figure 5-2 Experimentally determined {10-10}, {0002} and {10-11} pole figures showing the initial rolling texture measured using XRD for: (a) Mg-0.2Y, (b) Mg-0.6Y, (c) Mg-1Y and (d) Mg-3Y.

The starting textures were measured using XRD. Figure 5-2 shows the $\{10\bar{1}0\}$, $\{0002\}$ and $\{10\bar{1}1\}$ pole figures of the initial textures for these four alloys. All alloys exhibit primarily basal type rolling textures. However, a noticeable texture weakening effect with an increase in the Y concentration is observed. The maximum basal texture intensities are

21.2, 15.7, 7.3 and 5.3 multiples of uniform distribution (m.u.d.), respectively, for Mg-0.2Y, Mg-0.6Y, Mg-1Y and Mg-3Y.

5.5.2 Mechanical response

Quasi-static uniaxial mechanical tests along three loading directions were performed at room temperature on the four Mg-Y alloys. The stress-strain curves up to the ultimate stress are presented in Figure 5-3 (a, b and c) for the ND-C, RD-C and RD-T test directions, respectively. According to the initial basal rolling texture of these alloys, in the ND-C test, the compression direction is roughly parallel to the c-axes for most of the grains, a condition which would favor pyramidal $\langle \boldsymbol{c}+\boldsymbol{a} \rangle$ slip. For ND-C, the 0.2% offset yield strengths $\sigma_{0.2\%}$ are 83, 105, 97 and 101 MPa for Mg-0.2Y, Mg-0.6Y, Mg-1Y and Mg-3Y, respectively. After yielding, the hardening rate continuously decreases with increased strain, suggesting a slip-dominated response (Lentz et al., 2015b; Risse et al., 2017). In contrast, in the RD-C test, the compression axis is perpendicular to the c-axes of most of the grains, requiring the crystals to extend along the c-axis. The stress-strain curves in this case have a sigmoidal shape, i.e., the strain hardening rate first increases and then decreases after yield, which is a typical signature for $\{10\bar{1}2\}\langle\bar{1}011\rangle$ twinning-dominated deformation. The $\sigma_{0.2\%}$ for RD-C of Mg-0.2Y, Mg-0.6Y, Mg-1Y and Mg-3Y are 46 MPa, 64 MPa, 67 MPa and 78 MPa, respectively, lower than those in the ND-C test. During RD-T, when the tension axis is perpendicular to the c-axes, activation of prismatic $\langle \boldsymbol{a} \rangle$ slip would be, however, favored instead of $\{10\bar{1}2\}\langle\bar{1}011\rangle$ twinning or pyramidal $\langle \boldsymbol{c}+\boldsymbol{a} \rangle$ slip. The $\sigma_{0.2\%}$ values for Mg-0.2Y, Mg-0.6Y, Mg-1Y and Mg-3Y are higher than those for ND-C and much higher than those for RD-C and are 112, 126, 107 and 110 MPa, respectively. For a

general view, the yield strengths as a function of loading direction and composition are plotted in Figure 5-4.

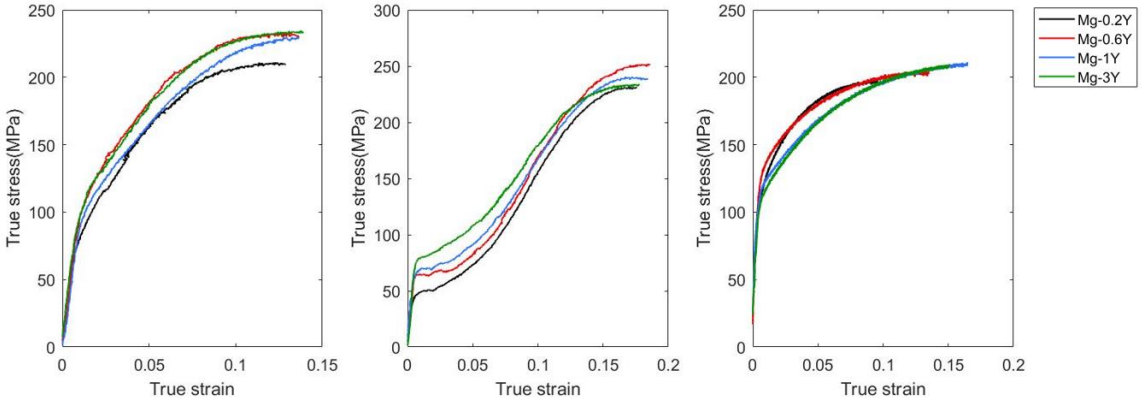

Figure 5-3 Experimental stress-strain curves for the for Mg-Y alloys under: (a) normal direction compression (ND-C), (b) rolling direction compression (RD-C), and (c) rolling direction tension (RD-T). This image is taken with permission from (Wang et al., 2021)

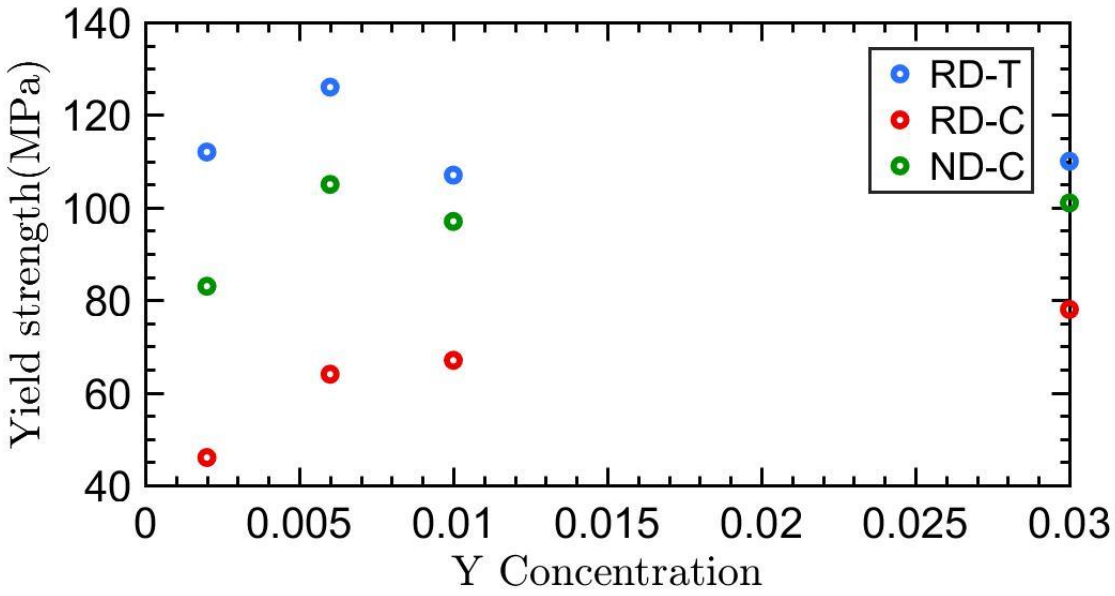

Figure 5-4 Yield strength for Mg-Y in different loading directions and composition. This image is taken with permission from (Wang et al., 2021)

5.5.3 Observation of Pyramidal $\langle \boldsymbol{c}+\boldsymbol{a} \rangle$ slip

To investigate the change in pyramidal $\langle \boldsymbol{c}+\boldsymbol{a} \rangle$ slip activity in Mg-Y compared to pure Mg, TEM analyses were performed on the deformed microstructure of the ND-C material. Figure 5-5 shows typical two-beam bright and dark field TEM images of ND-C deformed Mg-1Y at grains with c-axes close to the compression axis. The diffraction vector g = 0002 was used to identify the presence of dislocations with non-basal Burgers vectors ($\langle \boldsymbol{c} \rangle$ type dislocations). A uniform distribution of $\langle \boldsymbol{c} \rangle$ type dislocations is observed, with many of them lying partially along the basal plane trace and partially out of the basal plane.

Figure 5-6 shows, for comparison, a TEM image of the ND-C deformed pure Mg to the same strain. Overall, the density of $\langle \boldsymbol{c} \rangle$ type dislocations is lower than in Mg-Y. Also, the $\langle \boldsymbol{c} \rangle$ type dislocations are localized at regions corresponding to stress concentrations, such

as grain boundaries, twin boundaries or slip bands. Figure 5-6 shows a band of $\langle \boldsymbol{c} \rangle$ type dislocations that are found in front of a twin tip located at the top left corner of the micrographs. The non-uniform distributions of $\langle \boldsymbol{c} \rangle$ type dislocations existing only close to stress concentrators in pure Mg in contrast to the uniformly distributed $\langle \boldsymbol{c} \rangle$ type dislocations in Mg-1Y suggests that their activation is more difficult in pure Mg and requires a higher local stress than Mg-1Y.

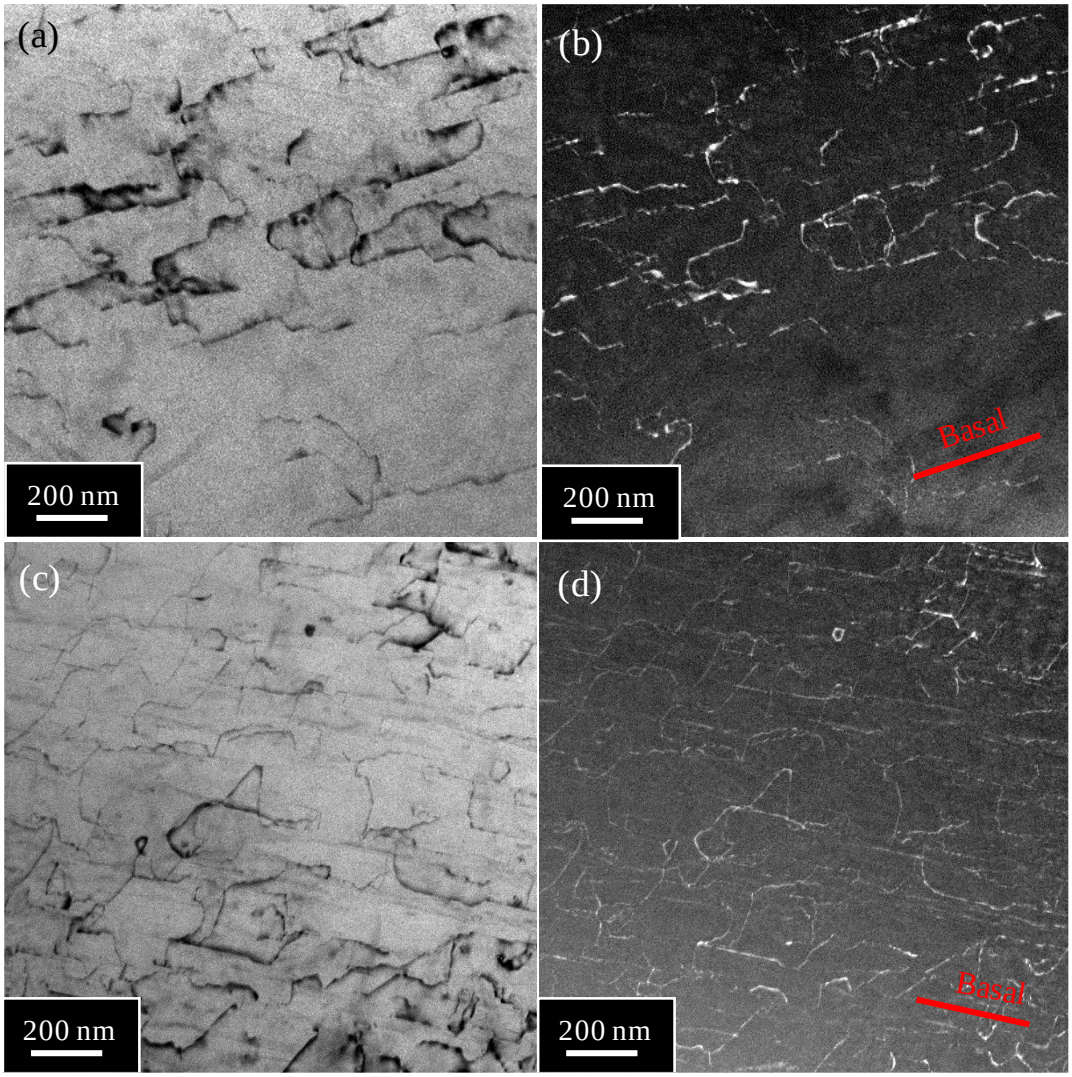

Figure 5-5 Representative TEM micrograph of ~2% ND compressed Mg-1Y, at zone axes of (a, b) B = 11-20 and (c, d) B=10-10, with diffraction vector g = [0002] showing the general activation of dislocations with $\langle \boldsymbol{c}+\boldsymbol{a} \rangle$ Burgers vectors. This image is taken with permission from (Wang et al., 2021)

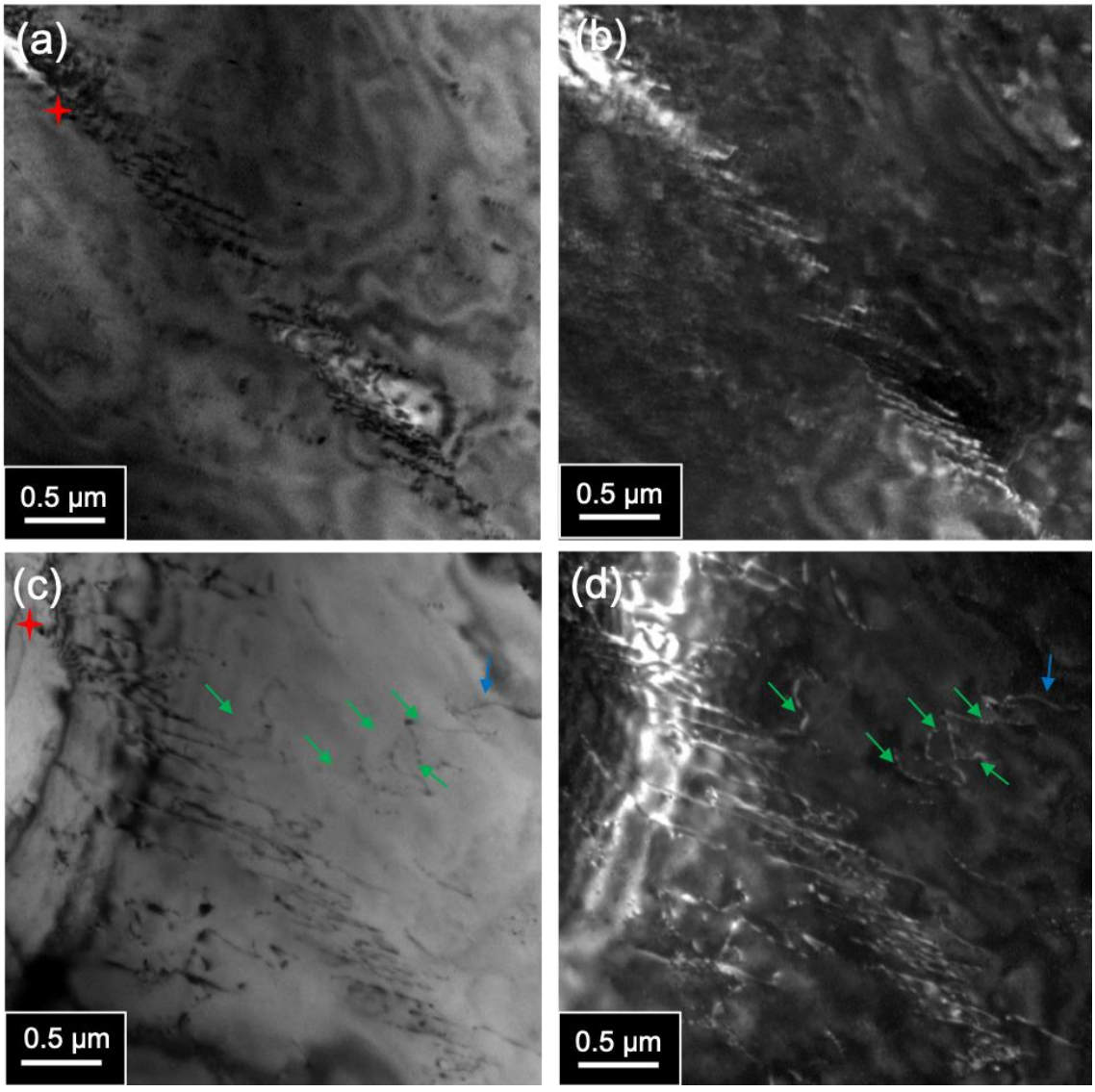

Figure 5-6 A slip band of $\langle \boldsymbol{c}+\boldsymbol{a} \rangle$ dislocations in front of a twin tip in pure Mg with (a, b) g = [0002] and some $\langle \boldsymbol{a} \rangle$ dislocations are seen with (c, d) g = [10-10]. Green arrows mark the <a> dislocations out of the basal plane, and blue arrows mark the basal $\langle \boldsymbol{a} \rangle$ dislocations. The red star points at a fiduciary mark just to guide the eye. This image is taken with permission from (Wang et al., 2021)

5.6 Model Results

5.6.1 Simulations of Y-affected deformation response

The observed effects of Y concentration on stress-strain response and T-C asymmetry could be due to several factors. They may be attributed to texture weakening and/or changes in the resistances for the slip and twinning modes as Y changes. Y concentrations are found here to affect the initial texture, weakening it as Y increases, a factor that could also contribute to lower T-C asymmetry. As shown in Figure 4-2, the initial textures for these four Mg-Y alloys are relatively strong with most grains with their c-axes oriented through the ND of the rolled sheet. In polycrystals, each grain by virtue of their different orientations will have different slip activities, involving multiple active slip systems and twin evolution. In addition, the reason for lower T-C asymmetry can also be attributed to the strengthening effect on each deformation mode due to Y alloying. A third factor concerns the interplay between slip, twinning, and texture evolution. When deformed under an applied strain, the texture changes, and thus, the relative activities of the different slip and twinning modes could change with strain as well. Thus, many factors are at play, which can complicate identifying how Y concentration impacts stress-strain response. To transcend the effects of texture and pointedly connect the stress-strain response of Mg-Y alloys to the activation of the various slip and twinning modes, VPSC polycrystal modeling was employed. All three distinct loading paths, RD-C, RD-T, and ND-C, and for four binary Mg-Y alloys were simulated.

One of the main results from this work is the identification of a single set of material-related hardening parameters that enabled the simulation to replicate all three stress-

strain curves for each alloy Y concentration: Mg-0.2Y, Mg-0.6Y, Mg-1Y and Mg-3Y. Figure 5-7-figure 5-9 compare the calculated true stress-strain response with the measured stress-strain response. The model captures reasonably well the evolution in stress and hardening rates in all tests. Some slight deviations are noted, for instance in the Mg-0.6Y curve for RD-T. Although the flow stress is a little overestimated in this one case, the strain hardening is accurately captured. The corresponding parameter sets are given in Table 5-2 for the four Mg-Y alloys. Other predictions from the model are slip mode activity and evolution of texture and twin volume fraction with strain, which are discussed in turn below.

Table 5-2 Parameters used for VPSC modeling for Mg-Y alloys. Superscript α refers to the slip mode (α = 1, 2, 3) and superscript β refers to the twin mode. The definitions of the parameters are provided in the text.

	Alloy	τ_0^α (MPa)	k_0^α (m^{-1})	D (MPa)	g	Q	$HP^{\alpha 1}$	C
Basal ($\alpha = 1$)	Mg-0.2Y	6	2.5 x 10^9	500	0.003	12	0	1000
	Mg-0.6Y	9	1.5 x 10^9	500	0.003	20	30	1000
	Mg-1Y	11	1.5 x 10^9	800	0.003	20	0	1000
	Mg-3Y	22	1.5 x 10^9	1000	0.002	5	100	1000

Prismatic ($\alpha = 2$)	Mg-0.2Y	105	4×10^9	6000	0.002	0	500	1000
	Mg-0.6Y	85	4×10^9	6000	0.002	0	500	1000
	Mg-1Y	85	4×10^9	6000	0.002	0	100	1000
	Mg-3Y	85	4×10^9	6000	0.002	5	500	1000
Pyramidal 2nd <a+c> ($\alpha = 3$)	Mg-0.2Y	90	5×10^8	2000	0.002	0	500	1000
	Mg-0.6Y	100	4×10^9	6000	0.002	0	500	1000
	Mg-1Y	100	6×10^8	2000	0.002	0	500	1000
	Mg-3Y	110	6×10^9	2000	0.002	0	500	1000
Extension Twin ($\beta = 1$)	Mg-0.2Y	10						
	Mg-0.6Y	10						
	Mg-1Y	13						
	Mg-3Y	13						

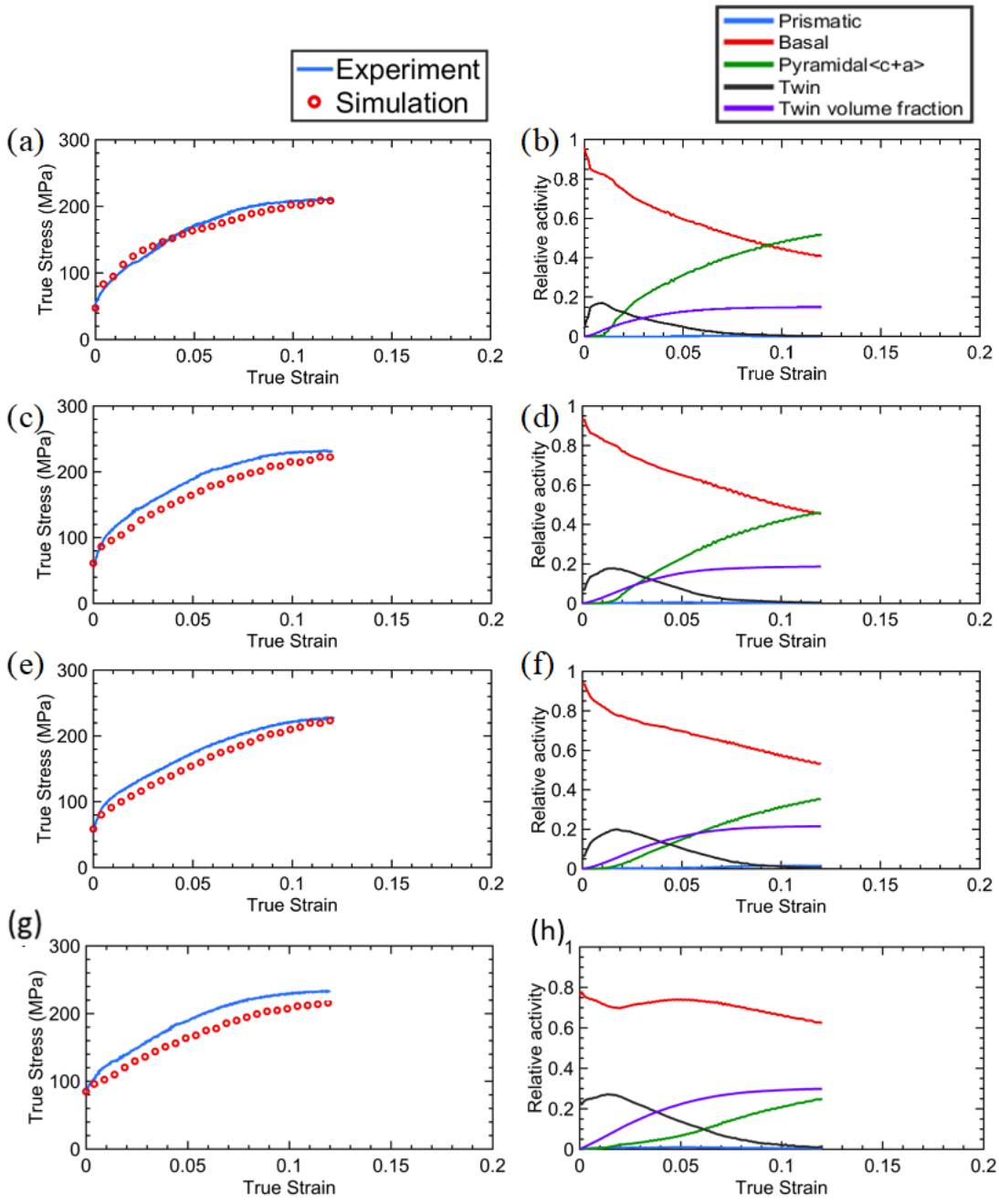

Figure 5-7 Experimental and simulated stress-strain curves for ND-C for: (a) Mg-0.2Y, (c) Mg-0.6Y, (e) Mg-1Y and (g) Mg-3Y; and the corresponding plots of the relative activity of multiple slip and twinning modes for: (b) Mg-0.2Y, (d) Mg-0.6Y, (f) Mg-1Y and (h) Mg-3Y, respectively

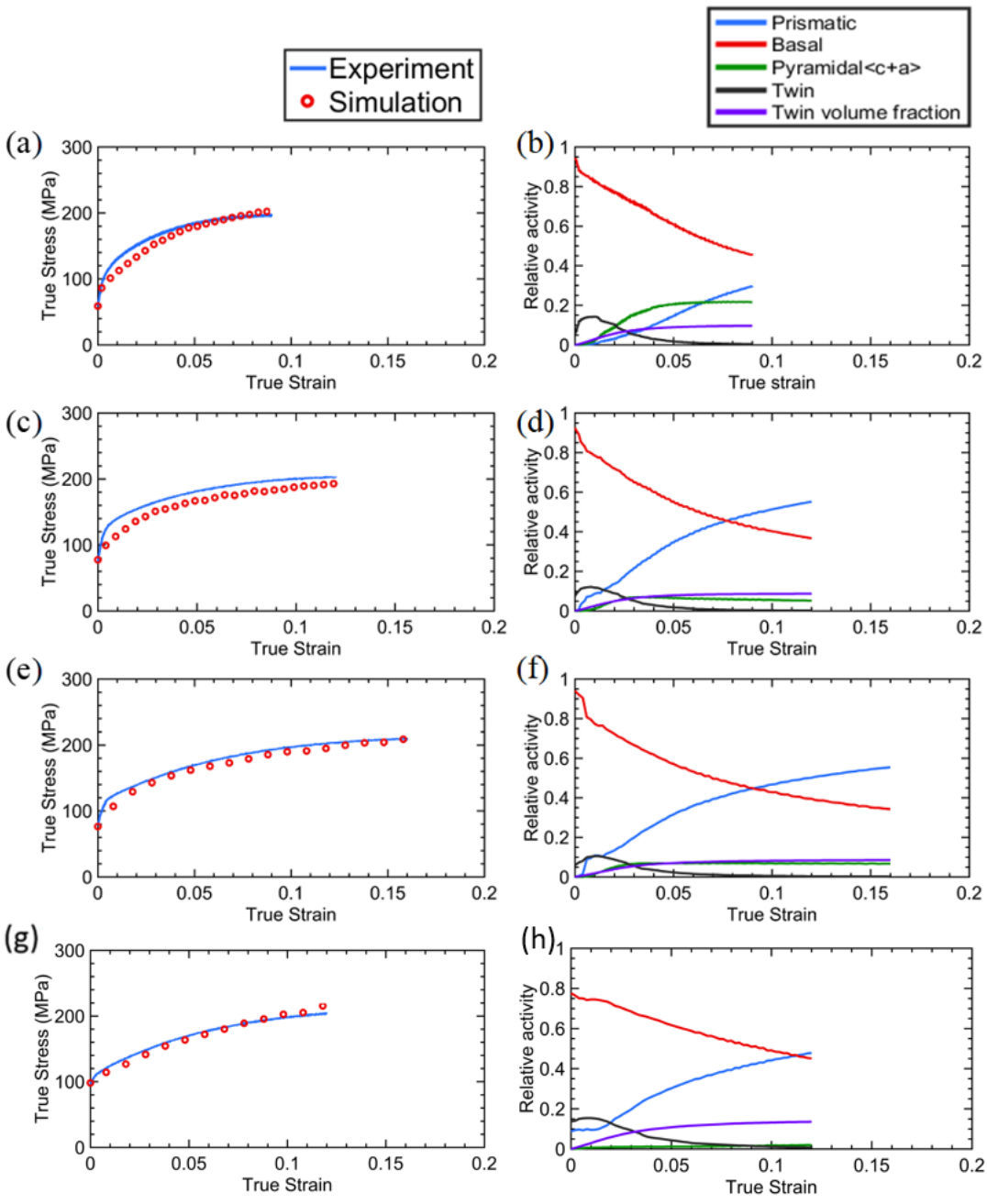

Figure 5-8 Experimental and simulated stress-strain curves for RD-T for: (a) Mg-0.2Y, (c) Mg-0.6Y, (e) Mg-1Y and (g) Mg-3Y; and the corresponding plots of the relative activity of multiple slip and twinning modes for: (b) Mg-0.2Y, (d) Mg-0.6Y, (f) Mg-1Y and (h) Mg-3Y, respectively.

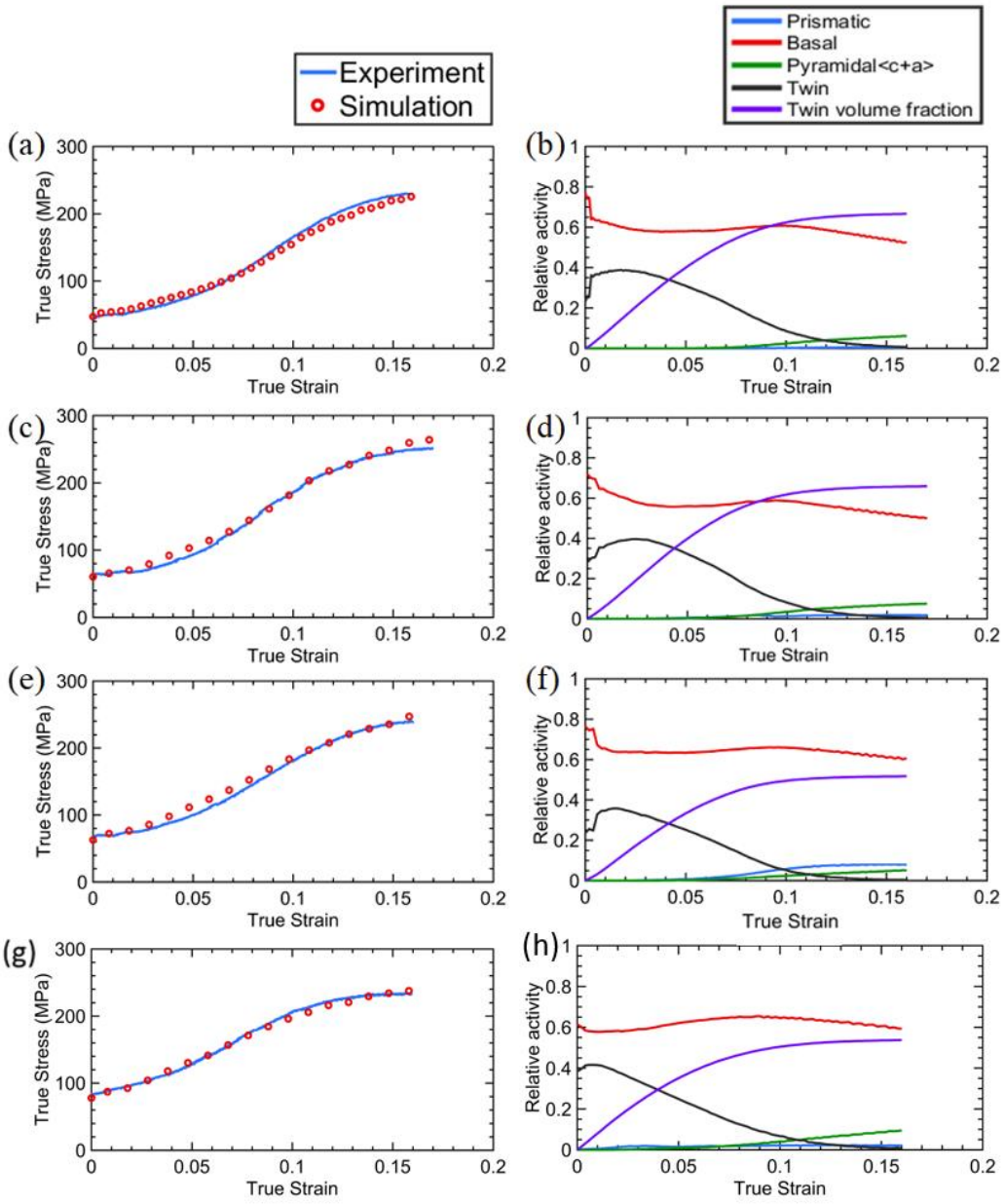

Figure 5-9 Experimental and simulated stress-strain curves for RD-C for: (a) Mg-0.2Y, (c) Mg-0.6Y, (e) Mg-1Y and (g) Mg-3Y; and the corresponding plots of the relative activity of multiple slip and twinning modes for: (b) Mg-0.2Y, (d) Mg-0.6Y, (f) Mg-1Y and (h) Mg-3Y, respectively.

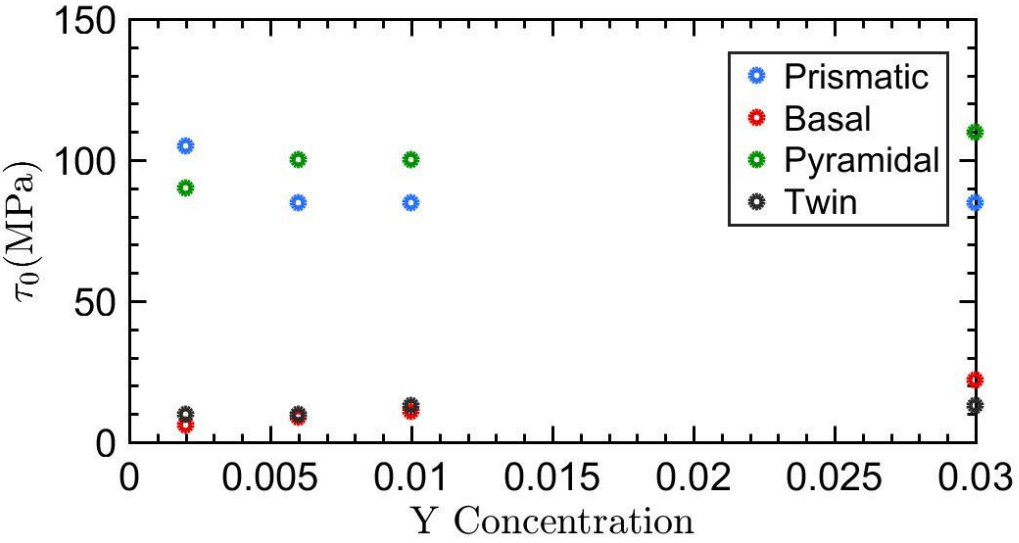

Figure 5-10 Predicted initial resistances for various slip and twinning modes in Mg-Y as a function of Y concentration.

5.7 Discussion

5.7.1 Influence of Y concentration on initial critical activation stresses for slip and twinning

Figure 5-10 shows the variation in τ_0^α and τ_0^β with Y concentration for each slip and twinning mode. Basal slip remains the easiest deformation mechanism for the binary Mg-Y alloy, a result that is consistent with many previous works on Mg and Mg alloys (Agnew et al., 2001; Roberts, 1960; Yoshinaga and Horiuchi, 1963). The non-basal slip modes are substantially larger than that for basal slip. The initial resistance for basal slip exhibits a proportional dependency on Y concentration, increasing with increasing amounts of Y concentration. The τ_0^α for prismatic slip and for twinning, however, are notably less sensitive to Y concentration. For comparison, similar models have reported lower τ_0^α

values of 3 MPa, 36 MPa, and 86 MPa for basal, prismatic, and pyramidal slip for pure Mg (Beyerlein et al., 2011).

A few studies have focused on the effect of Y on CRSS values, with results that are not consistent with those reported here. Stanford et al. (2014) investigated the CRSS values for various deformation modes in Mg-0.5 wt.% Y and Mg-2.2 wt.% Y using the elasto-plastic self-consistent method. They found that for this composition range, no additional hardening on basal slip and extension twinning were observed. They state that this observation implies that the solute strengthening of these deformation modes is exhausted when concentrations reach 0.5 wt.% Y. The results here, however, suggest that there is a strengthening effect on these two deformation modes, although it is small. A strengthening effect on first-order pyramidal slip is also observed, in agreement with a few studies (Kula et al., 2017; Rikihisa et al., 2017), but not one on prismatic slip. Kula et al. (2017) studied Mg-Y binary alloys with Y concentrations ranging from 1 wt.% to 4 wt.%. In the range 1 wt.% to 3 wt.%, they also found little change in the CRSS values for prismatic slip (less than 5 MPa), consistent with the finding. They only observed large changes in CRSS from 3 wt.% to 4 wt.%. It should be noted that the τ_0^α analyzed here only represents the initial CRSS value, and in the model the CRSS can rise from τ_0^α as strain evolves. Arguably, more important than absolute CRSS values are the change in the CRSS (non-basal)/CRSS (basal) ratio with increasing amounts of Y. Here it is shown that τ_0^α for basal slip increases faster compared with the non-basal slip, resulting in the reduction in this ratio as Y concentration increases.

5.7.2 Y-dependent slip and twinning activity in Mg-Y alloys

From the polycrystal model calculations, the polycrystal average amounts of slip and twinning contributed by each mode can be extracted. The columns on the right-hand side of Figure 5-7-Figure 5-9 present the calculated relative activities (RA^{α}) of basal slip, prismatic slip, and pyramidal $\langle \boldsymbol{c}+\boldsymbol{a} \rangle$ slip and activities of $\{1\bar{0}12\}\langle\bar{1}011\rangle$ extension twinning during strain evolution. It is first noticed that the relative slip activity for basal slip dominates in all Y concentrations and in all loading directions. The amount and type of secondary slip, as well as the participation of twinning, is, however, highly dependent on the loading direction and Y concentration.

From figure 5-6, for the four Mg-Y alloys being investigated, the hardening rate in the flow stress-strain response in ND-C decays with strain, indicating that their deformation is dominated by slip. In agreement, the VPSC calculation indicates that the response was enabled by the activation of slip and little twinning. Deformation twinning occurs only in the early stages and reduces in activity with increased ND-C strain. For the full range of Y, the twin volume fraction saturates to 15%-20% at a strain level around 8%. As mentioned, basal slip dominates, but, apart from basal slip, pyramidal $\langle \boldsymbol{c}+\boldsymbol{a} \rangle$ slip is the secondary slip mode, while prismatic slip activity is negligible. With ND-C straining, the contribution of pyramidal $\langle \boldsymbol{c}+\boldsymbol{a} \rangle$ slip increases, while that for basal slip decreases. With increasing Y concentration, the relative contribution of pyramidal $\langle \boldsymbol{c}+\boldsymbol{a} \rangle$ slip with respect to basal slip decreases. This reduction in $\langle \boldsymbol{c}+\boldsymbol{a} \rangle$ contribution causes the reduced hardening rate observed with higher concentrations of Y during ND-C.

Like in ND-C, the hardening rate decreases with strain in RD-T (Figure 5-8), suggesting also slip-dominated plasticity. In accord, the calculations of the slip and twinning activities indicate that the primary slip mode is basal slip, while the secondary slip mode is prismatic slip. Compared to the other two loading directions, deformation twinning contributes the least in RD-T. For all four Y concentrations, the relative contribution of prismatic slip rises with increased strain. As Y concentration increases from Mg-0.2Y to Mg-1Y, the contribution of prismatic slip increases. But for Mg-3Y, the relative activity of prismatic slip reduces below that in Mg-0.6Y and Mg-1Y. The predicted τ_0^{α} value for prismatic slip is insensitive to Y, being especially similar in Mg-3Y, Mg-1Y and Mg-0.6Y. Therefore, the lower activity of prismatic slip in the RD-T test for Mg-3Y can be attributed to its weaker initial texture.

Distinct from the other two loading directions, the flow stress-plastic strain response for RD-C exhibits a sigmoidal shape, a typical signature for twinning-dominant deformation behavior. The calculations predict that basal slip and twinning are the more active modes for the entire straining period, with pyramidal slip activity substantially lower and prismatic slip virtually inactive. In this test, twinning directly competes with and evidently, is favored over pyramidal $\langle \boldsymbol{c} + \boldsymbol{a} \rangle$ slip. With further straining (> 5%), the twinning rate starts to decrease, and non-basal slip becomes active, although still in small amounts. Table 5-3 compares the calculated strains at which twinning activity reduces and non-basal slip activity initiates. As shown, as Y increases, the strain at which twinning activity reduces and non-basal slip activity initiates decreases. When the maximum flow stress is reached, the calculated twin volume fraction is substantial, lying within a range of 40-60%

(Figure 5-9). The relatively activities among the slip and twinning modes are similar for all Y concentrations. There is slightly less twinning activity and twin volume fraction at a given strain for greater Y concentrations.

Table 5-3 The critical strain at which twinning activity reduces and non-basal slip activity initiates decreases

	Mg-0.2Y	Mg-0.6Y	Mg-1Y	Mg-3Y
Twinning activity reduce	0.023	0.026	0.016	0.008
Non-basal slip activity initiates	0.074	0.062	0.058	0.024

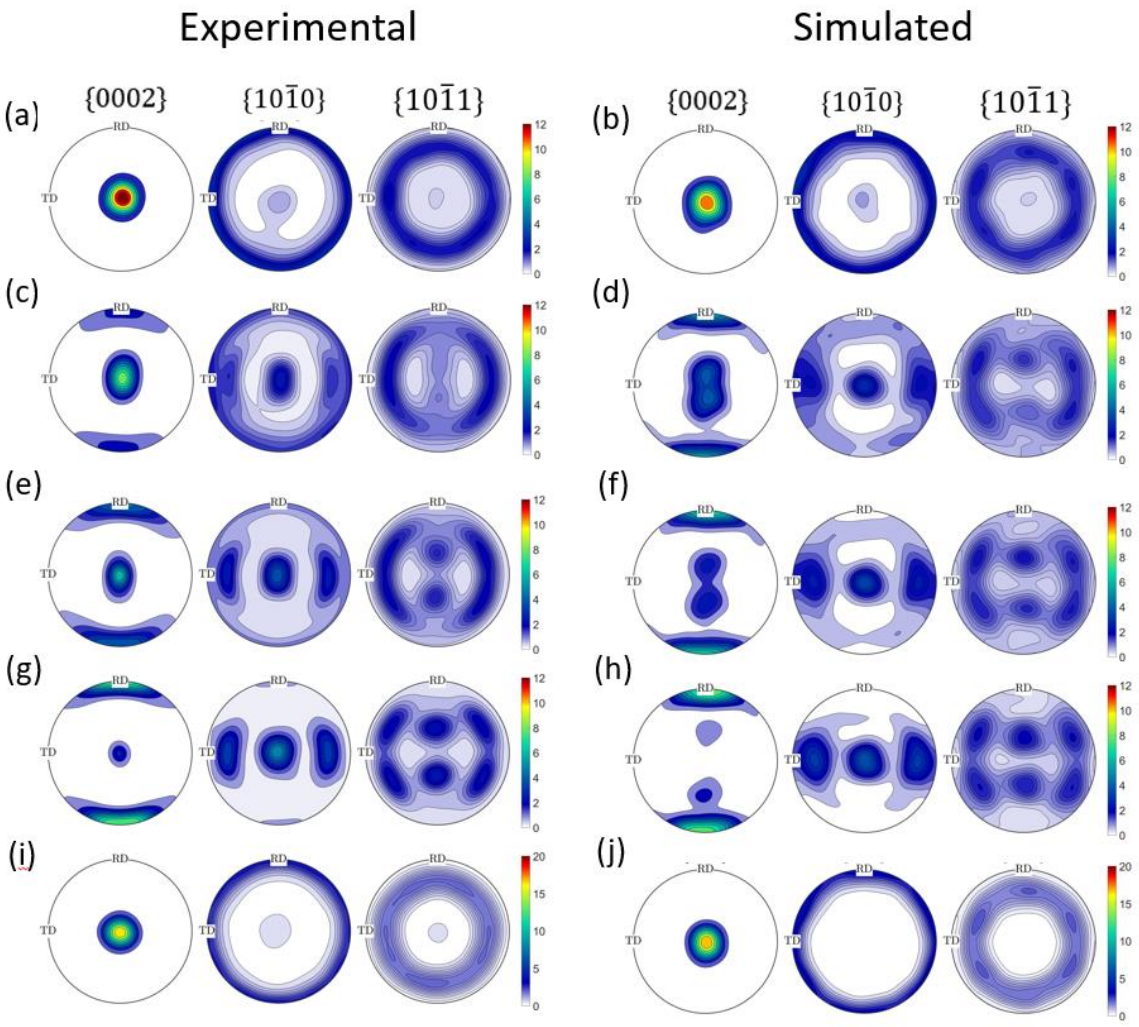

Figure 5-11 Experimental and simulated pole figures showing the texture evolution in Mg-0.2Y alloys: (a, b) initial, (c, d) 5% RD-C, (e, f) 7% RD-C, (g, h) 13% RD-C and (i, j) 10% ND-C.

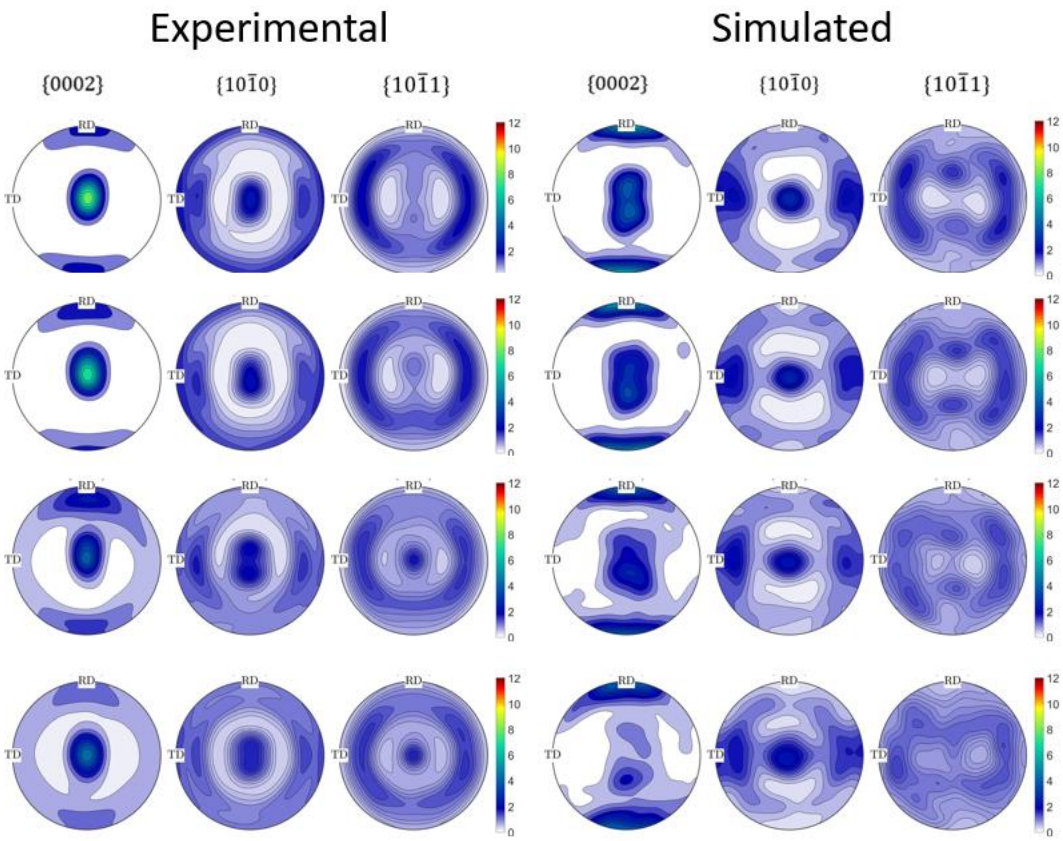

Figure 5-12 Experimental and simulated pole figures of 5% RD-C deformed Mg-Y alloys: (a, b) Mg-0.2Y, (c, d) Mg-0.6Y, (e, f) Mg-1Y and (g, h) Mg-3Y.

5.7.3 Effect of Y on twinning

Twin fractions can be detected post-mortem indirectly via texture analyses and directly with EBSD. Figure 5-11 compares the XRD measured and VPSC simulated pole figures for Mg-0.2Y at the as-annealed state and after 5%, 7% and 13% RD-C deformation and after 10% ND-C. The measurement shows that the initial texture of Mg-0.2Y has a basal rolling texture, with strong basal pole intensity at the ND. The representation of the initial texture used in the model is evidently reasonable. In the RD-C test, the basal pole intensity at ND decreases, while the intensity at RD increases, corresponding to a ~90° rotation of

the grain orientation. The formation of $\{10\bar{1}2\}\langle\bar{1}011\rangle$ twins, which reorient the crystal by ~86.3°, is one of the major causes of the abrupt change in the basal texture during RD-C. Up to a strain level of 7%, corresponding to the maximum strain hardening rate, the basal pole intensity grows stronger around RD rather than ND, as seen from both the experimental and simulation results. This change in texture indicates that the twin volume fraction has increased and potentially consumed most of the grains. When the RD-C strain increased to 13%, the basal pole density at RD has further intensified, suggesting that nearly all the crystals have been reoriented by $\{10\bar{1}2\}\langle\bar{1}011\rangle$ twinning.

Upon ND-C deformation, the measured and calculation textures show no substantial evolution. The deformation texture of Mg-0.2Y after 10% ND-C is like its initial basal texture, but with slightly higher basal pole intensity at ND. Although the model has predicted a twin volume fraction of 15% (Figure 5-7 d), the amount of reorientation is not sufficient to alter the bulk texture since the twins in the present case manifest as fine lamella. It has also been shown in several previous works that twin fractions need to exceed about 20% to manifest in bulk textures (Ardeljan et al., 2016; Knezevic et al., 2013; Niezgoda et al., 2014).

To examine the effect of Y concentration on texture evolution, Figure 5-12 presents the experimental and simulated deformation textures for Mg-0.2Y, Mg-0.6Y, Mg-1Y and Mg-3Y at the same strain, 5% RD-C. For all Mg-Y alloys, there is a ~90° reorientation of grains after RD-C that led to increased intensities around RD in the basal pole figures. With an increased amount of Y, the intensities in basal pole figures corresponding to $\{10\bar{1}2\}\langle\bar{1}011\rangle$ twinning decreased. Both modeling and measurements confirm the slip

and twinning activity predictions stated earlier--increased Y content reduces slightly the propensity of but does not shut off twinning.

Table 5-4 Fraction of $\{10\bar{1}2\}\langle 10\bar{1}\bar{1}\rangle$ *twins after ~5% true strain compression in the rolling direction (RD-C) .*

	Mg-0.2Y	Mg-0.6Y	Mg-1Y	Mg-3Y
Twin area fraction by EBSD	39%	36%	33%	25%
Twin volume fraction by VPSC	34.1%	32.2%	28.6%	30.1%

As an explicit way to identify Y concentration effects on twinning, the twin area fraction was measured using an EBSD-based statistical study for the four Mg-Y alloys when loaded in uniaxial RD-C condition to 5% true strain. Representative EBSD maps for 5% RD-C deformed Mg-0.2Y, Mg-0.6Y, Mg-1Y and Mg-3Y are shown in figure 5-13 (a-d), showing that all the samples contain profuse lenticular-shaped deformation twins. A careful statistical analysis was performed to quantify the twin fractions. In all samples, most of the twins are $\{1\bar{1}02\}\langle\bar{1}011\rangle$ twins, and the fraction of $\{10\bar{1}1\}\langle\bar{1}012\rangle$ twin type is negligible. Table 5-4 compares the area fractions of $\{10\bar{1}2\}\langle\bar{1}011\rangle$ twins measured by EBSD in the four alloys, with the values being 39%, 36%, 33% and 25% for Mg-0.2Y, Mg-0.6Y, Mg-1Y and Mg-3Y, respectively. Similar EBSD statistical analysis of extension twins in pure Mg show that the twin area fraction is about 60% for grains with a diameter of approximately

25 µm at 3% true strain (Beyerlein et al., 2011). Comparisons with the findings here suggests that Y addition suppresses the twin activity. VPSC calculations predicted both the relative activity of deformation twinning (Figure 5-9) and the twin volume fractions (Table 5-4 and Figure 5-14). The volume fraction of calculated by VPSC agree well with the EBSD results on twin area fractions

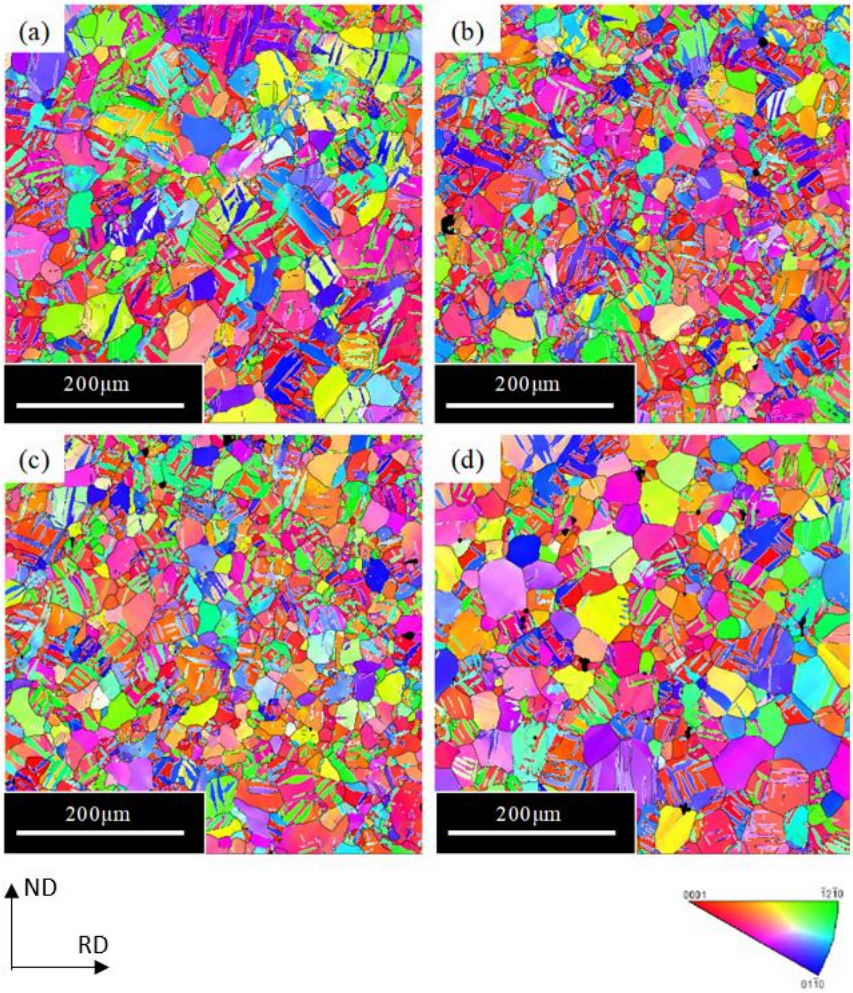

Figure 5-13 Representative EBSD inverse pole figure colored maps for 5% RD-C deformed Mg-Y alloys: (a) Mg-0.2Y, (b) Mg-0.6Y, (c) Mg-1Y and (d) Mg-3Y. This image is taken with permission from (Wang et al., 2021)

The relatively low propagation stresses for extension twinning, especially compared to those for prismatic and pyramidal slip, suggest that generally twinning remains an easily activated deformation mechanism in Mg-Y alloys. With an increase in Y concentration from 0.2 to 3 wt.%, the twin propagation stress slightly increases. The slightly increased propagation stress, in combination with the texture weakening with higher Y concentrations, can explain the lower fraction of twins in RD-C deformed Mg-Y and the reduced tension-compression yield asymmetry with a higher Y concentration.

5.7.4 Effect of Y on plastic anisotropy and slip-twin interactions

All four alloys exhibited similar plastic anisotropy despite the large changes in Y additions. Regarding rank, the yield stress is highest in RD-T, second in ND-C, and the lowest in RD-C. Thus, all four of the Mg-Y alloys show a RD T-C yield asymmetry greater than 1. The initial hardening rate are highest in ND-C for every alloy. However, Y concentrations affect the differences in the yield stress, among the different test directions. In this way, increases in Y additions lower the orientation dependent yield stress. The reduction can be attributed to a clear increase in the RD-C yield stress with increase in Y, since the changes in ND-C and RD-T yield stresses are not proportional or as pronounced. While the model predicts a reduced non-basal to basal initial CRSS ratio with increased Y, this ratio may not be the main reason for the reduced anisotropy. It is found that in ND-C, the contributions of pyramidal slip to deformation is important for all Mg-Y alloys but it tend to decrease slightly as Y increases. In RD-C, the twin volume fraction decreases with increasing Y and the pyramidal slip activity is slightly increased. Only in the RD-T tests does the contribution of prismatic slip increase as Y increases from 0.2% to 1%. The activity of

prismatic slip in the other two directions is relatively low. In fact, basal slip dominates in all loading directions and in all alloys and the non-basal contribution does not necessarily increase as Y increases. Other factors, such as initial texture, unidirectional activation of twinning, and loading direction, can also play a role. In Mg, the pyramidal-to-prismatic initial CRSS ratio can range from 2 to 5, while current study shows that this ratio in Mg-Y is small. The reduction in CRSS ratios with Y could be a reason for the reduced anisotropy.

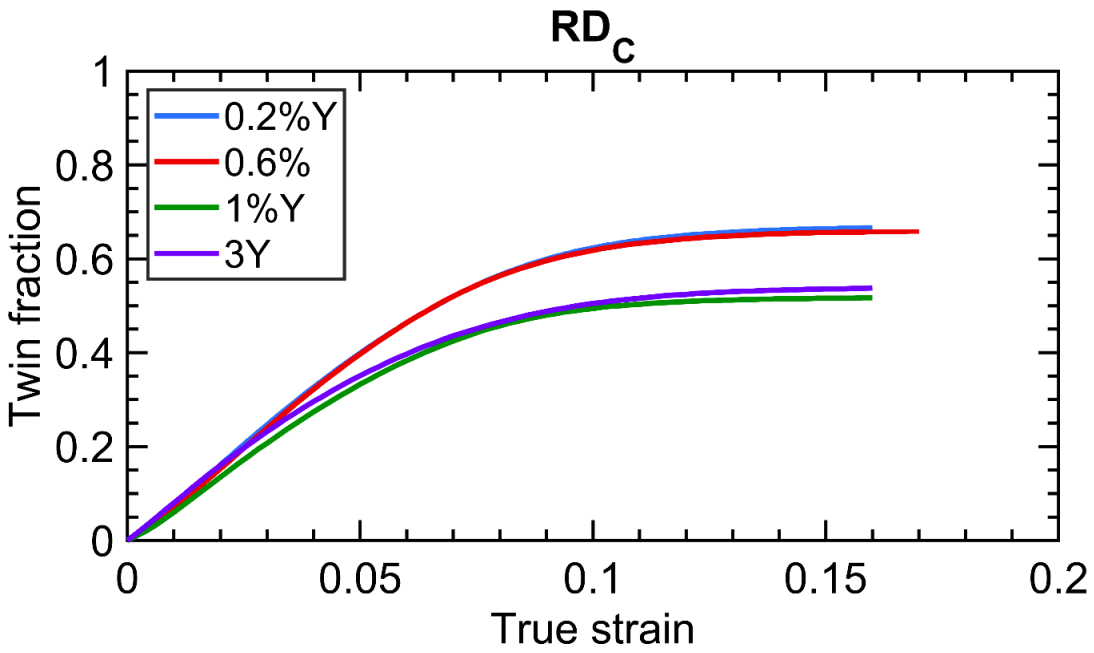

Figure 5-14 Calculated twin volume fractions as a function of RD compressive plastic strain.

The modeling suggests several interesting slip-twin interactions. First, the absorption rate coefficient C in Eq.5-2. for basal, prismatic, and pyramidal slip were the same in all cases. This finding suggests a possible that Y solutes at the twin boundaries does not affect the interactions between dislocations and the twin boundary. Clearly, the growth and

saturation of twinning is affected by Y as the twin volume fraction decreases with increasing amounts of Y additions. Second, the twin-barrier factor $HP^{\alpha\beta}$ for pyramidal slip is found to be 500 with all four Y concentrations, which is much larger than the factor for other two slip modes (basal and prismatic slip). This suggests that the twin boundary serves as a stronger obstacle to pyramidal $\langle \boldsymbol{c}+\boldsymbol{a} \rangle$ slip than the other slip modes. This effect is responsible for the rapid increase in hardening rate during the RD-C test.

5.8 Conclusions

A combination of microstructural characterization, texture analysis, and visco-plastic self-consistent (VPSC) modeling was employed to investigate the alloying effects of different concentrations of Y on the deformation response in Mg. In the experiment, four Mg-Y alloys were deformed along three different loading paths, tension, and compression in the rolling direction (RD-T and RD-C), and compression in the normal direction (ND-C). In the model, the formulation was extended to account for the absorption of lattice dislocations as the twin boundary migrates. For each alloy, the model identified a single set of material parameters that successfully reproduced all measured stress-strain curves and achieved agreement with measured deformation textures and twin area fractions. The following conclusions on the effects of Y alloy concentrations are made:

1. With increased Y concentration, the intensity of the initial basal rolling texture and plastic anisotropy reduced.

2. The effects of Y on yield strength, hardening rate, flow stress are not consistent among the different loading paths. Yield strength increases with Y concentrations only in the RD-C test.
3. The calculations show that the initial CRSS(non-basal)/CRSS(basal) ratio decreases with increased amounts of Y due to an increase in the CRSS for basal slip but relatively little change in the CRSS for pyramidal and prismatic slip with higher concentrations of Y.
4. Despite the lower CRSS(non-basal)/CRSS(basal) ratio, more substantial contributions of $\langle \boldsymbol{c} + \boldsymbol{a} \rangle$ slip and the reduced plastic anisotropy of Mg-Y alloys compared to pure Mg can be attributed to similar initial CRSS values between prismatic slip and pyramidal slip.
5. Increased Y concentration reduces the activity of $\{10\bar{1}2\}\langle\bar{1}011\rangle$ twinning in RD-C.
6. The calculations suggest that migrating twin boundaries in Mg-Y with different concentrations have the same dislocation absorption rate. In addition, the existed twin boundary may act as strong obstacles later in the deformation process.

6 Twin-Twin junctions in Mg

6.1 Motivation

The hardening laws in the critical resolved shear stress for activating slip are clearly important inputs into crystal plasticity-based modeling. In the former two EPSC and VPSC models, the predominant twin system scheme with the composite grain model is applied.

This model for twinning is adequate for most cases; however, as mentioned above, the multiple non-parallel twin variants can be activated and play a unique role compared with one twin variant. Advancing understanding of twin-twin interactions (TTI) between non-parallel twin can help further developing the CP model. Note that in an Mg crystal, the most frequently observed twin type is $\{10\bar{1}2\}$ tensile twin mode, which has six crystallographic equivalent variants. Table 1 presents all six variants of the $\{10\bar{1}2\}$ tensile twin mode for reference.

Table 6-1 twin variants for $\{10\bar{1}2\}$ *twin*

$\{\mathbf{10\bar{1}2}\}$ **Twin**	
$(10\bar{1}2)\langle\bar{1}011\rangle$	T1
$(01\bar{1}2)\langle0\bar{1}11\rangle$	T2
$(\bar{1}102)\langle1\bar{1}01\rangle$	T3
$(\bar{1}012)\langle10\bar{1}1\rangle$	T4
$(0\bar{1}12)\langle01\bar{1}1\rangle$	T5
$(1\bar{1}02)\langle\bar{1}101\rangle$	T6

The former work on twin-twin junctions (TTJs) does not account the effect on relative thickness between the two twins comprising the TTJ. However, it is likely the relative twin thicknesses of the two intersecting twins affect their growth. For instance, would the TTJ

lead to the formation of a new twin if the recipient twin (RT) were thicker? Would the impinging twin (IT) continue to expand after the intersection? In addition, most computational studies of TTJ focus on pure Mg. Considering that alloying Mg can affect the amounts of basal, prismatic, and pyramidal slip activated and material hardening, it is possible that alloying could affect the behavior of TTJs. To answer these questions, the elasto-viscoplastic fast Fourier transform (EVP-FFT) model was employed to study the effect of relative thickness of the two twins forming a $\{1\bar{0}12\}$ co-zone TTJ, meaning the zone axes of the two twins are the same. Furthermore, the effect of plastic anisotropy resulting from alloying additions on the local stress fields produced by the TTJ are also investigated.

6.2 EVP-FFT background

The original FFT-based method was developed to study the local and effective mechanical response of non-linear composite materials (Moulinec and Suquet, 1998). Later, it was adapted by Lebensohn to study polycrystalline materials (Lebensohn, 2001). Over the years, the FFT approach has been extended to apply to many distinct deformation regimes for such materials, such as elasticity (Brenner et al., 2009), incompressible visco-plasticity (Lebensohn et al., 2008), and infinitesimal elasto-visco-plasticity, referred to hereinafter as EVP-FFT (Kanjarla et al., 2012; Kumar et al., 2016). Here, in this thesis study, a formulation of EVP-FFT that further builds into the infinitesimal elasto-visco-plasticity model, the 1) eigenstrain associated with the twinning shear in a twin domain and 2) dislocation-density based hardening. As the integration of last portion is new, the constitutive model and hardening law are first described.

Under an infinite strain approximation, the elasto-visco-plastic constitutive behavior of the materials is written as,

$$\boldsymbol{\sigma}(x) = \boldsymbol{C}(x): \boldsymbol{\varepsilon}^{el}(x) = \boldsymbol{C}(x): (\boldsymbol{\varepsilon}(x) - \boldsymbol{\varepsilon}^{pl}(x) - \boldsymbol{\varepsilon}^{tr}(x)) \qquad 6\text{-}1$$

where $\boldsymbol{\sigma}(x)$, $\boldsymbol{C}(x)$, $\boldsymbol{\varepsilon}^{el}(x)$ are the Cauchy stress tensor, elastic stiffness tensor and elastic strain at a material point x, respectively. In this equation, the elastic strain is the difference between total strain and the sum of the plastic strain $\boldsymbol{\varepsilon}^{pl}(x)$ and transformation strain $\boldsymbol{\varepsilon}^{tr}(x)$. Using an implicit time discretization scheme, the stress tensor at time $t + \Delta t$ is expressed as,

$$\begin{aligned}\boldsymbol{\sigma}^{t+\Delta t}(x) = \ & \boldsymbol{C}(x): (\boldsymbol{\varepsilon}^{t+\Delta t}(x) - \boldsymbol{\varepsilon}^{pl,t}(x) - \dot{\boldsymbol{\varepsilon}}^{pl,t+\Delta t}\ (x, \boldsymbol{\sigma}^{t+\Delta t})\Delta t \\ & - \boldsymbol{\varepsilon}^{tr,t}(x) - \Delta\boldsymbol{\varepsilon}^{tr,t+\Delta t}(x)\end{aligned} \qquad 6\text{-}2$$

where $\dot{\varepsilon}^{pl}$ is the viscoplastic strain rate, and it is assumed to be accommodated by dislocation glide. In turn, the $\dot{\varepsilon}^{pl}$ is constitutively related with the stress at material point x through the summation of N active slip systems, of the form:

$$\dot{\boldsymbol{\varepsilon}}^{\mathrm{pl}}(\mathrm{x}) = \dot{\gamma}_0 \sum_{\mathrm{s}=1}^{\mathrm{N}} \mathbf{m}^{\mathrm{s}}(\mathrm{x}) \left| \frac{\mathbf{m}^{\mathrm{s}}: \boldsymbol{\sigma}}{\tau_{\mathrm{c}}^{\mathrm{s}}(\dot{\varepsilon}, \mathrm{T})} \right|^{\mathrm{n}} \mathrm{sign}(\mathbf{m}^{\mathrm{s}}: \boldsymbol{\sigma}) \qquad 6\text{-}3$$

where $\tau_{\mathrm{c}}^{\mathrm{s}}$ is the critical resolved shear stress. A dislocation density based hardening scheme is used to evolve $\tau_{\mathrm{c}}^{\mathrm{s}}$ with strain as a function of the imposed strain rate $\dot{\varepsilon}$ and temperature T. The term $\mathbf{m}^{\mathbf{s}}(\mathbf{m}^{\mathbf{s}} = 0.5\ (\mathbf{b}^{\mathbf{s}} \otimes \mathbf{n}^{\mathbf{s}} + \mathbf{n}^{\mathbf{s}}\mathbf{b}^{\mathbf{s}}))$ is the symmetric part of the Schmid tensor, where $\boldsymbol{b}^{\boldsymbol{s}}, \boldsymbol{n}^{\boldsymbol{s}}$ are two orthonormal unit vectors representing the slip direction and slip plane normal, respectively. The rate $\dot{\gamma}_0$ is a normalization factor and n is the rate-sensitivity exponent.

The twinning transformation strain within the explicit twin domain is imposed via successive increments using:

$$\Delta\varepsilon^{tr}(x) = \boldsymbol{m}^{tw}\Delta\gamma^{tw}(x) = \mathbf{m}^{tw}\frac{s^{tw}}{N^{twincr}} \qquad 6\text{-}4$$

where $\boldsymbol{m}^{tw}$ is the Schmid tensor associated with the explicitly simulated twin system, s^{tw} and N^{twincr} are the characteristic twinning shear and number of increments, respectively.

The hardening effect of dislocation is governed by the dislocation density law, which is presented in the background section, thus it is not repeat here. The pseudo-slip twin model is also applied to indicate material points where twinning is more likely than slip to occur. The pseudo-slip twin model relates the twinning shear rate to the resolved shear stress and a critical resolved shear stress using the same flow rule, Eq.6-3, as for slip. When the voxels start transforming from the matrix domain to an explicit twin domain, the pseudo-slip twin model is no longer used. The pseudo-slip twin model tests for twin formation only in the matrix and not in explicit twin domains.

6.3 Materials system and the associated parameters

In this work, Mg-4Li and AZ31 Mg alloys are considered along with pure Mg (PMg). The chemical compositions of the considered alloy systems are listed in Table 2. The effect of alloying elements on the lattice parameters and elastic constants most likely small and not known for the considered alloys systems. Thus, the lattice parameter and anisotropic elastic constants are assumed to be the same and equal to that of pure Mg i.e, c/a=1.624 and $C_{11} = 59.5GPa$; $C_{12} = 26.1GPa$; $C_{13} = 21.8GPa$; $C_{33} = 65.6GPa$; ;$C_{44} = 16.3GPa$. (Ganeshan et al., 2009; Simmons and Wang, 1971). The CRSS values for the slip

modes differ among the Mg alloys considered here. The initial CRSS and the associated hardening parameters for these alloys are found in (Beyerlein et al., 2011), (Lentz et al., 2015a), (Ardeljan et al., 2016). These same parameters are employed here since they were all obtained by a crystal plasticity model simulation scheme employing the same flow rule and dislocation density hardening law used here.

To quantify the effect of alloying addition on plasticity, the following plastic anisotropy (PA) measure from (Kumar et al., 2017b) are adapted

$$PA = \frac{\tau_0^{Pr} - \tau_0^{Ba}}{\tau_0^{TT} - \tau_0^{Ba}} \qquad 6\text{-}5$$

As a slight modification, the average instantaneous CRSS (see Figure 6-1) at 0.5% strain before twinning is used to calculate the PA for studied alloys (see). The twin is inserted at 0.5% strain since the TRSS for this twin in crystal rises sufficiently above the CRSS for twinning. Note that this PA measure assumes that the basal slip system is the easiest slip mode in magnesium alloys. With this notion, AZ31 being the most and MgLi the least anisotropic. Pure Mg falls in between these two alloys. This PA measure will be used to determine how this microscopic-level anisotropy in the slip modes affects the local micromechanical fields induced by TTIs and its role on further twin network structure formation.

Table 6-2 Chemical composition of studied Mg alloy and correspond CRSS with PA ratio

Mg alloys	composition (wt%)			CRSS at 0.5% strain before twinning [MPa]				PA	Ref.
	Al	Zn	Li	Basal	Prismatic	Pyramidal	T. Twin		
MgLi	-	-	4.0	5.5	17.1	53	25	0.59	(Lentz et al., 2015a)
PMg	-	-	-	3.85	36.2	87.2	11	4.52	(Beyerlein et al., 2011)
AZ31	3.0	1.0	-	12.1	47.3	158	13	39.35	(Ardeljan et al., 2016)

6.4 Simulation procedures

The EVP-FFT model setup for TTJ simulations is shown in Figure 6-1. The unit cell is periodic in all three directions and consists of a parent matrix grain (light blue) containing the TTJ and the surrounding buffer layer (dark blue). The unit cell is discretized into 3 x 500 x 500 voxels with 40 voxels thick buffer layer. The crystal orientation of each voxel in the buffer layer is randomly assigned. The crystallographic orientation of matrix grain is taken as (0°,0°,0°) in Bunge convention, which aligns the Y and Z axes with the $[01\bar{1}0]$ and

$[0001]$ directions of the matrix grain. The voxels with red and orange color designate explicit twins of variant T2-$(01\bar{1}2)[0\bar{1}11]$ and T5-$(01\bar{1}2)[0\bar{1}11]$, respectively. They are referred as the recipient twin (RT) and impinging twin (IT). The twinning plane normal and shear direction of both twins are in YZ plane. There is no out-of-plane twin shear in XY and XZ planes. Because of this, a 2D columnar microstructure is considered.

The unit cell is subjected to a compression strain of 0.5% along the Y direction, while applying stress-free boundary conditions in the Z and X faces. This imposed stress state corresponds to a Schmid factor of nearly 0.5 for both twin variants. After a compression to 0.5% strain, first the RT is introduced in the preselected domain by reorienting the crystal following the twinning relationship and imposing the characteristic twinning shear of 12.9% over 1000 numerical steps at a fixed macroscopic boundary condition. Then, the IT is formed at the same macroscopic loading. In all stages of simulation, plastic deformation is accommodated by basal <a>, prismatic <a> and pyramidal <c+a> slip along with $\{10\bar{1}2\}$ tensile twin as a pseudo-slip. But, within the twin domain, only the dislocation slip modes are made available, not the pseudo-slip twin mode, after introducing the twins.

EVP-FFT simulations with different twin thicknesses are performed to understand the effect of relative twin sizes on twin-twin interactions. Accordingly, two sets of simulations are considered: (1) recipient twin thickness (RT_t) is varied while for a fixed impinging twin thickness (IT_t =12 voxels), i.e., RT_t/ IT_t=1, 2, 3, 4; (ii) impinging twin thickness (IT_t) is varied while for a fixed recipient twin thickness ($RT_t = 12$ voxels), i.e., IT_t/ RT_t=1, 2, 3,

4. These TTJ simulations are performed for MgLi, PMg, and AZ31 material systems to investigate alloying effect.

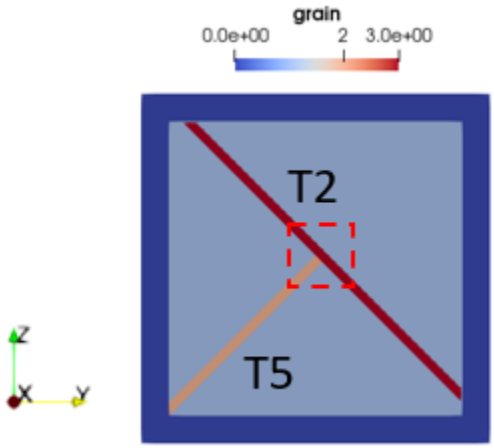

Figure 6-1 Schematic diagram of the simulation unit cell with two tensile twin (T2 and T5). T2 (red) is the recipent twin and T5 is the impinging twin. The orientation of parent grain (light blue) is (0°,0°,0°) i.e c-axis parallel to Z-direction. Simulation with different relative twin thickness were performed include RT_t/IT_t*=1, 2, 3, 4 and* IT_t/RT_t*=1,2, 3, 4. The CRSS in the red rectangle was used to calculate the instantaneous PA ratio.*

6.5 Results

The EVP-FFT model computes the full stress and strain tensors, and therefore the stress components acting on the twin interface can be determined. Here, twin plane resolved shear stress (TRSS) is calculated to infer the driving force for twin growth. The TRSS could drive the glide of twinning dislocations on the twin boundary, thus leading to the twin boundary migration (Christian and Mahajan, 1995; Ostapovets and Serra, 2014; Wang et al., 2013). In the following, TRSS5 represents the TRSS along the twinning direction of twin variant 5, which is the same as the IT. The same applies to other variants. The TRSS along

the two boundary of IT (white line in Figure 6-2 (c)) and RT (green line in Figure 6-2 (c)) are analyzed to investigated possible twin growth and nucleation behavior near TTJ. In the TRSS profile plots below, all TRSS is normalized by the CRSS for twin formation and the distance is normalized by the fixed twin thickness. TRSS profiles for V1 and V4 are the same as V3 and V6 respectively; thus, they cannot be view in the plot. In this section, AZ31 is used as an example, before presenting the other materials to elucidate the effect of alloying.

6.5.1 Effect of recipient twin thickness

To study the role of RT thickness on twin-twin interactions, at first, the effect of RT_t on IT growth was researched. The TRSS5 along the IT (T5) boundary is calculated for different RT_t's (indicated by the white line in Figure 6-2 (c)). The TRSS5 profile for AZ31 is shown in Figure 6-2 (a,b). In addition, TRSS5 when IT is presented alone in the crystal is plotted for comparison (i.e., RT_t=0). The TRSS curves show that all TRSS5 are negative and tend to arrest twin thickening. The existence of RT causes some variation of the TRSS5 along IT twin boundary, although the change is relatively small. The TRSS5 along IT top boundary does not change with the RT_t while the TRSS5 along IT bottom boundary has a very small decrement as RT_t increase. The results, thus, suggest that the thickness of the RT does not affect the growth of the IT after impingement.

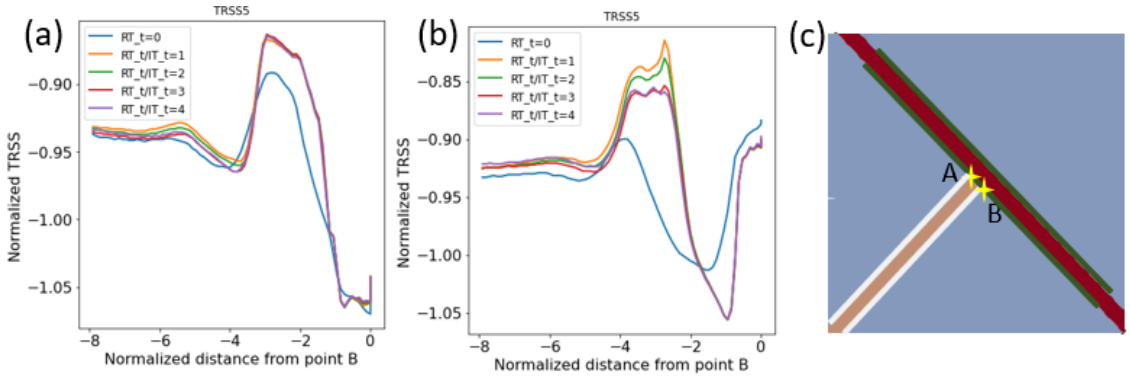

Figure 6-2 Normalized TRSS5 along the (a) top and (b) bottom boundary of IT in AZ31 makred in (c).

Then the TRSS profile along the RT boundaries are considered. In the RT bottom boundary, the TRSS profile does not promote the RT boundary migration when the $RT_t/IT_t \geq 2$ and it does not show a clear relationship between RT_t. Therefore, the results are not presented here. The TTJ configuration with RT_t/IT_t=1 is special, but since this case is also included in the simulations with IT_t increase, it will be discussed systemically in next section.

Figure 6-3 (a~b) show the TRSS along the top boundary of RT when only introdcuing RT, whereas figure 6-3 (d~f) show these TRSS profiles after introducing IT. When RT_t/IT_t=1, the highest TRSS values are TRSS2 and TRSS5 between C and D (see figure 6-3 (d)), indicating that the two mechanisms may happen in this region, i.e., the growth of RT and nucleation of a new twin with the same variant as the IT. Another question that remains is how does the RT_t thickness affect these two mechanisms. It is intuitive to think that higher RT_t will reduce the TRSS2 and TRSS5, thus suppress the growth and nucleation. The figures in the last two column in figure 6-3 show the simultion with

increasing RT_t. Apparently, the change of TRSS caused by IT is minimized (as shown in figure 6-3 e,f) and the highest TRSS become the non-co-zone variant, V3 and V6. The TRSS2 and TRSS5 values between C and D decay rapidly with increases in RT thickness. In figure 6-3 (e), where RT_t/IT_t =2, the TRSS2 and TRSS5 have already beome negative, which suggests that the growth of RT and apparent acrossing is unlikely to happen.

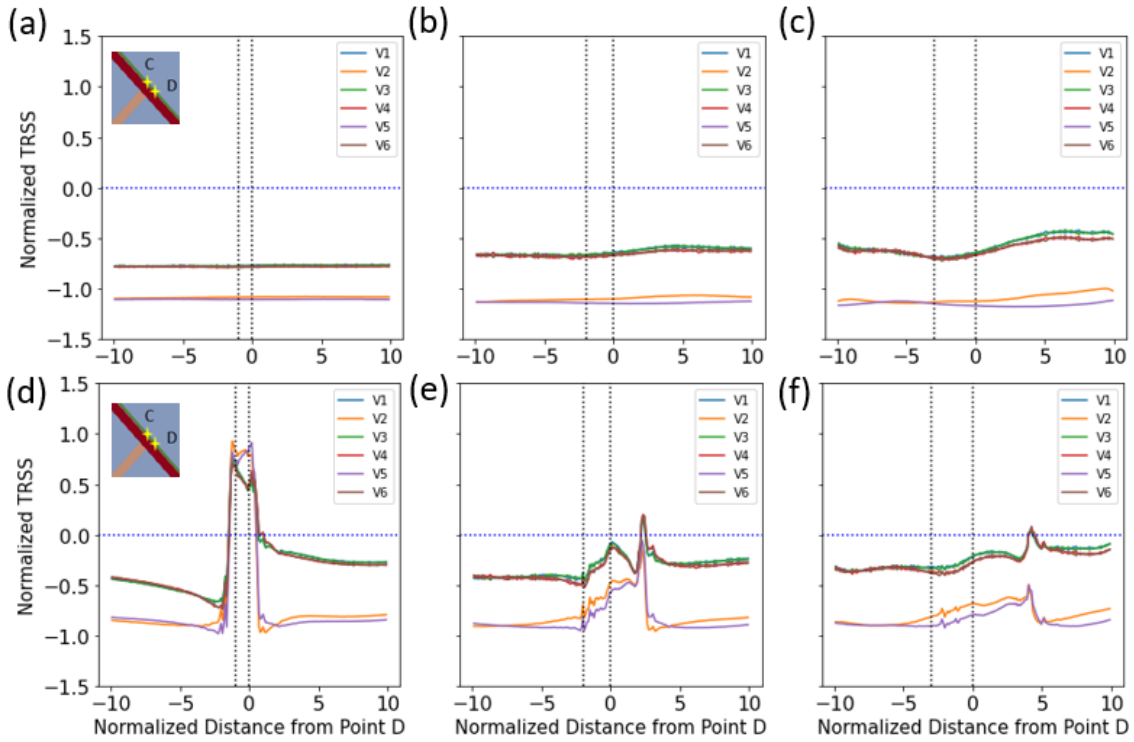

Figure 6-3 Normalized TRSS profile along RT Top boundary before (a~c) and after (d~f) forming the TTJ in AZ31. (a,d),(b,e),(c,f) correspond to RT_t/IT_t=1, RT_t/IT_t=2, RT_t/IT_t=3.

6.5.2 Effect of impinging twin thickness

In this section, the TRSS profiles along twin boundary are calculated as IT_t increases. The TRSS profile along IT boundary was studied first. The TRSS remains negative in all cases

and has the same patterns as the case $IT_t/\ RT_t = 1$. Therefore, the growth of IT is clearly not favored in this TTJ and this result is not discussed further.

Next, the driving forces along the RT boundary are studied. The stress state along the RT interface is much more complicated than that along the IT interface and accordingly the TRSS for all twin variants are worthy of further analysis. Figure 6-4 shows the TRSS profile along the RT bottom boundary (indicated by the green line in Figure 6-4 (a)). Figure 6-4 (a) corresponds to the case without the IT (IT_t=0). Figure 6-4 (b) corresponds to the case $IT_t/\ RT_t$=1, and Figure 6-4 (c) corresponds to $IT_t/\ RT_t$=4. As shown, the TRSS increases as IT_t increases. This suggests the backstress associated with the RT is relaxed due to the TTJ structure. Among these six twin variants, the TRSS2 and TRSS5 have the highest values, and in certain regions, they become positive. Thus, the growth of RT or the nucleation of twin variant 5 may happen with little or no additional macroscopic loading. In the plot, TRSS5 has a higher value than TRSS2, which suggests the formation of twin variant 5 is more likely compared to the growth of the RT. Figure 6-5 is a TEM image reported by Yu et al. (2014a). This experimental observation shows some tiny twins parallel to the IT next to the TTJ (indicated by the red circle in Figure 6-5). According to the TRSS analysis, the TTJ structure could have directly caused these smaller twins to form.

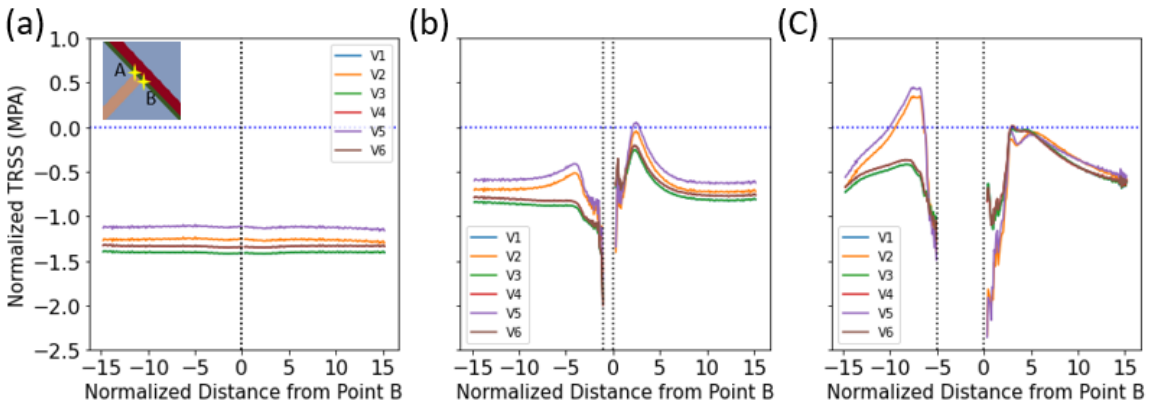

Figure 6-4 Normalized TRSS profile AZ31 along the RT bottom boundary, (a) IT_t=0, (b) IT_t/ RT_t=1 , (c) IT_t/ RT_t=4. The region between gray dot line represents the region AB

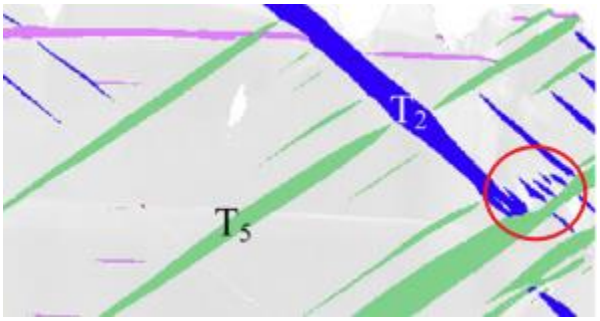

Figure 6-5 TEM image of Mg. This image is taken with permission from Yu et al. (2014a)

The TRSS along the other side of the RT boundary is also studied. Figure 6-6 shows the TRSS profile of AZ31 along the RT top boundary (indicated in figure 6-6 (a)) as IT_t increase. Figure 6-6 (a) is the TRSS profile before the IT has formed, and figure 6-6 (b~e) corresponds to the TRSS after the TTJ has formed. All cases show that highest TRSS5 value occurs between C and D. One thing that needs to be pointed out is that TRSS2 is also very high between C and D. In fact, it seems more likely that a new twin of variant 5 will form, while in the other half of CD, the growth of RT (variant 2) will be more favorable. In addition, by increasing the IT_t further, the TRSS for the other twin variants becomes

positive on the right of point D. But the formation of non-co-zone twin is unlikely to happen because the available stress for RT growth (TRSS2) or apparent crossing (TRSS5) is much higher. Thus, these two mechanisms may happen first, which would then be followed by relaxation of the stress state in this region. On the other hand, the large IT_t TTJ configuration, such as $IT_t/RT_t = 3{,}4$, may not be common in the actual situation. This is due to two reasons. First, the twin thickening process usually happens after the twin tip reaches the opposing grain boundaries or defects. Second, the current study shows that the thickening of IT is unfavored when it reaches the RT interface. Therefore, the TTJ structure does not promote the automatic formation of a non-co-zone twin variant at the top boundary of the RT.

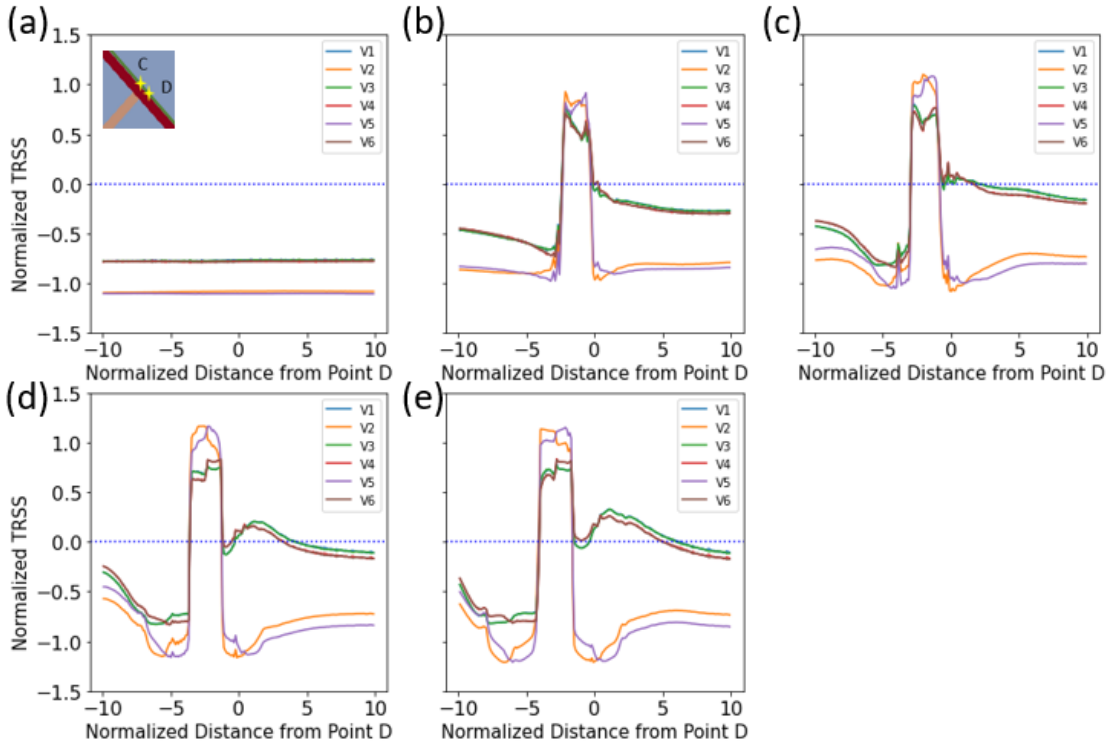

Figure 6-6 Normalized TRSS along the RT top boundary in AZ31, (a) IT_t=0, (b) IT_t/ RT_t=1, (c) IT_t/ RT_t=2, (d)IT_t/ RT_t=3, (e) IT_t/ RT_t=4.

6.5.3 The effect of alloy additions

The effect of alloy additions is investigated using the PA measure described in Eq.6-5. For Mg and its alloys, the easiest deformation mode is basal slip, while the second easiest deformation mode could be either prismatic slip or tensile twinning. The PA measure quantifies the difficulty of twinning in Mg alloy. If PA measure is small, it represents that the alloying addition hampers twinning, thus reduces plastic anisotropy. As shown in Table 6-2, MgLi and PMg have a lower PA ratio compared with AZ31. Studying these materials can help understand how the alloying element affects the twinning mechanism presented above.

First, the cases that IT_t is fixed and RT_t is varied are considered. The TRSS5 profiles along the IT boundary with different RT_t are calculated. It does not show an apparent difference between AZ31 and the other two alloys, although the magnitude is different. Therefore, the plot is not presented here. The finding that RT thickening is not affected by the RT_t is also true for lower PA ratio Mg Alloys. The TRSS5 profiles along RT top boundary in PMg and MgLi also indicate that thicker RT will impede the apparent crossing mechanism (shown in figure 6-7). In figure 6-7 (b), since the peak TRSS5 values in PMg and MgLi are close to zero, albeit still positive, the crossing mechanism may be unlikely to happen. This suggests that RT_t/ IT_t=2 may be a critical thickness ratio for apparent crossing.

Second, the alloy addition affects the TRSS profile with fixed RT_t and different IT_t is studied. figure 6-8 shows the TRSS profile along the RT bottom twin boundary of PMg and MgLi. The observation is similar in that the TRSS increases as IT_t increases. However, PA decreases, the increment in the co-zone variant TRSS reduces, while the increment in that of the non-co-zone variant increases. In MgLi, the highest TRSS on the two sides of points A and B are TRSS6 and TRSS3 (figure 6-8 (e)), indicating that the formation of a non-co-zone twin is favored near the bottom boundary of RT.

Analyzing the TRSS profile in Figure 6-6 shows that the TRSS of the co-zone variants (V2 and V5) and non-co-zone variants (V1,3,4,6) become dominant in different regions of the TTJ. TRSS5 and TRSS3 are selected for the following analysis since they are two representative variants in co-zone variant and non-co-zone variant, respectively. To reveal the effect of alloying, the TRSS3 and TRSS5, among different materials, are plotted in Figure 6-9. In Figure 6-9(a), marked by a red rectangle, the TRSS3 on the red of point D positively correlates with the PA ratio, while the TRSS5 between C and D (marked by a red rectangle in Figure 6-9 (b)) appears to be uncorrelated with the PA ratio.

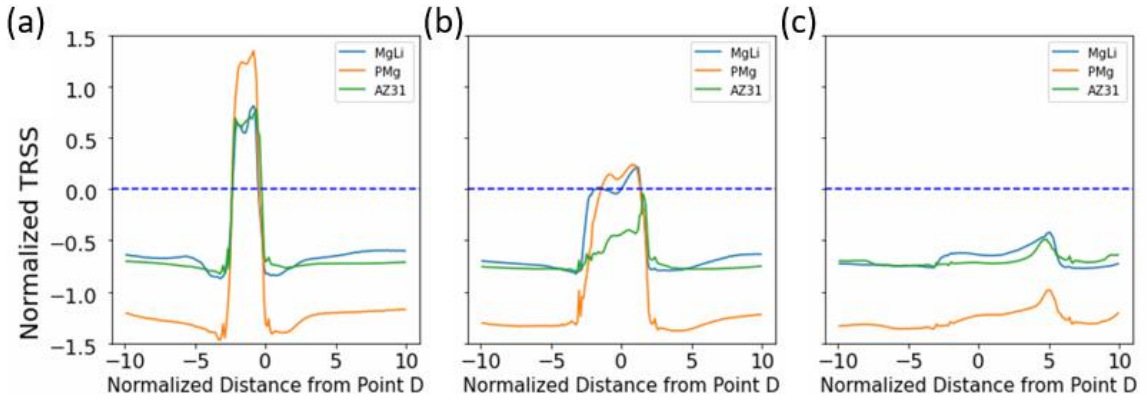

Figure 6-7 Normalized TRSS profile along RT top boundary of three Mg alloys with RT thickening (a) RT_t/IT_t=1, (b) RT_t/IT_t=2, (c) RT_t/IT_t=3, The distance is normalized with respect to IT_t

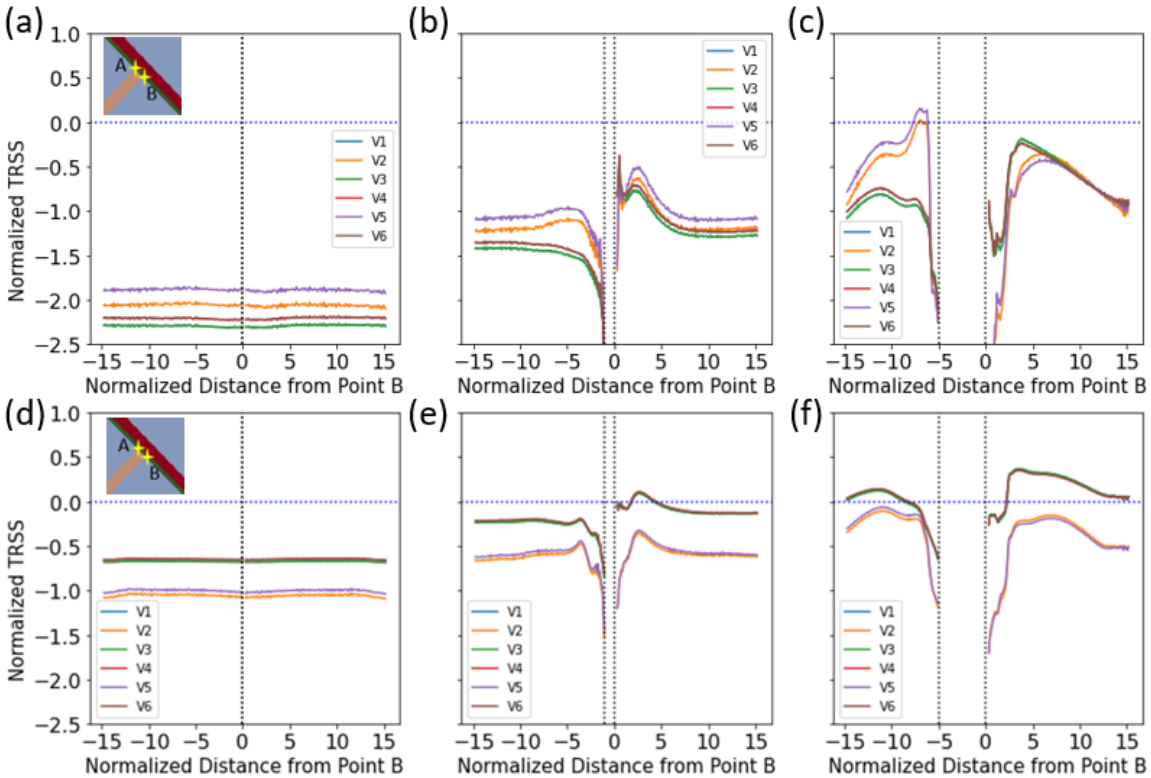

Figure 6-8 Normalized TRSS along the RT bottom boundary. (a~c) PMg with (a) IT_t =0, (b) IT_t/RT_t=1, (c) IT_t/RT_t=4; (d~f) MgLi with (a) IT_t=0, (b) IT_t/RT_t=1, (c) IT_t/RT_t=4. The region between gray dot line represents the region AB

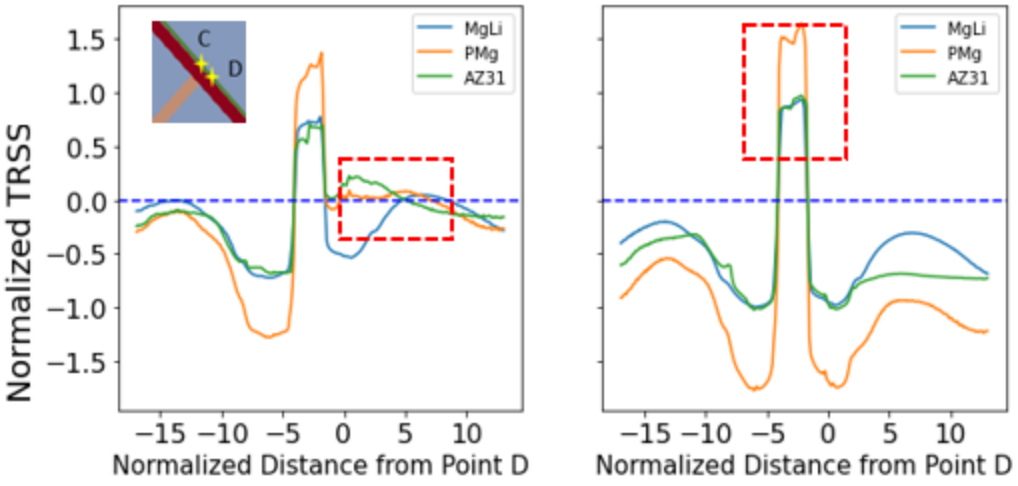

Figure 6-9 Normalized TRSS profile along the RT top boundary among different materials with IT_t/RT_t=4 (a) TRSS3. (b) TRSS5. The distance is normalized with respect to RT_t

6.6 Discussion

Both this study and previous studies (El Kadiri et al., 2013; Juan et al., 2015) have drawn a connection between the formation of numerous fine twin lamellae and multiple TTJs. Based on the current calculations, the stress fields around TTJ show that TTJs would favor new twin formation with the same twin variant as the IT on the other side of the RT. The TTJ does not fully support the expansion of the intersecting twins along their entire length but rather promotes their expansion in the vicinity of TTJ. This local expansion has been observed in experiment. Sun et al. (2015b) investigated the co-zone TTJ in AZ31 using TEM and find the asymmetry growth of RT in the interface close to IT tip. Yu et al (2014b) also

observed a similar structure in a pure Mg single crystal. The reduction in the average twin propagation rate when TTJs appear in grain could be explained by the re-nucleation being more favored. Kadiri et al. (2013) compared the twin nucleation and twin growth in two grains with one grain containing a single twin variant and the other containing two co-zone twin variants. The interesting finding in their study is that the twin volume fraction is nearly equivalent and suggests the amount of strain accommodated by the twinning is almost the same (El Kadiri et al., 2013). Thus, in the presence of TTJs, the twin thickening rate is lowered, and formation of new twins favored. For a propagating twin, the twin boundary of RT, could act as an obstacle making the formation of other parallel twins favored. This would imply that the likely result would have more TTJs and hence more twin boundaries. The expansion of the TTJ twins appears to be only limited in a small region along the twin boundary.

Regarding new twin formation, among the other five variants, the co-zone variant twin has the highest TRSS and thus is favored in all possible TTJ twin thicknesses. In contrast, the nucleation of a non-co-zone variant is more likely to happen in some cases when the IT_t is much larger than RT_t. In the following discussion, nucleation of a co-zone twin variant will be the main emphasis.

An alternate method is proposed to measure new twin formation. Since the pseudo slip twin model is included in simulation, the contribution to shear of each twin system s, $\Delta\gamma^s$, in each voxel can be tracked. This quantity has been widely used in the mean-field crystal plasticity models to simulate twinning either using predominant twin reorientation (PTR) or volume transfer scheme. (Beyerlein and Tomé, 2008; Knezevic et al., 2015; Proust et

al., 2007). Following this concept, the accumulated normalized twin shear (ANTS) is used as an indicator for twin nucleation, and it is defined as,

$$ANTS^s = \Delta\gamma^s/S$$

where *S* is the characteristic twinning shear. It is worth noting that the ANTS is used as an indicator for twin nucleation, while in the mean-field scheme, $\Delta\gamma^s/S$ is frequently used for calculating twin volume fraction. The average $ANTS^5$ in the region, Ω (shown in Figure 6-10 (a)) is plotted in Figure 6-10. Figure 6-10 (a~c) corresponds to the cases in which the RT_t varies and IT_t is fixed, while Figure 6-10 (d~f) corresponds to the cases in which the IT_t varies and RT_t is fixed. The first column and second column in Figure 6-10 shows the $ANTS^5$ when only RT has formed before IT twinning and with both the RT and IT have formed, respectively. The last column shows the change in $ANTS^5$ between these two cases.

In the current study, if the change in $ANTS^5$ is larger than 5%, the new twin can form in this region without further loading, a phenomenon was referred to as "auto-twinning". In this case, with only the RT in the grain, the $ANTS^5$ is negative indicating that the twin nucleation of V5 is unlikely happen. With increasing RT_t, more backstress is generated by the RT and thus it becomes more difficult for V5 nucleation. Figure 6-10 (c) show the change in $ANTS^5$ caused by the IT is negligible when $RT_t/IT_t \geq 1$. More generally, Figure 6-10 (f) shows that the IT only plays an important role on V5 nucleation when $IT_t/RT_t > 2$ (or $RT_t/IT_t < 0.5$). In this case, the IT_t/RT_t ratio lies above 2, the ANTS5 in Ω seems to be more sensitive to the IT_t, and AZ31 has the highest sensitivity to IT_t increases. Auto-

twinning can happen when $IT_t/\ RT_t$ is larger than 2 in AZ31, while the other two alloys require $IT_t/\ RT_t$ to be larger than 3. This indicates that the high PA alloy favors twin nucleation in this region more so than the low PA alloy. But $IT_t/\ RT_t$>2 may not be frequently observed, which would mean situations favoring auto-twinning may not happen. But with further loading in the same direction, the nucleation of co-zone twin could occur within this area.

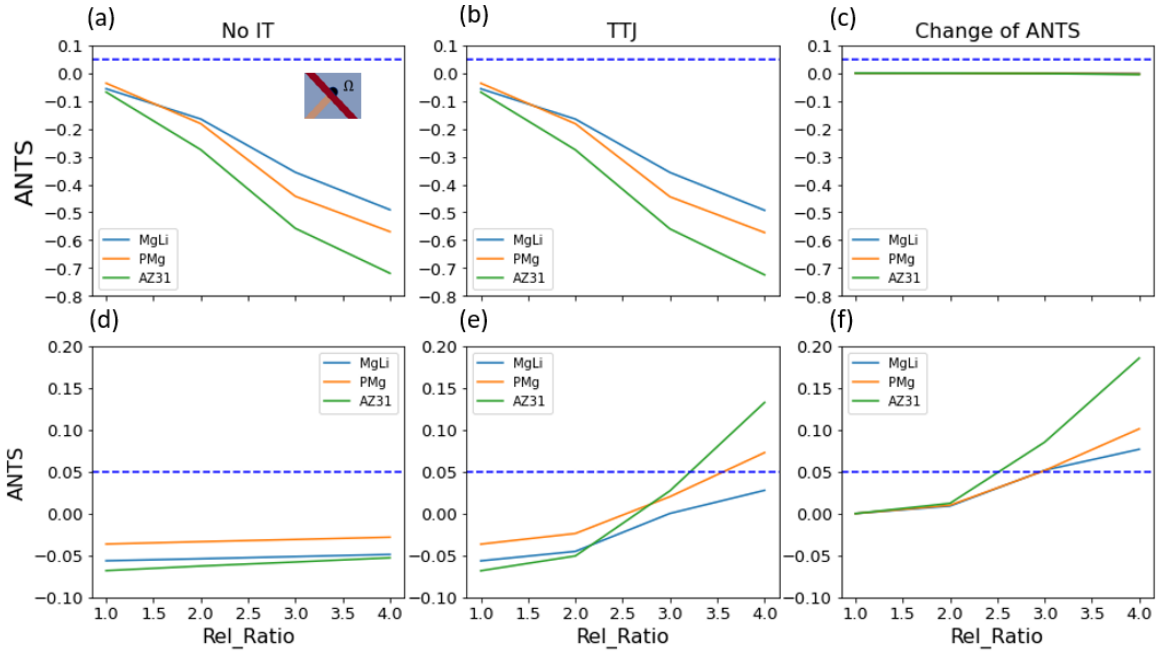

Figure 6-10 ANTS in region Ω. (a~c) RT thickening, the Rel_ratio is calculated by $RT_t/\ IT_t$; (d~f) IT thickening, the Rel_ratio is calculated by $IT_t/\ RT_t$. (a,d),(b,e),(c,f) correspond to the case only RT in the grain, both IT and RT formed in the grain, the change of ANTS between these two cases, respectively

Another question that arises is how the TTJs affect the hardening behavior of material. Yu et al., (2011) performed a fully reversed tension-compression cyclic test on Mg single

crystal along [0001] direction to 0.5%. With an increase in loading cycles, the yield strength of Mg increased. The reason was attributed to the extensive twinning and the residual twins that remained after the loading cycle since their twin boundaries would act as an obstacle to dislocation motion. In their study, many TTJs are also observed. To unravel the hardening effect due to TTJ, here another simulation was conducted with only a single twin inside the crystal for all alloys, in which the loading condition is the same. The total volume fraction is the same as the crystal containing TTJ with IT_t/RT_t=1. The strain-stress response of MgLi and AZ31 is present here for analysis (see figure 6-11). The result indicates that the TTJ causes even less macroscopic hardening compared with the single twin. A possible explanation is that the TTJ structure prefers twinning; thus, most of the deformation in the crystal is accommodated by pseudo-slip twinning.

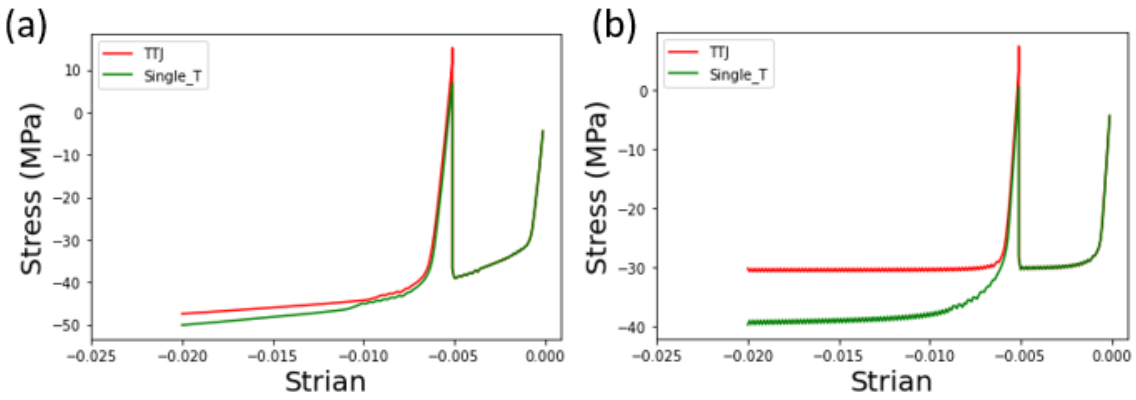

Figure 6-11 Macroscopic strain-stress response of single crystal under compression along $[01\bar{1}0]$ direction (a) MgLi, (b)AZ31

Last, the dislocation activity around the TTJ is investigated. In this model, the instantaneous CRSS is updated as the dislocation density evolves. In AZ31 simulation, the dislocation activity is negligible since most of the deformation is accommodated by the

pseudo-slip twinning. This dislocation density field is similar between MgLi and PMg. Thus, the PMg is used as an example for illustration.

The hardening effect on prismatic slip and pyramidal slip caused by the TTJ is negligible. Note this should not be interpreted as contrary to the observation that a significant amount of pyramidal dislocation exists around twin or TTJ (Agnew et al., 2001; Yoo, 1981). Rather it is a consequence of including the pseudo-slip twinning model in the simulation, as pseudo-slip twinning also accommodates the deformation along c direction, and its CRSS is much lower than that for pyramidal slip. Figure 6-12 (a) shows the CRSS field of basal dislocation in PMg for $IT_t/RT_t = 1$. As shown, the CRSS in the corner of the TTJ and on the other side of T2 increases, and CRSS in the region above CD does not increase much, thus producing a butterfly pattern. Comparing the TRSS profiles shows that these areas have negative TRSS, which suggests that twinning activity in this region is unfavored during deformation. The CRSS field here identifies predominant basal slip in these areas. In the twin domain, the CRSS increment is mainly due to the explicit twin transformation, but the IT also caused a higher hardening rate on basal slip near the region where the two twins intersect. This dislocation activity shown here is consistent with the experimental observation that a basal slip band is found near the TTJ (Yu et al., 2014b). In region Ω, the hardening effect on basal slip is small. Instead, the local strain in this region acts primarily in tension along the c direction, favoring tensile twinning in this location.

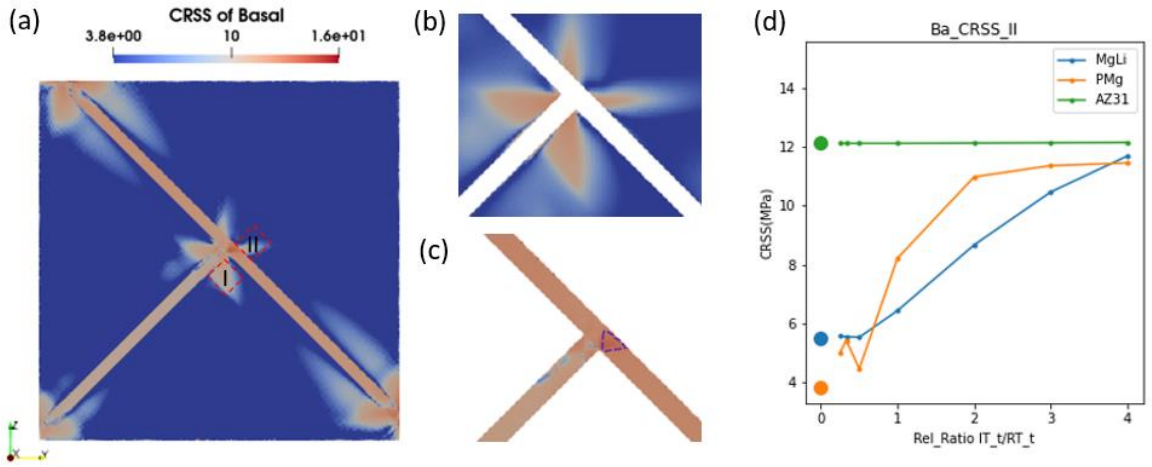

Figure 6-12 Basal CRSS field of PMg (a) whole unit cell, (b)Matrix domain,(c) Twin domain (d) Average CRSS in region II for all three alloys.

Figure 6-12 (d) shows the average CRSS in region-II for basal slip with different twin thicknesses. The average CRSS in the severe hardening region (region I and region II in figure 6-12) was used to investigate how hardening changes with respect to the thickness ratio IT_t/RT_t. In region I, the CRSS value does not show a clear relationship with the thickness ratio and thus is not discussed further. In region II, when IT_t/RT_t larger than 1, the CRSS increase with increasing IT_t, as shown in figure 6-12 (d). The simulation with the single twin variant shows that the increment in CRSS in region II is primarily due to the stress enhancements at the IT tip. Therefore, it can be expected that a thicker IT will cause more hardening in the other side of twin. When the IT_t/RT_t is less than 1, the CRSS shows some variation. It is likely that when the thickness of RT_t becomes larger than IT_t, the effect of IT on the other side of RT decays rapidly with increasing RT_t, and soon becomes negligible. This is supported by the observation that CRSS in region II before IT forms is

very close to the CRSS when IT_t/RT_t <=0.5. It also indicates that the impinging twin will create greater local hardening than that with just a single twin.

6.7 Conclusions

In the current study, the Elasto-Visco-Plastic Fast Fourier Transform model was employed to investigate the interaction between two co-zone twins. TTJs with different relative twin thickness between impinging twin and recipient twin were considered. Simulations were performed on three different Mg alloys with different degrees of plastic anisotropy. The TRSS field was calculated to analyze the twin growth and nucleation behavior. It is found that the TTJ promotes the local thickening of the recipient twin and new twin nucleation. It is shown that increasing the recipient twin thickness RT_t does not affect the impinging twin growth, while increasing the impinging twin thickness IT_t will promote new twin formation and lead to apparent crossing structure. The formation of a non-co-zone variant from the TTJ is unfavored in most cases. In addition, the normalized twin shear was used to analyze the apparent crossing mechanism. The result shows that formation of a new twin on the other side of RT due to the TTJ structure is not automatic and additional loading is required even though the stress favors the apparent crossing. The alloy addition does not strongly affect twin growth and apparent crossing mechanism, but the non-co-zone twin nucleation is more likely to happen in the lower PA alloy.

7 Conclusions

HCP metals and their alloys are desired in many industries due to their excellent properties. Two types of metallic materials, CP-Ti and Mg alloys were studied in this thesis. The application of these materials suffers from the insufficient availability of easy slip modes. Therefore, various twinning mechanisms are activated depending on the material type and loading conditions. The interactions of twins with other type of defects, as well as twinning itself, significantly increase the complexity in the plastic behavior of HCP metals. In the current thesis research, three types of crystal plasticity (CP) based models were applied to research the twin-related hardening mechanisms in Ti and Mg alloys. The attraction of CP-based models lies in their ability to predict the material macroscopic response and microstructure evolution in any loading condition. Much data can be obtained through the simulation, including the texture evolution, slip activity, twin volume fraction. Taking advantage of these capabilities, the CP formulation has been used as an important tool to help analyze polycrystalline plastic behavior and interpret experimental observations and measurements.

In the first work, the elasto-plastic self-consistent model was used to simulate the deformation behavior of CP-Ti under cyclic loading. The main objective is to research twinning and detwinning behavior. Three major slip systems with two twin systems were considered for simulation. In cyclic loading, a phenomenon called Bauschinger effect is always observed. To predict this effect well, a slip-system level backstress is incorporated

into the model. Validation was carried out with the help of the forward-reverse data reported in (Hama et al., 2015), which included stress-strain curves and deformation textures. A single set of hardening parameters is characterized for the model that enables model results to agree with the data sets. From this, the set identifies that prismatic slip has the lowest CRSS while the pyramidal has the highest CRSS. The CRSS values for contraction twin and extension twin propagation indicate that twin propagation is more difficult than dislocation glide. Predictions of slip activities show that prismatic slip dominates plasticity in all strain levels and the relative amounts of slip activity do not change throughout the loading cycle. Pyramidal slip is found to develop the highest backstress. To elucidate how the backstress developed by pyramidal slip influences twinning behavior, a new set of parameters were characterized, without the backstress term included. Predictions of cyclic loading was compared with the original prediction with backstress. The comparison shows that the backstress developed by pyramidal slip favor deformation twinning in forward loading and suppressed twinning in reverse loading.

The next investigation into dislocation-twin interactions concerned another HCP material, the Mg-Y alloy. This alloy was selected because experimental reports consistently find that only {10-12} extension twinning occurs in this alloy, and therefore can serve as a model system for simulation. Another reason is because the sigmoidal shape stress-strain curve of Mg-Y in RD compression indicates that even more twinning occurs under similar conditions than the CP-Ti. In this study, four concentrations of Y in Mg-Y were studied to understand the effects of Y on twinning. It is found that before deformation that the initial

texture depends on Y concentration, an effect that can be taken into account in the VPSC calculation. Some initial studies showed that the initial texture changed the amount of twinning activity with all else being the same, such as the same loading path. In the experiment, the alloys were deformed along three loading directions with respect to the sheet, which included RD-tension, RD-compression, and ND-compression. For each alloy, the VPSC model identified a single set of parameters that can reproduce the stress-strain response and texture evolution. The twin area fraction of four alloys is measured by the EBSD after 5% true strain in RD compression and compared with the twin volume fraction predicted by VPSC model. The VPSC prediction agrees well with the EBSD measurement. The model was then extended to explain the initial softening mechanism after loading in RD compression by adding a dislocation absorption model to the hardening law. The model also included a Hall-Petch hardening mechanism, which treats the twin boundary as an obstacle to dislocation glide. The work shows that with increasing Y concentration, the initial basal texture, plastic anisotropy, and non-basal CRSS/ basal CRSS ratio reduce. Among these reductions, the last one can be attributed to the hardening of the CRSS for basal slip. The simulations of the four Mg-Y alloys suggest that the dislocation absorption rate by twin boundary migration is unaffected by Y concentration. On the other hand, since the twin boundary acts as a strong obstacle to dislocation, the twin boundary is the main reason for the rapid hardening after initial softening in RD-compression.

In both the EPSC and VPSC methods, the twinning behavior was approximated by the composite grain model where the grain consists of matrix and twin regions, wherein only one twin variant is allowed to form. However, different twin variants can also exist in the

same grain and form a twin-twin junction (TTJ) structure. To further investigate twin-twin interactions, the EVP-FFT method was utilized to research the interactions between two non-parallel twins with same zone axis. In this work they are called the recipient twin (RT) and impinging twin (IT). The analysis considers a model single crystal with an orientation given by Euler angles (0,0,0) that is compressed to 0.5% stain. This compression direction produces a high Schmid factor for RT-$(01\bar{1}2)[0\bar{1}11]$ and IT-$(01\bar{1}2)[0\bar{1}11]$, ideal for forming a TTJ. The TTJ with different relative twin thicknesses, i.e., RT_t /IT_t= 1,2,3,4 and IT_t /RT_t= 1,2,3,4, is investigated in three different Mg alloys. The plastic anisotropy (PA) measure is adapted in this study to compare the effect of alloy additions on the TTJ response. First, a set of simulations is performed with RT_t /IT_t= 1,2,3,4 to study how the RT_t affects IT growth. Likewise, another set of simulations with IT_t /RT_t= 1,2,3,4 is conducted to study the "apparent crossing" of the RT by IT and how RT growth is affected by IT thickness. The study shows that for all the RT_t studied, the growth of the IT is not favored after the TTJ first forms. On the other hand, increasing IT_t will promote the apparent crossing of the IT over the RT. Further calculations suggest that apparent crossing requires additional increases in stress and is not automatic under the same stress that caused the junction to form in the first place. Last, alloying additions appear to have a minor effect on the apparent TTJ crossing mechanism. The TRSS profile analysis does not find a correlation between the TRSS along the TTJ interface and the PA measure. It is worth mentioning, however, that a non-co-zone twin variant may form in MgLi near the IT bottom area, which has the lowest PA value, but the stress field in the IT top boundary in AZ31 and PMg show that co-zone twin variant is more likely to form. So, in the PMg

and AZ31, some tiny twins of same twin variant as the IT may form parallel to the IT. This type of configuration has been identified by the TEM study.

In summary, dislocation-twin interactions and twin-twin interactions are studied in this thesis work via three studies. The first and second studies related the microstructure response to macroscopic softening and hardening behavior in HCP Ti and HCP Mg alloys via the mean field crystal plasticity modeling. This is antipciated to help the design the processing of advanced HCP alloy material for the specific applications. The last study aims to understand how the TTJ configuration affects twin nucleation and growth within a grain. The findings can be used to further improve the crystal plasticity models, which are efficient tools for researching processing/microstructure/property relationships, for HCP Mg alloys.

8 Recommendations for future work

While this study investigated several interaction mechanisms, including dislocation-twin interactions and twin-twin interactions, many unanswered questions remain. Based on the research findings from this thesis research, the following efforts for the future are recommended.

8.1 Interaction between non-co-zone twins and different types of twin-twin interactions

This thesis study of twin-twin interactions is limited to co-zone twin-twin interactions. In fact, non-co-zone twin-twin interactions are even less well understood. The twin shears of two non-co-zone twin variants do not act within the same plane, therefore calling for a 3D simulation model to investigate non-co-zone TTJs. Considering the angles between

the two interacting twinning planes in any TTJ, the two sides of the IT can be referred as an obtuse angle region and acute region. In co-zone TTJs, the IT is roughly perpendicular to the RT, so the stress field between the obtuse angle and acute angle regions are not too different. However, this is not the case in a non-co-zone TTJ. Thus, it can be expected that migration of the IT boundary between the acute and obtuse sides will differ, even without considering other external factors that could lead to asymmetry (nearby defects, grain boundaries). Furthermore, this non-co-zone asymmetry may also affect the migration of the boundary of the RT. Another difference between co-zone and non-co-zone TTJs is that TEM observations find that the non-co-zone TTJs always are accompanied by secondary twinning at the junction in Mg and Mg alloys. The reason for the secondary twinning remains unknown. Furthermore, different types of twins can be activated within the same grain. The interactions between different types of twins are also unclear.

Similar to the TTJ study in this thesis work, the EVP-FFT model can be used to study the strain field, stress field, and dislocation activity around the twin TTJ. A 3D simulation setup, instead of 2D, is required since the twin plane normal and twin shear direction of both twin variant in non-co-zone TTJ is not in the same plane. To validate the result, some experimental studies are recommended. First, the high-resolution electron backscatter diffraction (HR-EBSD) analysis can be performed on the polycrystalline samples to obtain the micromechanical fields around the TTJ. With the HR-EBSD method it is possible to calculate the elastic strain variations and lattice rotations based on the shift features of Kikuchi diffraction patterns collected from the initial and deformed samples. These stress

fields can be calculated by the elastic modulus and strain field (Abdolvand and Wilkinson, 2016). This analysis can provide reliable results on and valuable insight into how TTJs form and subsequently grow in the crystal. However, the mechanical field is limited to one plane since it extracts the information from the surface of the sample. Due to the nature of simulation, the mechanical field in the EVP-FFT model in any plane can be easily obtained. Accordingly one can compare the HR-EBSD analysis with the EVP-FFT work for validation, then use the EVPFFT model to study the mechanical field in other planes. Secondly, the EVP-FFT model can forcast the directions of twin growth or nucleation around TTJ. This can be discussed with reference to studies of various twin morphologies around TTJs in grain via TEM, TKD, or procession electron diffraction (PED).

8.2 Twin variant selection

The selection of twin variant of TTJ in this thesis research is based on the Schmid factor. However, the selection in the activation of twin variants in polycrystal is more complicated and cannot be determined by just the Schmid factor. Kadiri et al. (2013) found that most grains with two close Schmid factor (0.47 and 0.44) twin variants still have a predominant twin variant. Statistical research in twinning in Zr shows that significant amounts of twins do not correspond to the highest Schmid factor twin variants for the parent grain (Capolungo et al., 2009). Thus, this “non-Schmid effect”, such as grain boundary misorientation and grain-grain interactions might also play a role in TTJ formation. One factor could be the grain size. A positive grain size effect on twinning has been reported in several metals(Barnett et al., 2004; Christian and Mahajan, 1995; Meyers et al., 2001). Based on microscopy data on these deformed materials, twinning

appears more frequently in larger grains. Yet it is stil not clear how the grain size will affect the selection of the twin variant.

One possible study for clarifying the quantities that govern twin variant selection is recommended based on the findings of this thesis work. First, both compression and tension tests could be performed on the rolled Mg polycrystal. The stress-strain data can then be used for mean-field model calibration. Next, electron backscatter diffraction (EBSD) can be employed for obtaining statistical data on multiple properties of each grain, including grain orientation, twin numbers, and twin variants. At the same time, this statistical information can also be obtained from the mean-field model. One will then be able to compare the statistical data for further validation of the model. Agreement between the simulation and experimental measurements, could give insight into how the input average grain size can be maniupulated. With a validated model, it can be used to isolate grain size effects by altering grain size while keeping other inputs the same. It is anticipated that the activated twin variants from such calculations can elucidate a dependence of twin variant selection on grain size.

8.3 Advancement of a mechanism for twin hardening

Crystal plasticity-based modeling usually requires a hardening law to adequately account for the plasticity in the metal. As its currently stands, the hardening law used in the CP model can be further improved with a deeper understanding of twin-twin interactions. This may be more important in the mean-field scheme, such as VPSC than EVP-FFT, since the full field scheme EVP-FFT can already model the twin domains and TTJs explicitly.

Many mean-field models use the predominant twin system algorithm, which allows only the predominate twin to form in the grain. Advancement of the mean-field schemes to hardening due to twin-twin interactions could start by invoking a Hall-Petch like hardening mechanism by the TTJ. This may be sufficient in most cases. However, further considerations may be necessary, since, as this thesis research found, TTJs can be activated and can have unique hardening behavior. Therefore, it is worth upgrading twinning hardening mechanisms in polycrystal plasticity models and in tandem, developing a more compressive understanding of twin-twin interactions.

References

Abdolvand, H., Wilkinson, A.J., 2016. Assessment of residual stress fields at deformation twin tips and the surrounding environments. Acta Mater 105, 219-231.

Agnew, S., Yoo, M., Tome, C., 2001. Application of texture simulation to understanding mechanical behavior of Mg and solid solution alloys containing Li or Y. Acta Mater 49, 4277-4289.

Agnew, S.R., Duygulu, O., 2005. Plastic anisotropy and the role of non-basal slip in magnesium alloy AZ31B. Int J Plasticity 21, 1161-1193.

Agnew, S.R., Horton, J.A., Yoo, M.H., 2002. Transmission electron microscopy investigation of < c+a > dislocations in Mg and alpha-solid solution Mg-Li alloys. Metall Mater Trans A 33, 851-858.

Ando, S., Tsushida, M., Kitahara, H., 2012. Plastic Deformation Behavior in Magnesium Alloy Single Crystals. Mater Sci Forum 706-709, 1122-+.

Ansari, N., Sarvesha, R., Lee, S.Y., Singh, S.S., Jain, J., 2020. Influence of yttrium addition on recrystallization, texture and mechanical properties of binary Mg-Y alloys. Mat Sci Eng a-Struct 793.

Ardeljan, M., Beyerlein, I.J., McWilliams, B.A., Knezevic, M., 2016. Strain rate and temperature sensitive multi-level crystal plasticity model for large plastic deformation behavior: Application to AZ31 magnesium alloy. Int J Plasticity 83, 90-109.

Arul Kumar, M., Leu, B., Rottmann, P., Beyerlein, I.J., 2019. Characterization of Staggered Twin Formation in HCP Magnesium, in: Joshi, V.V., Jordon, J.B., Orlov, D., Neelameggham, N.R. (Eds.), Magnesium Technology 2019. Springer International Publishing, Cham, pp. 207-213.

Bachmann, F., Hielscher, R., Schaeben, H., 2010. Texture Analysis with MTEX - Free and Open Source Software Toolbox. Solid State Phenomen 160, 63-+.

Barnett, M.R., Keshavarz, Z., Beer, A.G., Atwell, D., 2004. Influence of grain size on the compressive deformation of wrought Mg–3Al–1Zn. Acta Mater 52, 5093-5103.

Basinski, Z.S., 1974. Forest Hardening in Face-Centered Cubic Metals. Scripta Metallurgica 8, 1301-1307.

Basinski, Z.S., Szczerba, M.S., Niewczas, M., Embury, J.D., Basinski, S.J., 1997. The transformation of slip dislocations during twinning of copper-aluminum alloy crystals. Rev Metall-Paris 94, 1037-1043.

Bauschinger, J., 1886. Über die Veränderung der Elasticitätsgrenze und Festigkeit des Eisen und Stahls durch Strecken und Quetschen, durch Erwarmen und Abkühlen und durch oftmal wiederholte Beanspruchung. Mitteilungen aus dem mechanisch-technischen Laboratorium der k. polytechnischen Schule, 1877-1836.

Becker, H., Pantleon, W., 2013. Work-hardening stages and deformation mechanism maps during tensile deformation of commercially pure titanium. Comp Mater Sci 76, 52-59.

Benmhenni, N., Bouvier, S., Brenner, R., Chauveau, T., Bacroix, B., 2013. Micromechanical modelling of monotonic loading of CP alpha-Ti: Correlation between macroscopic and microscopic behaviour. Mat Sci Eng a-Struct 573, 222-233.

Beyerlein, I., Capolungo, L., Marshall, P., McCabe, R., Tomé, C., 2010. Statistical analyses of deformation twinning in magnesium. Philos Mag 90, 2161-2190.

Beyerlein, I.J., McCabe, R.J., Tomé, C.N., 2011. Effect of microstructure on the nucleation of deformation twins in polycrystalline high-purity magnesium: A multi-scale modeling study. J Mech Phys Solids 59, 988-1003.

Beyerlein, I.J., Tomé, C.N., 2008. A dislocation-based constitutive law for pure Zr including temperature effects. Int J Plasticity 24, 867-895.

Brenner, R., Lebensohn, R.A., Castelnau, O., 2009. Elastic anisotropy and yield surface estimates of polycrystals. Int J Solids Struct 46, 3018-3026.
Britton, T.B., Dunne, F.P.E., Wilkinson, A.J., 2015. On the mechanistic basis of deformation at the microscale in hexagonal close-packed metals. P Roy Soc a-Math Phy 471.
Callister, W.D., Rethwisch, D.G., 2013. Materials Science and Engineering: An Introduction, 9th Edition: Ninth Edition. John Wiley and Sons, Incorporated.
Chen, P., Wang, F.X., Li, B., 2019. Dislocation absorption and transmutation at {10(1)over-bar2} twin boundaries in deformation of magnesium. Acta Mater 164, 440-453.
Chichili, D.R., Ramesh, K.T., Hemker, K.J., 1998. The high-strain-rate response of alpha-titanium: Experiments, deformation mechanisms and modeling. Acta Mater 46, 1025-1043.
Chino, Y., Kado, M., Mabuchi, M., 2008a. Compressive deformation behavior at room temperature-773 K 14 in Mg-0.2 mass%(0.035at.%)Ce alloy. Acta Mater 56, 387-394.
Chino, Y., Kado, M., Mabuchi, M., 2008b. Enhancement of tensile ductility and stretch formability of magnesium by addition of 0.2 wt%(0.035 at%)Ce. Mat Sci Eng a-Struct 494, 343-349.
Chino, Y., Sassa, K., Mabuchi, M., 2009. Texture and stretch formability of a rolled Mg-Zn alloy containing dilute content of Y. Mat Sci Eng a-Struct 513-14, 394-400.
Christian, J.W., Mahajan, S., 1995. Deformation twinning. Prog Mater Sci 39, 1-157.
El Kadiri, H., Kapil, J., Oppedal, A.L., Hector, L.G., Agnew, S.R., Cherkaoui, M., Vogel, S.C., 2013. The effect of twin–twin interactions on the nucleation and propagation of {101¯2} twinning in magnesium. Acta Mater 61, 3549-3563.
Essmann, U., Mughrabi, H., 1979. Annihilation of dislocations during tensile and cyclic deformation and limits of dislocation densities. Philosophical Magazine A 40, 731-756.
Fan, H.D., Aubry, S., Arsenlis, A., El-Awady, J.A., 2015. The role of twinning deformation on the hardening response of polycrystalline magnesium from discrete dislocation dynamics simulations. Acta Mater 92, 126-139.
Ganeshan, S., Shang, S.L., Wang, Y., Liu, Z.K., 2009. Effect of alloying elements on the elastic properties of Mg from first-principles calculations. Acta Mater 57, 3876-3884.
Gao, L., Chen, R.S., Han, E.H., 2009. Solid solution strengthening behaviors in binary Mg-Y single phase alloys. J Alloy Compd 472, 234-240.
Ghorbanpour, S., Zecevic, M., Kumar, A., Jahedi, M., Bicknell, J., Jorgensen, L., Beyerlein, I.J., Knezevic, M., 2017. A crystal plasticity model incorporating the effects of precipitates in superalloys: Application to tensile, compressive, and cyclic deformation of Inconel 718. Int J Plasticity 99, 162-185.
Gong, M.Y., Liu, G.S., Wang, J., Capolungo, L., Tome, C.N., 2018a. Atomistic simulations of interaction between basal <a> dislocations and three-dimensional twins in magnesium. Acta Mater 155, 187-198.
Gong, M.Y., Xu, S., Jiang, Y.Y., Liu, Y., Wang, J., 2018b. Structural characteristics of {(1)over-bar012} non-cozone twin-twin interactions in magnesium. Acta Mater 159, 65-76.
Hama, T., Kitamura, N., Takuda, H., 2013. Effect of twinning and detwinning on inelastic behavior during unloading in a magnesium alloy sheet. Mat Sci Eng a-Struct 583, 232-241.
Hama, T., Kobuki, A., Fujimoto, H., Takuda, H., 2016. Crystal-plasticity finite-element analysis of deformation behavior in a commercially pure titanium sheet. J Phys Conf Ser 734.
Hama, T., Nagao, H., Kobuki, A., Fujimoto, H., Takuda, H., 2015. Work-hardening and twinning behaviors in a commercially pure titanium sheet under various loading paths. Mat Sci Eng a-Struct 620, 390-398.

Han, W.Z., Carpenter, J.S., Wang, J., Beyerlein, I.J., Mara, N.A., 2012. Atomic-level study of twin nucleation from face-centered-cubic/body-centered-cubic interfaces in nanolamellar composites. Appl Phys Lett 100.
Hantzsche, K., Bohlen, J., Wendt, J., Kainer, K.U., Yi, S.B., Letzig, D., 2010. Effect of rare earth additions on microstructure and texture development of magnesium alloy sheets. Scripta Mater 63, 725-730.
Hong, S.G., Park, S.H., Lee, C.S., 2010. Role of {10-12} twinning characteristics in the deformation behavior of a polycrystalline magnesium alloy. Acta Mater 58, 5873-5885.
Hooshmand, M.S., Mills, M.J., Ghazisaeidi, M., 2017. Atomistic modeling of dislocation interactions with twin boundaries in Ti. Modelling and Simulation in Materials Science and Engineering 25.
Hosford, W.F., 1993. The Mechanics of Crystals and Textured Polycrystals. Oxford University Press, USA.
Huang, G.H., Yin, D.D., Lu, J.W., Zhou, H., Zeng, Y., Quan, G.F., Wang, Q.D., 2018. Microstructure, texture and mechanical properties evolution of extruded fine-grained Mg-Y sheets during annealing. Mat Sci Eng a-Struct 720, 24-35.
Jang, H.S., Lee, B.J., 2019. Effects of Zn on < c plus a > slip and grain boundary segregation of Mg alloys. Scripta Mater 160, 39-43.
Juan, P.A., Pradalier, C., Berbenni, S., McCabe, R.J., Tomé, C.N., Capolungo, L., 2015. A statistical analysis of the influence of microstructure and twin–twin junctions on twin nucleation and twin growth in Zr. Acta Mater 95, 399-410.
Kanjarla, A.K., Lebensohn, R.A., Balogh, L., Tomé, C.N., 2012. Study of internal lattice strain distributions in stainless steel using a full-field elasto-viscoplastic formulation based on fast Fourier transforms. Acta Mater 60, 3094-3106.
Kassner, M., Prado, M.P., Hayes, T., Jiang, L., Barrabes, S., Lee, I., 2013a. Elevated temperature deformation of Zr to large strains. Journal of Materials Science 48, 4492-4500.
Kassner, M.E., Geantil, P., Levine, L.E., 2013b. Long range internal stresses in single-phase crystalline materials. Int J Plasticity 45, 44-60.
Kassner, M.E., Ziaai-Moayyed, A.A., Miller, A.K., 1985. Some trends observed in the elevated-temperature kinematic and isotropic hardening of type 304 stainless steel. Metallurgical Transactions A 16, 1069-1076.
Kitayama, K., Tomé, C., Rauch, E., Gracio, J., Barlat, F., 2013. A crystallographic dislocation model for describing hardening of polycrystals during strain path changes. Application to low carbon steels. Int J Plasticity 46, 54-69.
Knezevic, M., Beyerlein, I.J., Brown, D.W., Sisneros, T.A., Tomé, C.N., 2013. A polycrystal plasticity model for predicting mechanical response and texture evolution during strain-path changes: Application to beryllium. Int J Plasticity 49, 185-198.
Knezevic, M., Levinson, A., Harris, R., Mishra, R.K., Doherty, R.D., Kalidindi, S.R., 2010. Deformation twinning in AZ31: Influence on strain hardening and texture evolution. Acta Mater 58, 6230-6242.
Knezevic, M., Zecevic, M., Beyerlein, I.J., Bingert, J.F., McCabe, R.J., 2015. Strain rate and temperature effects on the selection of primary and secondary slip and twinning systems in HCP Zr. Acta Mater 88, 55-73.
Kocks, U.F., Mecking, H., 1981. Kinetics of Flow and Strain-Hardening. Acta Metallurgica 29, 1865-1875.
Kocks, U.F., Mecking, H., 2003. Physics and phenomenology of strain hardening: the FCC case. Prog Mater Sci 48, 171-273.

Kula, A., Jia, X., Mishra, R.K., Niewczas, M., 2017. Flow stress and work hardening of Mg-Y alloys. Int J Plasticity 92, 96-121.
Kumar, A., Morrow, B.M., McCabe, R.J., Beyerlein, I.J., 2017a. An atomic-scale modeling and experimental study of < c plus a > dislocations in Mg. Mat Sci Eng a-Struct 695, 270-278.
Kumar, M.A., Beyerlein, I.J., Lebensohn, R.A., Tome, C.N., 2017b. Role of alloying elements on twin growth and twin transmission in magnesium alloys. Mat Sci Eng a-Struct 706, 295-303.
Kumar, M.A., Beyerlein, I.J., Tome, C.N., 2016. Effect of local stress fields on twin characteristics in HCP metals. Acta Mater 116, 143-154.
Kumar, M.A., Gong, M., Beyerlein, I.J., Wang, J., Tome, C.N., 2019. Role of local stresses on co-zone twin-twin junction formation in HCP magnesium. Acta Mater 168, 353-361.
Lavrentev, F.F., 1980. The type of dislocation interaction as the factor determining work hardening. Mater Sci Eng 46, 191-208.
Lebensohn, R.A., 2001. N-site modeling of a 3D viscoplastic polycrystal using Fast Fourier Transform. Acta Mater 49, 2723-2737.
Lebensohn, R.A., Brenner, R., Castelnau, O., Rollett, A.D., 2008. Orientation image-based micromechanical modelling of subgrain texture evolution in polycrystalline copper. Acta Mater 56, 3914-3926.
Lebensohn, R.A., Tomé, C.N., 1993. A self-consistent anisotropic approach for the simulation of plastic deformation and texture development of polycrystals: Application to zirconium alloys. Acta Metallurgica et Materialia 41, 2611-2624.
Lentz, M., Behringer, A., Fahrenson, C., Beyerlein, I.J., Reimers, W., 2014. Grain Size Effects on Primary, Secondary, and Tertiary Twin Development in Mg-4 wt pct Li (-1 wt pct Al) Alloys. Metall Mater Trans A 45a, 4737-4741.
Lentz, M., Klaus, M., Beyerlein, I.J., Zecevic, M., Reimers, W., Knezevic, M., 2015a. In situ X-ray diffraction and crystal plasticity modeling of the deformation behavior of extruded Mg-Li-(Al) alloys: An uncommon tension-compression asymmetry. Acta Mater 86, 254-268.
Lentz, M., Klaus, M., Beyerlein, I.J., Zecevic, M., Reimers, W., Knezevic, M., 2015b. In situ X-ray diffraction and crystal plasticity modeling of the deformation behavior of extruded Mg–Li–(Al) alloys: An uncommon tension–compression asymmetry. Acta Mater 86, 254-268.
Lorentzen, T., Daymond, M.R., Clausen, B., Tomé, C.N., 2002. Lattice strain evolution during cyclic loading of stainless steel. Acta Mater 50, 1627-1638.
Ma, C., Wang, H.M., Hama, T., Guo, X.Q., Mao, X.B., Wange, J., Wu, P., 2019. Twinning and detwinning behaviors of commercially pure titanium sheets. Int J Plasticity 121, 261-279.
Meyers, M.A., Vohringer, O., Lubarda, V.A., 2001. The onset of twinning in metals: A constitutive description. Acta Mater 49, 4025-4039.
Molodov, K.D., Al-Samman, T., Molodov, D.A., 2017. Profuse slip transmission across twin boundaries in magnesium. Acta Mater 124, 397-409.
Morrow, B.M., Cerreta, E.K., McCabe, R.J., Tomé, C.N., 2014a. Toward understanding twin–twin interactions in hcp metals: Utilizing multiscale techniques to characterize deformation mechanisms in magnesium. Materials Science and Engineering: A 613, 365-371.
Morrow, B.M., McCabe, R.J., Cerreta, E.K., Tomé, C.N., 2014b. In-Situ TEM Observation of Twinning and Detwinning During Cyclic Loading in Mg. Metallurgical and Materials Transactions A 45, 36-40.
Mott, N.F., 1952. A Theory of Work-Hardening of Metal Crystals. Philos Mag 43, 1151-1178.
Moulinec, H., Suquet, P., 1998. A numerical method for computing the overall response of nonlinear composites with complex microstructure. Computer methods in applied mechanics and engineering 157, 69-94.

Mughrabi, H., 1983. Dislocation wall and cell structures and long-range internal stresses in deformed metal crystals. Acta Metallurgica 31, 1367-1379.
Niezgoda, S.R., Kanjarla, A.K., Beyerlein, I.J., Tomé, C.N., 2014. Stochastic modeling of twin nucleation in polycrystals: An application in hexagonal close-packed metals. Int J Plasticity 56, 119-138.
Oppedal, A.L., El Kadiri, H., Tomé, C.N., Kaschner, G.C., Vogel, S.C., Baird, J.C., Horstemeyer, M.F., 2012. Effect of dislocation transmutation on modeling hardening mechanisms by twinning in magnesium. Int J Plasticity 30-31, 41-61.
Ostapovets, A., Serra, A., 2014. Characterization of the matrix-twin interface of a (10(1)over-bar2) twin during growth. Philos Mag 94, 2827-2839.
Partridge, P.G., 1967. The crystallography and deformation modes of hexagonal close-packed metals. Metallurgia Revised 12, 169.
Paton, N.E., Backofen, W.A., 1970. Plastic deformation of titanium at elevated temperatures. Metallurgical Transactions 1, 2839-2847.
Pedersen, O.B., Brown, L.M., Stobbs, W.M., 1981. The Bauschinger Effect in Copper. Acta Metallurgica 29, 1843-1850.
Pradalier, C., Juan, P.A., McCabe, R.J., Capolungo, L., 2018. A Graph Theory-Based Automated Twin Recognition Technique for Electron Backscatter Diffraction Analysis. Integrating Materials and Manufacturing Innovation 7, 12-27.
Proust, G., Tomé, C.N., Kaschner, G.C., 2007. Modeling texture, twinning and hardening evolution during deformation of hexagonal materials. Acta Mater 55, 2137-2148.
Rikihisa, H., Mori, T., Tsushida, M., Kitahara, H., Ando, S., 2017. Influence of Yttrium Addition on Plastic Deformation of Magnesium. Materials Transactions 58, 1656-1663.
Risse, M., Lentz, M., Fahrenson, C., Reimers, W., Knezevic, M., Beyerlein, I.J., 2017. Elevated Temperature Effects on the Plastic Anisotropy of an Extruded Mg-4 Wt Pct Li Alloy: Experiments and Polycrystal Modeling. Metallurgical and Materials Transactions A 48, 446-458.
Roberts, C.S., 1960. Magnesium and Its Alloys. Wiley, New York/London.
Roberts, E., Partridge, P.G., 1966. The accommodation around {10$\bar{1}$2} 〈$\bar{1}$011〉 twins in magnesium. Acta Metallurgica 14, 513-527.
Salem, A.A., Kalidindi, S.R., Doherty, R.D., 2003. Strain hardening of titanium: role of deformation twinning. Acta Mater 51, 4225-4237.
Sandlobes, S., Friak, M., Neugebauer, J., Raabe, D., 2013. Basal and non-basal dislocation slip in Mg-Y. Mat Sci Eng a-Struct 576, 61-68.
Sandlobes, S., Friak, M., Zaefferer, S., Dick, A., Yi, S., Letzig, D., Pei, Z., Zhu, L.F., Neugebauer, J., Raabe, D., 2012. The relation between ductility and stacking fault energies in Mg and Mg-Y alloys. Acta Mater 60, 3011-3021.
Sandlöbes, S., Zaefferer, S., Schestakow, I., Yi, S., Gonzalez-Martinez, R., 2011. On the role of non-basal deformation mechanisms for the ductility of Mg and Mg–Y alloys. Acta Mater 59, 429-439.
Sangid, M.D., Ezaz, T., Sehitoglu, H., 2012. Energetics of residual dislocations associated with slip-twin and slip-GBs interactions. Mat Sci Eng a-Struct 542, 21-30.
Seeger, A., Diehl, J., Mader, S., Rebstock, H., 1957. Work-Hardening and Work-Softening of Face-Centred Cubic Metal Crystals. Philos Mag 2, 323-+.
Serra, A., Bacon, D.J., 1995. Computer simulation of screw dislocation interactions with twin boundaries in H.C.P. metals. Acta Metallurgica et Materialia 43, 4465-4481.
Serra, A., Bacon, D.J., 1996. A new model for {1012} twin growth in hcp metals. Philosophical Magazine A 73, 333-343.

Serra, A., Bacon, D.J., Pond, R.C., 1999. Dislocations in interfaces in the h.c.p. metals—I. Defects formed by absorption of crystal dislocations. Acta Mater 47, 1425-1439.
Serra, A., Bacon, D.J., Pond, R.C., 2002. Twins as barriers to basal slip in hexagonal-close-packed metals. Metall Mater Trans A 33, 809-812.
Shi, B.Q., Chen, R.S., Ke, W., 2013. Effects of yttrium and zinc on the texture, microstructure and tensile properties of hot-rolled magnesium plates. Mat Sci Eng a-Struct 560, 62-70.
Simmons, G., Wang, H., 1971. Single crystal elastic constants and calculated aggregate properties.
Stanford, N., Carlson, U., Barnett, M.R., 2008. Deformation twinning and the Hall-Petch relation in commercial purity Ti. Metall Mater Trans A 39a, 934-944.
Stanford, N., Cottam, R., Davis, B., Robson, J., 2014. Evaluating the effect of yttrium as a solute strengthener in magnesium using in situ neutron diffraction. Acta Mater 78, 1-13.
Sun, Q., Zhang, X.Y., Ren, Y., Tan, L., Tu, J., 2015a. Observations on the intersection between 10$\bar{1}$2 twin variants sharing the same zone axis in deformed magnesium alloy. Materials characterization 109, 160-163.
Sun, Q., Zhang, X.Y., Ren, Y., Tan, L., Tu, J., 2015b. Observations on the intersection between {10(1)over-bar2} twin variants sharing the same zone axis in deformed magnesium alloy. Materials Characterization 109, 160-163.
Takernoto, K., Rikihisa, H., Tsushida, M., Kitahara, H., Ando, S., 2020. Effects of Yttrium Addition on Plastic Deformation of Rolled Magnesium. Materials Transactions 61, 935-940.
Tirry, W., Bouvier, S., Benmhenni, N., Hammami, W., Habraken, A.M., Coghe, F., Schryvers, D., Rabet, L., 2012. Twinning in pure Ti subjected to monotonic simple shear deformation. Materials Characterization 72, 24-36.
Tomé, C., Kaschner, G.C., 2005. Modeling Texture, Twinning and Hardening Evolution during Deformation of Hexagonal Materials. Materials Science Forum 495-497, 1001-1006.
Vanderplanken, J., Deruyttere, A., 1969. Solution Hardening of Magnesium Single Crystals by Tin at Room Temperature. Acta Metallurgica 17, 451-+.
Wang, F., Hazeli, K., Molodov, K.D., Barrett, C.D., Al-Samman, T., Molodov, D.A., Kontsos, A., Ramesh, K.T., El Kadiri, H., Agnew, S.R., 2018. Characteristic dislocation substructure in {10(1)over-bar2} twins in hexagonal metals. Scripta Mater 143, 81-85.
Wang, F.L., Agnew, S.R., 2016. Dislocation transmutation by tension twinning in magnesium alloy AZ31. Int J Plasticity 81, 63-86.
Wang, J., Beyerlein, I., Tomé, C., 2014. Reactions of lattice dislocations with grain boundaries in Mg: implications on the micro scale from atomic-scale calculations. Int J Plasticity 56, 156-172.
Wang, J., Liu, L., Tome, C.N., Mao, S.X., Gong, S.K., 2013. Twinning and De-twinning via Glide and Climb of Twinning Dislocations along Serrated Coherent Twin Boundaries in Hexagonal-close-packed Metals. Materials Research Letters 1, 81-88.
Wang, J., Wang, X., Yu, K., Rupert, T., Mahajan, S., Lavernia, E., Schoenung, J., Beyerlein, I., 2021. Manipulating deformation mechanisms with Y alloying of Mg. Materials Science and Engineering: A 817, 141373.
Wang, J.Y., Li, N., Alizadeh, R., Monclus, M.A., Cui, Y.W., Molina-Aldareguia, J.M., LLorca, J., 2019. Effect of solute content and temperature on the deformation mechanisms and critical resolved shear stress in Mg-Al and Mg-Zn alloys. Acta Mater 170, 155-165.
Wang, L., Zheng, Z., Phukan, H., Kenesei, P., Park, J.S., Lind, J., Suter, R.M., Bieler, T.R., 2017. Direct measurement of critical resolved shear stress of prismatic and basal slip in polycrystalline Ti using high energy X-ray diffraction microscopy. Acta Mater 132, 598-610.
Warwick, J.L.W., Jones, N.G., Rahman, K.M., Dye, D., 2012. Lattice strain evolution during tensile and compressive loading of CP Ti. Acta Mater 60, 6720-6731.

Wen, W., Borodachenkova, M., Tome, C.N., Vincze, G., Rauch, E.F., Barlat, F., Gracio, J.J., 2015. Mechanical behavior of Mg subjected to strain path changes: Experiments and modeling. Int J Plasticity 73, 171-183.
Williams, C.L., Mallick, D.D., Wilkerson, J.W., 2020. A Concise Note on Deformation Twinning and Spall Failure in Magnesium at the Extremes. J Dynam Behav Mat 6, 432-444.
Wollmershauser, J.A., Clausen, B., Agnew, S.R., 2012. A slip system-based kinematic hardening model application to in situ neutron diffraction of cyclic deformation of austenitic stainless steel. International Journal of Fatigue 36, 181-193.
Won, J.W., Choi, S.W., Yeom, J.T., Hyun, Y.T., Lee, C.S., Park, S.H., 2017. Anisotropic twinning and slip behaviors and their relative activities in rolled alpha-phase titanium. Mat Sci Eng a-Struct 698, 54-62.
Won, J.W., Park, C.H., Hong, S.G., Lee, C.S., 2015. Deformation anisotropy and associated mechanisms in rolling textured high purity titanium. J Alloy Compd 651, 245-254.
Wronski, M., Kumar, M.A., Capolungo, L., McCabe, R.J., Wierzbanowski, K., Tome, C.N., 2018. Deformation behavior of CP-titanium: Experiment and crystal plasticity modeling. Mat Sci Eng a-Struct 724, 289-297.
Wu, X., Kalidindi, S.R., Necker, C., Salem, A.A., 2008. Modeling anisotropic stress-strain response and crystallographic texture evolution in α-titanium during large plastic deformation using Taylor-type models: Influence of initial texture and purity. Metallurgical and Materials Transactions A 39A, 3046-3054.
Wu, Z.X., Ahmad, R., Yin, B.L., Sandlobes, S., Curtin, W.A., 2018. Mechanistic origin and prediction of enhanced ductility in magnesium alloys. Science 359, 447-451.
Xie, K.Y., Alam, Z., Caffee, A., Hemker, K.J., 2016. Pyramidal I slip in c-axis compressed Mg single crystals. Scripta Mater 112, 75-78.
Xin, Y.C., Lv, L.C., Chen, H.W., He, C., Yu, H.H., Liu, Q., 2016. Effect of dislocation-twin boundary interaction on deformation by twin boundary migration. Mat Sci Eng a-Struct 662, 95-99.
Xu, F., Zhang, X.Y., Ni, H.T., Liu, Q., 2012. {1 1 (2)over-bar 4} deformation twinning in pure Ti during dynamic plastic deformation. Mat Sci Eng a-Struct 541, 190-195.
Yoo, M.H., 1981. Slip, twinning, and fracture in hexagonal close-packed metals. Metall. Mater. Trans. A 12, 409–418.
Yoo, M.H., Morris, J.R., Ho, K.M., Agnew, S.R., 2002. Nonbasal deformation modes of HCP metals and alloys: Role of dislocation source and mobility. Metallurgical and Materials Transactions A 33, 813-822.
Yoshinaga, H., Horiuchi, R., 1963. Deformation mechanisms in magnesium single crystals compressed in the direction parallel to hexagonal axis. Transactions of the Japan Institute of Metals 4, 1-8.
Yu, Q., Jiang, Y.Y., Wang, J., 2015. Cyclic deformation and fatigue damage in single-crystal magnesium under fully reversed strain-controlled tension-compression in the [10(1)over-bar0] direction. Scripta Mater 96, 41-44.
Yu, Q., Wang, J., Jiang, Y., McCabe, R.J., Li, N., Tomé, C.N., 2014a. Twin–twin interactions in magnesium. Acta Mater 77, 28-42.
Yu, Q., Wang, J., Jiang, Y.Y., McCabe, R.J., Tome, C.N., 2014b. Co-zone {(1)over-bar012} Twin Interaction in Magnesium Single Crystal. Materials Research Letters 2, 82-88.
Yu, Q., Zhang, J.X., Jiang, Y.Y., 2011. Direct observation of twinning-detwinning-retwinning on magnesium single crystal subjected to strain-controlled cyclic tension-compression in [0001] direction. Philosophical Magazine Letters 91, 757-765.
Zecevic, M., Beyerlein, I.J., Knezevic, M., 2018. Activity of pyramidal I and II <c+a> slip in Mg alloys as revealed by texture development. J Mech Phys Solids 111, 290-307.

Zecevic, M., Knezevic, M., 2015a. A dislocation density based elasto-plastic self-consistent model for the prediction of cyclic deformation: Application to AA6022-T4. Int J Plasticity 72, 200-217.
Zecevic, M., Knezevic, M., 2015b. A dislocation density based elasto-plastic self-consistent model for the prediction of cyclic deformation: Application to Al6022-T4. Int J Plasticity 72, 200-217.
Zecevic, M., Knezevic, M., 2018. Latent hardening within the elasto-plastic self-consistent polycrystal homogenization to enable the prediction of anisotropy of AA6022-T4 sheets. Int J Plasticity 105, 141-163.
Zecevic, M., Korkolis, Y.P., Kuwabara, T., Knezevic, M., 2016. Dual-phase steel sheets under cyclic tension-compression to large strains: Experiments and crystal plasticity modeling. J Mech Phys Solids 96, 65-87.
Zhang, D.L., Jiang, L., Wang, X., Beyerlein, I.J., Minor, A.M., Schoenung, J.M., Mahajan, S., Lavernia, E.J., 2019a. In situ transmission electron microscopy investigation on < c plus a > slip in Mg. J. Mater. Res. 34, 1499-1508.
Zhang, D.L., Jiang, L., Wang, X., Beyerlein, I.J., Minor, A.M., Schoenung, J.M., Mahajan, S., Lavernia, E.J., 2019b. Revealing deformation mechanisms in Mg-Y alloy by in situ deformation of nano-pillars with mediated lateral stiffness. J. Mater. Res. 34, 1542-1554.
Zhang, D.L., Wen, H.M., Kumar, M.A., Chen, F., Zhang, L.M., Beyerlein, I.J., Schoenung, J.M., Mahajan, S., Lavernia, E.J., 2016. Yield symmetry and reduced strength differential in Mg-2.5Y alloy. Acta Mater 120, 75-85.
Zhang, J.D., Zhang, Y., El-Awady, J.A., Tang, Y.Z., 2018. The plausibility of < c plus a > dislocation slip on {-12-11} planes in Mg. Scripta Mater 156, 19-22.
Zhao, C.Y., Li, Z.Y., Shi, J.H., Chen, X.H., Tu, T., Luo, Z., Cheng, R.J., Atrens, A., Pan, F.S., 2019. Strain hardening behavior of Mg-Y alloys after extrusion process. J Magnes Alloy 7, 672-680.
Zheng, S.J., Wang, J., Carpenter, J.S., Mook, W.M., Dickerson, P.O., Mara, N.A., Beyerlein, I.J., 2014. Plastic instability mechanisms in bimetallic nanolayered composites. Acta Mater 79, 282-291.